DUAL MODALITY (NEUTRON AND X-RAY) IMAGING FOR CHARACTERIZATION OF PARTIALLY SATURATED GRANULAR MATERIALS AND FLOW THROUGH POROUS MEDIA

A Dissertation Presented for the
Doctor of Philosophy
Degree
The University of Tennessee, Knoxville

Felix Hoyean Kim
May 2013

Copyright © 2013 by Felix H. Kim

All rights reserved.

DEDICATION

This dissertation is dedicated to my parents Dr. Jinwhan and Pilsoo Kim.

ACKNOWLEDGEMENTS

I would like to thank my advisor, Dr. Dayakar Penumadu, for his support throughout the Ph.D. research. He provided me opportunities to work on the research project, perform neutron and Synchrotron imaging experiments around the world, and attend several international workshops and conferences.

I also thank Drs. Eric Drumm, Jens Gregor, and Andreas Koschan for serving in my committee. Dr. Drumm had taught me undergraduate soil mechanics course, and he was also the advisor of ASCE student chapter which I was active during my undergraduate. Dr. Gregor taught me principles of image reconstruction using filtered backprojection and iterative methods during two semesters of independent study course. I thank Dr. Koschan for discussions of image processing and segmentation.

I would like to thank fellow group members Mr. Jeffrey Bunn, Robin Woracek and Stephen Puplampu for helping with running experiments at neutron imaging facilities and attending international workshops and conferences together. I thank other fellow group members including Dr. Akawut Siriruk, Mr. Mathew Kant, Stephen Young, Aashish Sharma, and Anne Turner for discussions and help received. I would like to thank Mr. Ken Thomas and Mr. Larry Roberts for fabricating experimental instruments to be used at neutron and synchrotron imaging facilities. Their help was essential in performing successful imaging experiments.

I thank Drs. Daniel Hussey and David Jacobson of NIST, Drs. Nikolay Kardjilov, Andre Hilger, and Ingo Make at HZB, Dr. Burkhard Schillinger at TUM and Drs. Peter Vontobel and Eberhard Lehmann at PSI for assisting me with running good neutron imaging experiments. I want to thank Dr. Volker P. Schulz of Baden-Wuerttumberg Cooperative State University at Mannheim for collaboration on simulating flow through compacted sand. I thank Dr. Andreas Wiegmann and Dr. Jurgen Becker of Math2Market on providing me license to use GeoDict software. I thank Dr. Mike Marsh of VSG for helping me with using Avizo software. I thank Mr. Allen Gu, Jeff Gelb, and Ms. Sylvia Yun of Xradia for collaborating on obtaining high resolution X-ray tomography data. I want to thank Dr. Kwai Lam Wong and Mr. Pragneshkumar Patel of National Institute for Computational Science for helping with run simulations on high performance computing cluster. I would like to thank Dr. Anton Tremsin at University of California, Berkeley for obtaining neutron imaging data.

I would like to thank Joint Institute for Advanced Materials (JIAM) Fellowship program for providing additional financial support during my doctoral studies. I received partial financial support from Office of Naval Research (ONR) on a program managed by Dr. Yapa Rajapakse. I also received financial support from Defense Threat Reduction Agency (DTRA) on a program managed by Dr. Suhithi Peiris.

ABSTRACT

Problems involving mechanics of partially saturated soil and physics of flow through porous media are complex and largely unresolved based on using continuum approach. Recent advances in radiation based imaging techniques provide unique access to simultaneously observe continuum scale response while probing corresponding microstructure for developing predictive science and engineering tools in place of phenomenological approach used to date.

Recent developments with X-ray/Synchrotron and neutron imaging techniques provided tools to visualize the interior of soil specimen at pore/grain level. X-ray and neutron radiation often presents complementary contrast for given condensed matter in the images due to different fundamental interaction mechanisms. While X-rays mainly interact with the electron clouds, neutrons directly interact with the nucleus of an atom. The dual-modal contrasts are well suited for probing the three phases (silica, air and water) of partially saturated sand since neutrons provide high penetration through large sample size and are very sensitive to water and X-rays of high energy can penetrate moderate sample sizes and clearly show the particle and void phases.

Both neutron and X-ray imaging techniques are used to study microstructure of partially saturated compacted sand and water flow behavior through sand with different initial structures. Water distribution in compacted sand with different water contents for different grain shapes of sand was

visualized with relatively coarse resolution neutron radiographs and tomograms. Dual-modal contrast of partially saturated sand was presented by using high spatial resolution neutron and X-ray imaging. Advanced image registration technique was used to combine the dual modality data for a more complete quantitative analysis. Quantitative analysis such as grain size distribution, pore size distribution, coordination number, and water saturation along the height were obtained from the image data. Predictive simulations were performed to obtain capillary pressure – saturation curves and simulated two fluid phase (water and air) distribution based image data. In-situ water flow experiments were performed to investigate the effect of initial microstructure. Flow patterns for dense and loose states of Ottawa sand specimens were compared. Flow patterns and water distribution of dense Ottawa and Q-ROK sand specimens was visualized with high resolution neutron and X-ray image data.

TABLE OF CONTENTS

Chapter 1. Introduction and Literature Review 1

1.1 Introduction 2

1.2 Literature Review 11

1.3 References 18

Chapter 2. X-ray and Neutron Imaging 23

2.1 Abstract 24

2.2 X-ray and Neutron 24

2.3 Interaction Mechanism 26

2.4 Lambert – Beer's Law 27

2.5 Radiography 31

2.6 Tomography 34

2.7 Reconstruction 35

2.7.1 Filtered Backprojection 35

2.7.2 Iterative Reconstruction 42

2.7.3. Reconstruction Results 46

2.7.4 Comparison of FBP and ITR 52

2.8 Dual Modality Imaging 52

2.8 References 61

Chapter 3. Neutron Imaging of Partially Saturated Sand 62

3.1 Abstract 64

3.2 Introduction....64
3.3 Sample Description....70
3.4 Water Distribution Variation of Partially Saturated Sand....74
3.5 Conclusions....85
3.6 Appendix....86
3.7 References....89
Chapter 4. High Resolution Dual Modality Imaging of Partially Saturated Sand....92
4.1 Abstract....94
4.2 Introduction....94
4.3 Materials and Methods....99
4.3.1 Materials and Specimen Description....99
4.3.2 Principles of Neutron and X-ray Imaging and Tomography....102
4.3.3 High Resolution Neutron Tomography....104
4.3.4 Microfocus X-ray Tomography....108
4.4 Results and Discussions....108
4.4.1 Neutron Contrast Comparison....108
4.4.2 Effect of Compaction and Grain Shape Morphology on Void and Water Distribution....110
4.4.3 Dual Modality....114
4.4.4 Application to Soil Mechanics....116
4.5 Conclusions....123

4.6 References 125
Chapter 5. Image Registration of Dual Modality Data 129
5.1 Abstract 131
5.2 Introduction 131
5.3 Specimen Descriptions 136
5.4 Image Registration Based on Maximization of Normalized Mutual Information 139
5.4.1 Background 139
5.4.2 Process 142
5.4.3 Results 144
5.5 Analyses 149
5.5.1 Image Segmentation 149
5.5.2 Saturation Profile 152
5.5.3 Pore Size Distribution and Coordination Number 155
5.5.4 Representative Elementary Volume Analysis 158
5.6 Conclusions 161
5.7 References 163
Chapter 6. Direct Numerical Simulation Based on Image Data 167
6.1 Abstract 169
6.2 Introduction 169
6.3 Full Morphology Method 171

6.3.1 Principles 171
6.3.2 Materials and Methods 174
6.3.3 Thresholding 175
6.3.4 Pore Size Distribution and Full Morphology Simulations 177
6.3.5 Effect of Contact Angle 180
6.4 Hydraulic Conductivity Simulation 182
6.4.1 Permeability and Hydraulic Conductivity 182
6.4.2 Materials and Methods 186
6.4.3 Representative Elementary Volume (REV) and Hydraulic Conductivity 187
6.4.4 Grain Shape Effect 188
6.5 Conclusion 191
6.6 References 192
Chapter 7. High Resolution Neutron Imaging of Flow through Compacted Porous Media 194
7.1 Abstract 196
7.2 Introduction 197
7.3 In-situ Flow Experiment through Compacted Sand 199
7.4 In-situ Flow Experiment through Dense and Loose States of Sand 201
7.4.1 Thermal neutron imaging at PSI 201
7.4.2 Imaging Setup and Parameters 202

7.4.3 Specimen Preparation 207
7.4.4 Flow Experiment Parameters.....208
7.4.5 Dual Modality 209
7.4.6 Flow Results 211
7.5 High Resolution In-situ Flow Experiment though Compacted Sand Specimens using Cold Neutrons 222
7.5.1 High Resolution Neutron and X-ray Imaging.....222
7.5.2 Specimen Preparation 223
7.5.3 Experimental Procedure 224
7.5.4 Dual Modality and Image Registration 227
7.5.5 Time-lapsed Radiography.....229
7.5.6 Pore Size Distribution and Capillary Rise 232
7.5.7 Degree of Saturation along Height of the Specimen.....236
7.5.8 Full Morphology Imbibition Simulation 237
7.6 Conclusions.....241
7.7 References.....243
Chapter 8. Conclusion and Future Work.....245
8.1 Conclusions.....246
8.2 Future Work.....248

LIST OF TABLES

Table 2.1: Neutron characteristics at various energy ranges (Herwig 2009).....25

Table 2.2: The four points representing pixel centers and the associated interpolation coefficients used in bilinear interpolation.....44

Table 3.1: Gravimetric water content (GWC), volumetric water content (VWC), total mass (mT) and void ratio (e) for each sand specimen.....73

Table 3.2: Neutron imaging experimental parameters.....74

Table 4.1: Measured silica sand and water phase compositions and liquid content of each specimen.....101

Table 4.2: Neutron macroscopic cross section and X-ray attenuation coefficient comparison of the 3 phases (Water, Air, and Silica).....103

Table 4.3: The imaging parameters of neutron and X-ray tomography.....107

Table 4.4: Void ratios obtained from phase relationship and tomography for Ottawa sand and Q-ROK sand.....119

Table 6.1: Porosity values at different threshold levels.....177

Table 6.2: Simulated hydraulic conductivity values of Ottawa and Q-ROK sand.....189

Table 7.1: Average total macroscopic cross section of water (Σ_w) and penetration depth for 3% penetration at NEUTRA (thermal neutron) and CONRAD (cold neutron) beam line.....202

Table 7.2: Neutron and X-ray imaging parameters used at PSI NEUTRA beam line 204
Table 7.3: Measured void ratios of dense and loose sand specimens 208
Table 7.4: Parameters used for the flow experiment through sand specimens prepared in dense and loose states 209
Table 7.5: X-ray and neutron imaging parameters used at HZB 223
Table 7.6: Water injection parameters for Ottawa sand and Q-ROK sand specimens 226
Table 7.7: Dimensions of ROIs used for analysis of pore size distribution and their porosity values 234

LIST OF FIGURES

Figure 1.1: Partially saturated soil at grain/pore scale, and negative capillary pressure of capillary bridges. 3

Figure 2.1: Mathematical model of monochromatic neutron attenuation where the neutrons are running through an object of thickness Δx with a constant total macroscopic cross section, Σ_T 29

Figure 2.2: Typical neutron imaging setup; neutron interaction mechanism with matter and the effect of L/D on image resolution 33

Figure 2.3: Neutron imaging setup at NIST 33

Figure 2.4: Projection process and coordinate system 36

Figure 2.5: Projection and backprojection of circular cross section 37

Figure 2.6: Simple backprojection of circular cross section with different number of projections 38

Figure 2.7: Fourier slice theorem 39

Figure 2.8: FBP of circular cross section for different number of projections 41

Figure 2.9: Binary system model 43

Figure 2.10: Bilinear interpolation model 44

Figure 2.11: FBP result of high resolution neutron tomography data of partially saturated sand sample 48

Figure 2.12: Comparison of original, filtered backprojection and iterative reconstruction (binary model with ART) result of 64 × 64 Shepp-Logan phantom.....49
Figure 2.13: Comparison of original, filtered backprojection and iterative reconstruction (interpolation model with ART) result of 64 × 64 Shepp-Logan phantom.....50
Figure 2.14: Comparison of filtered backprojection and iterative reconstruction (interpolation model) result of neutron tomography data of various holes filled with water 51
Figure 2.15: Interaction of matter with X-rays and neutrons (Strobl et al. 2009). (© IOP Publishing. Reproduced by permission of IOP Publishing. All rights reserved.).....53
Figure 2.16: Mass attenuation coefficients for thermal neutrons and100 keV x-rays for the elements. (Reprinted with permission from Kardjilov et al. (2006). Copyright (2006), IOS Press) 55
Figure 2.17: Attenuation coefficient comparison of water, air and sand phase for cold neutron and X-ray (100 keV).....56
Figure 2.18: Comparisons of X-ray energy and attenuation coefficients for water and silica.....58
Figure 2.19: Picture of the partially saturated sand specimen (a), radiography of partially saturated sand specimen showing 1X and 10X magnification FOV

size and location (b), tomography slice of partially saturated sand specimen at 1X magnification (c), and tomography slice of partially saturated sand specimen at 10X magnification (d).....59

Figure 2.20: Three dimensional visualization ($1mm^3$) of dry (a) and partially saturated (b) sand specimen at 10X magnification.....59

Figure 3.1: Cross section comparison of H_2O, O_2 and SiO_2 for neutrons and X-rays (1 b = 10^{-24} cm^2).....69

Figure 3.2: Picture of sand specimens contained in aluminum specimen holders and radiographs of Ottawa sand and Q-ROK sand 72

Figure 3.3: Morphology comparison of (a) Ottawa sand and (b) Q-ROK sand ...72

Figure 3.4: Grain Size distribution of Ottawa sand and Q-ROK sand 73

Figure 3.5: Image division process 76

Figure 3.6: Attenuation comparison of line A-A for 0%, 6%, 9%, and 12% gravimetric water content (GWC) Ottawa sand and Q-ROK sand 77

Figure 3.7: Contour plots of water content (WC) distribution from neutron radiography images 79

Figure 3.8: Contour plots of water saturation (WS) distribution on reconstructed tomography slices.....82

Figure 3.9: Comparison of standard deviation of histogram between Ottawa sand and Q-ROK sand 83

Figure 3.10: Comparison of the 3 compaction layers of top (A-A), middle (B-B) and bottom (C-C) for 12% GWC Ottawa sand 83
Figure 3.11: Maximum and average uncertainty of attenuation value comparison of Ottawa sand at GWC of 6%, 9%, and 12% 84
Figure 3.12: Effect of scattered neutrons on image formation from an infinite line charge 87
Figure 4.1: Specimen dimension and description 101
Figure 4.2: Microfocus X-ray system and high resolution neutron imaging setup at HZB 106
Figure 4.3: Contrast comparison of the three specimens shown from neutron radiographs and tomography slices 110
Figure 4.4: Comparison of water distribution resulting from different sand grain shape morphologies 111
Figure 4.5: Effect of compaction and grain shape morphology on void and water distribution 113
Figure 4.6: Dual modality of neutron and X-ray tomography data 115
Figure 4.7: Image processing sequence applied to segment the sand grain phase: (a) 3D median filter applied image, (b) Thresholding result by factorization method on the region of interest, (c) Result after opening algorithm applied, (d) Result after 3D watershed algorithm applied, (e) Labeled (color coded) image of individual sand grains 119

Figure 4.8: Void percentage over the height for Ottawa sand and Q-ROK sand 120
Figure 4.9: Local void ratio comparison of Ottawa sand and Q-ROK sand 121
Figure 4.10: Grain size distribution based on sand grain volume obtained from the X-ray tomography data 122
Figure 4.11: Visualization of the sand phase (a), and the water phase (b) in 3D 123
Figure 5.1: Picture of a specimen (a) and neutron radiograph (b) showing specimen description, compaction layer and region of interest 137
Figure 5.2: Histogram of the X-ray data after median filter (5×5×5) is applied .. 139
Figure 5.3: Definitions of marginal entropy, joint entropy and mutual information by using Venn diagrams 141
Figure 5.4: Illustration of registration process and result with super-positioned image of neutron and X-ray tomography slice 145
Figure 5.5: Three dimensional super-positioned views neutron and X-ray tomography data of the three specimens after image registrations are performed 146
Figure 5.6: Illustrative example of registration process and verification of the result by computing marginal entropies, mutual information and normalized mutual information for different angles of rotation 148

Figure 5.7: Process to segment water phases more accurately by using registered X-ray and neutron data 151
Figure 5.8: Pore volume, water volume and saturation over the height of the specimen 154
Figure 5.9: Pore size distribution for Ottawa sand with water and Q-ROK sand with water specimens 156
Figure 5.10: Coordination distribution for Ottawa sand with water and Q-ROK sand with water specimen..... 158
Figure 5.11: REV analysis of porosity 159
Figure 5.12: REV analysis of saturation 160
Figure 5.13: Example REV of 12% gravimetric water content Ottawa sand and Q-ROK sand at the third compaction layer with RVE volume of 3×3×3 mm^3. 161
Figure 6.1: Illustration of morphological opening step for drainage simulation shown with initial unsaturated state (a), fully saturated with WP (b), erosion step (c), connectivity to WP (d) and dilation step (e)..... 173
Figure 6.2: Picture of the aluminum compaction mold (a), X-ray radiography of dry Ottawa sand specimen (b), reconstructed slice (c), and 3D volume rendering of the dry Ottawa sand specimen segmented from X-ray tomography (d) 175
Figure 6.3: Histogram comparison for original data, and median 3D (3x3x3) filter applied and median 3D (5x5x5) filter applied..... 176

Figure 6.4: Different threshold values and binary results comparison.....177
Figure 6.5: Pore size distribution for different threshold values 178
Figure 6.6: Cumulative pore size distribution for different threshold values.....178
Figure 6.7: Capillary pressure – saturation curves for different threshold values 179
Figure 6.8: Capillary pressure – saturation curves for different threshold values magnified between capillary pressure of 1 kPa and 2 kPa 180
Figure 6.9: Effect of different contact angles on capillary pressure – saturation curves 181
Figure 6.10: Simulated two phase distribution for contact angle 0° 181
Figure 6.11: Darcy's law 184
Figure 6.12: Porosity variation for different REV side dimensions 187
Figure 6.13: Hydraulic conductivity for different size of REV 188
Figure 6.14: The number of iteration to reach convergence of Ottawa sand data 190
Figure 6.15: Simulated velocity profile Ottawa sand specimen at the edge (a) and around the area where high velocity is found (b).....190
Figure 7.1: Water injection system used for in-situ imaging at NIST.....200
Figure 7.2: Radiographs after incremental water flow steps showing through thickness attenuation as a function of location.....200

Figure 7.3: Example tomography slices at the flow front from top (a) to bottom (b) for the flow step 2 201
Figure 7.4: Experimental setup used at PSI NEUTRA beam line 205
Figure 7.5: Optical image of focusing mask (a), Gd mask used for neutron resolution determination for a given set of imaging parameters (b), Gd resolution mask magnified (c).....206
Figure 7.6: MTF of X-ray scintillator (OG4) (CAWO).....207
Figure 7.7: Dual-modal (neutron and X-ray) contrast of Ottawa dense specimen at flow step 1 shown from radiographs and reconstructed tomography slices 210
Figure 7.8: Time-lapsed radiographs of flow step 1 of Ottawa sand at dense state 212
Figure 7.9: Time-lapsed radiographs of flow step 2 of Ottawa sand at dense state 213
Figure 7.10: Time-lapsed radiographs of flow step 3 of Ottawa sand at dense state.....214
Figure 7.11: Time-lapsed radiographs of flow step 1 of Ottawa sand at loose state.....215
Figure 7.12: Time-lapsed radiographs of flow step 2 of Ottawa sand at loose state.....216

Figure 7.13: Time-lapsed radiographs of flow step 3 of Ottawa sand at loose state 217
Figure 7.14: Cross-sectional water distribution pattern of dense Ottawa sand specimen shown from reconstructed tomography slices from top, middle and bottom compaction layers for flow steps 1, 2 and 3 219
Figure 7.15: Cross-sectional water distribution pattern of loose Ottawa sand specimen shown from reconstructed tomography slices from top, middle and bottom location of the specimen for flow steps 1, 2 and 3 221
Figure 7.16: Aluminum flow chamber (a) and syringe pump (b) 224
Figure 7.17: Experimental setup used at CONRAD neutron imaging beam line 225
Figure 7.18: Three dimensional view of X-ray tomography data of the dry state, neutron data of the dry state, flow step 1, and flow step 2 of Ottawa sand at dense state 228
Figure 7.19: Dual modality contrast comparison of X-ray and neutron images and quality of image registration shown from small ROI volumes..... 228
Figure 7.20: High resolution time-lapsed neutron radiographs of flow step 1 of Ottawa sand specimen in dense state 230
Figure 7.21: High resolution time-lapsed neutron radiographs of flow step 2 of Ottawa sand specimen in dense state 231

Figure 7.22: High resolution time-lapsed neutron radiographs of flow step 1 of Q-ROK sand specimen in dense state.....232
Figure 7.23: Cumulative pore size distribution of the dense Ottawa sand specimen 234
Figure 7.24: Comparisons of pore size distribution of different ROIs (small pore volume (a), large pore volume (b), and entire volume (c)) 235
Figure 7.25: The degree of saturation along the height of the specimen for flow steps 1 and 2 of Ottawa sand (round) specimen in dense state 237
Figure 7.26: The variation of local saturation along the height of the specimen for flow steps 1 of Q-ROK sand (angular) specimen in dense state.....237
Figure 7.27: Simulated capillary pressure – saturation curve and solid (red), water (blue) and air (white) distribution by using full morphology method for Ottawa sand specimen in dense state 240
Figure 7.28: Neutron and X-ray super-positioned image compared with simulated two fluid phase distribution at similar saturation level 241

CHAPTER 1. INTRODUCTION AND LITERATURE REVIEW

1.1 Introduction

Granular materials are defined as large conglomerations of discrete macroscopic particles (Jaeger et al. 1996). They are large enough such that they are not subject to thermal motion fluctuation. For soil, cohesionless soil such as gravel and sand are in the category of granular materials. They are non-cohesive and the forces between them are essentially only repulsive so that the shape of the material is determined by external boundaries and gravity.

Soil is a three phase material composed of discrete solid particles, pore water and air. The interactions between the different phases are of a critical importance in understanding soil deformation and fluid flow behaviors. An arrangement of the three phases can be very complex, and it is very difficult to quantify.

Structure of soil is defined as the combined effects of fabric, composition, and interparticle forces (Mitchell and Soga 2005). The fabric refers to the arrangement of solid particles in soil. Force is transferred through contact points of soil particles, and the fabric governs the load deformation behavior. Additionally, liquid phase forms capillary bridges and thin films around soil particles when partially saturated due to complex interaction with solid and pore air phases as shown in Figure 1.1. Partially saturated or unsaturated soil mechanics have been studied by various researchers, and the effects of interparticle forces are analyzed carefully (Bishop et al. 1960; Kim and Sture

2004; Kim and Sture 2008; Lu et al. 2009; Lu and Likos 2006; Lu et al. 2007). For sandy soil to be studied in this research, the capillary forces dominate as the interparticle force. The negative pressure of the capillary bridge adds additional cohesive force between the touching sand particles which did not exist in dry soil, and it increases the resistance of the soil. Thus, the distribution of water in soil is important to understand the shear strength of partially saturated soil. The distribution of water in the pore space of soil and rock also fundamentally affects the conductivity and diffusivity properties (Berkowitz and Hansen 2001).

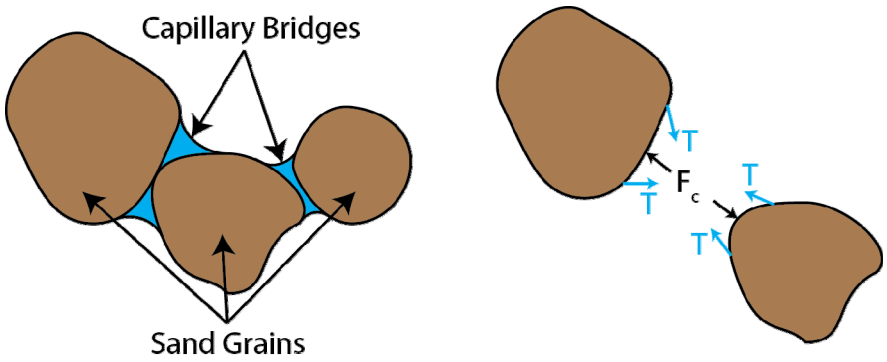


Figure 1.1: Partially saturated soil at grain/pore scale, and negative capillary pressure of capillary bridges.

Partially saturated soil mechanics can be studied experimentally by generating moisture suction curve from experiments such as hanging column tests. The curve relates suction value to saturation of soil. It provides information between dry and fully saturated state of soil. The effect of suction has been

studied extensively by various researchers (Fredlund and Rahardjo 1993; Hoyos 2013). However, the experimental determination of moisture suction curve is very time consuming especially for smaller pore size and fine grained soils.

The discrete nature of solid particles of soil is another important aspect. The solid particles in soil are not bonded together as strong as crystals in a metal are, each particle is relatively free to move with respect to one another. However, the soil particles are solid and cannot move as easily as the elements in a fluid. Soil is a particulate system. Thus, neither solid mechanics nor fluid mechanics can be used to study granular materials (Lambe and Whitman 1969). The contact force between soil particles will cause individual particles to deform, and in some cases, particle crushing can occur at higher stress levels. Once the shear force at contact becomes larger than the shear resistance at the contact, a relative particle sliding can occur. The overall strain of a soil mass will be partly the result of deformation of individual particles and partly the result of relative sliding between particles. Thus, the phenomena at the contact points are the fundamental to study of soils. The concept of friction and adhesion between particles should be considered. However, there are so many contact points within a granular system, and it is practically impossible to build up the stress-strain relationship at all contacts even if one knows what the relationship is. Hence, traditional continuum assumption has been applied for interpreting soil and granular mechanics experiments, related theories and numerical simulation at a

laboratory specimen scale. However, granular media do not behave as continua at the particle scale, and it is difficult to assume granular media as continua (Peters 2005). Mechanical tests such as triaxial tests are good ways to get mechanical behaviors of the granular system. However, mechanical testing can only reveal the load applied at the boundary of the sample and its global displacement. The failure mechanism is still largely unknown. The microstructure needs to be studied to understand the failure mechanism.

The discrete nature of granular materials was accounted with a numerical simulation method such as discrete element method (DEM), and the technique has been applied popularly (Bardet and Proubet 1991; Cundall and Strack 1979; Iwashita and Oda 1998; Yimsiri and Soga 2010).

Flow through porous media such as soil is also a complex problem. Experimental approach to study flow phenomenon is challenging especially at the pore scale. The initial state of pore structure has significant effect on the flow pattern. It is important to determine the proper physical (comprehensive descriptions of the pore and particle space as well as mechanical properties), hydraulic (flow of fluids through the medium), transport (diffusion, electrical conductivity, dispersion, and advection of both sorbing and nonsorbing solutes) properties (Hunt and Ewing 2009). When transport properties are determined, an arithmetic means are often computed which assumes the perfect connectivity. The natural porous media is very complex and variable. One of the approaches

has been to predict hydraulic properties from physical properties, then to predict transport properties from the physical and hydraulic properties.

Modeling of flow through porous media is rather complex, and simplification assumptions have been made such as continuum assumption (Abriola and Pinder 1985; Miller et al. 1998) or stochastic reconstruction (Kainourgiakis et al. 2000; ØRen and Bakke 2002; Yeong and Torquato 1998a; Yeong and Torquato 1998b). Three dimensional image data of real or idealized structure of granular materials have been used to simulate the flow through porous media at pore scale (Arns et al. 2001; Hazlett et al. 1998; Schulz et al. 2007). As significant progress was made with numerical simulation techniques performed at the grain/pore scale, the numerical simulation results need to be validated and improved with experimental results at grain/pore scale. Such grain/pore scale experimental results are still lacking.

In recent years, various experimental imaging techniques were used to visualize the interior microstructure of the granular system at the grain/pore level. The imaging techniques include optical microscopy, scanning electron microscopy (SEM), X-ray and neutron tomography have been used to study granular materials (Al-Raoush and Alshibli 2006; Desrues et al. 1996; Kim et al. 2012; Muhunthan and Chameau 1997; Oda 1972a; Oda 1972b; Oda 1972c; Otani 2010; Razavi et al. 2007; Wang et al. 2004; Yang 2005). Some of the literatures will be reviewed more carefully in the literature review section.

Different imaging modalities often show different features at different spatial resolutions/Field of View (FOV).

Optical microscopy or SEM imaging of soil provides high spatial resolution at a small FOV. However, it requires a destructive process of resin impregnation and serial sectioning for soil specimen. During the preparation process, the original structure of the sample may be disturbed.

On the other hand, X-ray radiography and tomography techniques are non-destructive since they can penetrate through materials. X-ray imaging technique often shows good contrast of the sand grain phase, and high spatial resolution can be achieved. However, it usually does not show good contrast of water phase at the energy of X-ray typically used to image larger soil specimens. Thus, a contrast agent such as Cesium Chloride (CsCl) is often added to improve the contrast of the liquid. The addition of such salt can possibly change the contact angle of between solid and liquid interface. Also, adding a contrast agent is not an option for studying samples from the environment.

Recently, neutron imaging technique has made significant improvements with spatial and temporal resolution. Unlike X-rays, neutron shows high contrast to water, and it is easy to identify the location of water in soil specimen. However, it does not show as good contrast of the soil particles. Thus, neutron imaging technique is becoming a complementary imaging technique to X-ray imaging technique for studying partially saturated soil. Out of the three phases of soil

(solid, liquid and gas), the silica solid phase can be identified with X-ray imaging and the water phase can be identified with neutron imaging. The details of X-ray and neutron imaging technique are explained in the upcoming chapters.

In this dissertation, procedures taken and results obtained with simultaneous or sequential use of neutron and X-ray imaging techniques to experimentally study partially saturated sand and flow through compacted sand are presented.

In Chapter 2, comprehensive explanation is provided for X-ray and neutron imaging techniques used in this research. The principles of computed tomography reconstruction are presented thoroughly with conventional filtered backprojection algorithms and more complicated algebraic reconstruction algorithm based on an iterative method. The motive of dual modality (neutron and X-ray) imaging approach is presented with its potentials for studying soil.

In Chapter 3, experimental results to visualize water distribution in partially saturated compacted sand data obtained from neutron imaging facility of National Institute of Standards and Technology (NIST) are presented. At a relatively coarse spatial resolution (250 μm), different water contents (0 %, 6 %, 9 %, and 12 %) of partially saturated Ottawa (round) and Q-ROK (angular) sand specimens were imaged with neutron radiography and tomography. A quantitative approach to visualize local water content distribution in the interior of the sand specimens was performed with both radiography and tomography data.

In Chapter 4, high resolution neutron and X-ray tomography results of partially saturated compacted sand specimens are presented. High spatial resolution (~39 μm) of neutron imaging is achieved by using a thin (10 μm) gadox scintillator with a lens (1:1 magnification) coupled CCD camera. Slightly higher spatial resolution (~ 22 μm) X-ray tomography data of the same specimen was also obtained at 100 kV source voltages. Dual-modal contrast of the three phases is presented at grain scale. Image processing procedure used to segment the X-ray data is presented, and the analysis results are shown.

In Chapter 5, the high resolution neutron and X-ray tomography data presented in Chapter 4 was combined into the same coordinates by using image registration technique. The neutron and X-ray data are taken with different imaging systems, their resolution, pixel size, and specimen orientation are different. By using an automatic metric of maximization of normalized mutual information, the two data sets were combined in the same coordinates. Based on the registration results, water phase of neutron tomography data was segmented more accurately by using the sand grain boundary obtained with X-ray tomography data. Based on the combined information of water phase and pore phase, the degree of saturation over the height of the specimen is obtained.

In Chapter 6, X-ray tomography image based direct numerical simulation approach was also performed to predict engineering properties. Full morphology method was studied and used to simulate capillary pressure – saturation curve

for drainage condition, and simulated two fluid phase distribution for different capillary pressure. The effect of image threshold on the simulated capillary pressure – saturation curve was investigated. The effect of choice of contact angle for the method is also investigated. Permeability was simulated based on the X-ray tomography image data. Permeability of different size of Representative Elementary Volume was compared. Permeability coefficients of Ottawa sand and Q-ROK sand were also compared.

In Chapter 7, results of in-situ imaging experiment of flow through sand specimens are presented. In-situ flow experiment imaging results obtained at different neutron imaging facilities (NIF at NIST, NEUTRA at PSI and CONRAD at HZB) are presented. Flow patterns of dense and loose states of Ottawa sand are compared with time-lapsed neutron radiography and tomography after each flow step. Similar flow experiments are also performed on dense Ottawa and Q-ROK sand specimens at high spatial resolution. High resolution X-ray tomography data of initial dry state of sand specimens are additionally obtained at similar spatial resolution. Based on image registration of neutron and X-ray data, sand/pore information is obtained from X-ray tomography data and water information is obtained from neutron tomography data. Water distribution of Ottawa sand and Q-ROK sand are compared. Full morphology method is also used to simulate water flow pattern of imbibition.

In Chapter 8, conclusions and future work are presented.

1.2 Literature Review

Imaging requires comprehensive understanding of various aspects including beam generation, radiation detection, image reconstruction, image processing, 3D visualization and image analysis. The radiation based techniques have been used on soil and granular materials for various applications. This section will focus on previous application of neutron and X-ray imaging on soil and granular media to further improve the understanding.

Some historical background will be provided here. In 1895, X-rays were first discovered by Röntgen, and the first X-ray image of Röntgen's wife's hand was presented (Röntgen 1896). Radon established theoretical foundation of computed tomography (CT) in 1917 (Radon 1917; Radon 1986). Neutron was first discovered by Chadwick in 1932 (Chadwick 1932a; Chadwick 1932b). The first reactor was built by Fermi for neutron production in 1942. In 1947, the first neutron images were obtained by Kallmann (Kallmann 1947). Neutron imaging at research reactor was performed by Thewlis in 1956 (Thewlis 1956).

In 1963 and 1964, Cormack partially rediscovered Radon's idea and applied them to CT (Cormack 1963; Cormack 1964). Hounsfield and colleagues built the first medical CT machine (Hounsfield 1973). Cormack and Hounsfield shared the 1979 Nobel Prize in Medicine. In 1970, X-ray tomography started performing at hospitals. In 1980s, dedicated Synchrotron light sources which generate intense X-ray beam were built.

Several scientists started using X-ray to study soils. Coumoulos had studied soil with γ-ray and X-ray radiography in 1968, and Roscoe had presented some of the results in 1975 (Coumoulos 1968; Roscoe 1970). Void ratio during dilation has been visualized with X-ray radiographs.

Wellington and Vinegar have performed X-ray CT on a core for petroleum engineering application in 1987 by using a medical scanner (Wellington and Vinegar 1987). Three dimensional measurements of petrophysical applications including density and porosity, correlation of core logs with well logs, characterization of mud invasion, fractures, and disturbed cores were performed.

Jasti et al. have studied several porous media with X-ray tomography (Jasti et al. 1993). A micro focus X-ray system was used instead of medical scanner, and much higher spatial resolution was achieved. A glass bead pack, Berea sandstone samples with different air permeability, and Texas creme chalk were imaged. An example water flooding experiment involving glass bead, water, and hexadecane doped with iodohexadecane which contained 5% iodine. Iodine has high contrast to X-rays. The three phases were shown with good contrast.

Desrues et al. studied shear bands and strain localization in triaxial tests on dense sand by using X-ray CT (Desrues et al. 1996). The localization pattern involving a central cone and set of pairs was obtained from CT images. Local void ratio evolution at the shear band zone was different from global void ratio of the specimen.

Alshibli et al. have performed X-ray tomography to study shear band formation (Alshibli et al. 2000). The internal fabric and localized deformation patterns of triaxial sand specimens studied. Triaxial tests were conducted in a microgravity environment on a Space Shuttle. Multiple symmetrical radial shear bands were observed in the specimen tested in the microgravity environment, but nonsymmerical spatial deformation was observed in the specimen tested in the normal gravity environment.

Al-Raoush and Alshibli have developed a methodology to calculate distribution of local void ratio in porous media system from 3D data (Al-Raoush and Alshibli 2006). A combination of watershed transform and distance transform is to calculate the local void ratio. Local void ratio was calculated from X-ray micro tomography data of glass beads.

Matsushima et al have studied lunar soil with X-ray tomography taken at Spring-8 Synchrotron radiation facility (Matsushima et al. 2009a). Image processing algorithm was developed to segment individual sand grains. Based on the result, grain size distribution and grain shape properties were obtained. DEM simulation was further applied based on image data.

Neutron imaging technique was also used to study soils by various researchers. Lewis and Krinitzsky have performed a 2D radiography study on a thin soil layer for moisture distribution study using a Californium – 252 source (Lewis and Krinitzsky 1976). Californium source is a relatively weak source, and

it took 16 hours to obtain an image using film technology. It was possible to visualize the water content difference from top and bottom of the sample. Tomographic imaging was yet to be applied on neutron imaging. This work was the earlier work using neutron imaging to study soil the author was able to find.

Jasti and Fogler have performed acid etching of limestone and sandstone with neutron radiography (Jasti and Fogler 1992). The high contrast hydrogen and water to thermal neutron was used to visualize the fluid. Relatively fast imaging was performed to visualize miscible dispersion process in-situ.

Pleinert and Degueldre performed a feasibility study to measure porosity of crystalline rock samples with neutron radiography (Pleinert and Degueldre 1995). The water content of granodiorite and mylonite samples was determined by quantitative neutron radiography combined with densitometric scanning.

Lopes et al performed a neutron tomography experiment on compacted soil samples (Lopes et al. 1999). They compared compacted soil samples with varying global water contents of 7.8 to 14.8 %. The spatial resolution was too coarse to visualize the specimen at the grain/pore level.

De Beer and Middleton studied two phase flow in porous concrete using a Hassler cell to simulate petroleum recovery (de Beer and Middleton 2006). The Hassler cell is used to reproduce deep reservoir pressure conditions. Heavy water (D_2O) was used to improve contrast against petroleum.

Hassanein et al. performed an investigation of water imbibition with thermal neutron radiography (Hassanein et al. 2006). Water sorption and dehydration with and without salt in three different limestones from the United States were investigated.

Carminati et al. performed a water flow experiment to study non-uniform flow through soil aggregates (Carminati et al. 2007). Water flow through aggregates was focused, and the water exchange between soil aggregates was monitored by neutron radiography.

Kardjilov et al. have presented the high resolution neutron tomography capability at CONRAD beam line at HZB (Kardjilov et al. 2011). The high resolution was achieved by using a thin (10 μm) gadox scintillator, 1:1 magnification lens and high resolution CCD camera. One of the author's specimens is presented as an example to present the high spatial resolution and dual modality.

Dual-modal contrast obtained from neutron and X-ray images have been reported for various materials. Manke et al. have compared neutron and synchrotron X-ray radiographies of PEM fuel cell (Manke et al. 2011). Synchrotron tomography and neutron tomography of a battery is also compared. Different material was studied with different imaging modalities.

Matsushima et al. have studied rose bent neck syndrome with both cold neutron and Synchrotron X-ray imaging techniques (Matsushima et al. 2009b).

Neutron radiography and tomography was used to visualize water and heavy water intake pattern, and Synchrotron X-ray tomography data revealed the structures of vascular bundles and parenchyma cells of pith in rose peduncle were clearly observed.

Borehole rock samples were investigated by both neutron and X-ray (Christe et al. 2007). Out of the few rock samples tested, sand stone showed good contrast for both neutron and X-ray.

Adler et al. (1990) generated artificial pore geometry to predict permeability. Average statistical properties of pore space of Fontainebleau sandstone are measured from thin sections, and artificial pore geometry is generated based on these statistical properties. The Stokes flow of Newtonian fluid was determined by a finite-difference scheme in three dimensions.

Auzerais et al. (1996) have estimated porosity, pore-volume-to surface ratio, permeability, end point relative permeability , electrical resistivity and wetting phase residual saturation by using high resolution image of the microstructure of Fontainebleau sandstone (Auzerais et al. 1996).

Hydraulic property of porous media such as the capillary pressure-saturation relation and hydraulic conductivity function based on X-ray tomography images are performed (Vogel et al. 2005).

Two-dimensional and three-dimensional lattice Boltzmann models were developed, and the three-dimensional model was applied on the pore geometry

of compacted aggregates and asphalt specimens generated from X-ray Computed Tomography to estimate hydraulic characteristic such as permeability (Kutay et al., 2006).

1.3 References

Abriola, L. M., and Pinder, G. F. (1985). "A Multiphase Approach to the Modeling of Porous Media Contamination by Organic Compounds: 1. Equation Development." *Water Resources Research*, 21(1), 11-18.

Al-Raoush, R., and Alshibli, K. A. (2006). "Distribution of Local Void Ratio in Porous Media Systems from 3D X-ray Microtomography Images." *PHYSICA A*, 361(2), 441-456.

Alshibli, K. A., Sture, S., Costes, N. C., Frank, M. L., Lankton, M. R., Batiste, S. N., and Swanson, R. A. (2000). "Assessment of Localized Deformations in Sand Using X-Ray Computed Tomography." *Geotecnical Testing Journal*, 23(3), 274-299.

Arns, C. H., Knackstedt, M. A., Pinczewski, M. V., and Lindquist, W. B. (2001). "Accurate estimation of transport properties from microtomographic images." *Geophys. Res. Lett.*, 28(17), 3361-3364.

Auzerais, F. M., Dunsmuir, J., Ferréol, B. B., Martys, N., Olson, J., Ramakrishnan, T. S., Rothman, D. H., and Schwartz, L. M. (1996). "Transport in sandstone: A study based on three dimensional microtomography." *Geophys. Res. Lett.*, 23(7), 705-708.

Bardet, J. P., and Proubet, J. (1991). "A Numerical Investigation of the Structure of Persistent Shear Bands in Granular Media." *Géotechnique*, 41(4), 599-613.

Berkowitz, B., and Hansen, D. P. (2001). "A Numerical Study of the Distribution of Water in Partially Saturated Porous Rock." *Transport in Porous Media*, 45, 303-319.

Bishop, A. W., Alan, I., Blight, G. E., and Donald, I. B. (1960). "Factors controlling the strength of partially saturated cohesive soils." *Research conference on shear strength of cohesive soils* University of Colorado, Boulder, CO, 500-532.

Carminati, A., Kaestner, A., Ippisch, O., Koliji, A., Lehmann, P., Hassanein, R., Vontobel, P., Lehmann, E., Laloui, L., Vulliet, L., and Flühler, H. (2007). "Water flow between soil aggregates." *Transport in Porous Media*, 68(2), 219-236.

Chadwick, J. (1932a). "The existence of a neutron " *Proceedings of the Royal Scociety A: Mathematical, Physical & Engineering Sciences*, 136, 692-708.

Chadwick, J. (1932b). "Possible existance of a neutron." *Nature*, 129(3252), 312.

Christe, P., Bernasconi, M., Vontobel, P., Turberg, P., and Parriaux, A. (2007). "Three-dimensional petrographical investigations on borehole rock samples: a comparison between X-ray computed- and neutron tomography." *Acta Geotechnica*, 2(4), 269-279.

Cormack, A. M. (1963). "Representation of a Function by Its Line Integrals, with Some Radiological Applications." *Journal of Applied Physics*, 34(9), 2722-2727.
Cormack, A. M. (1964). "Representation of a Function by Its Line Integrals, with Some Radiological Applications. II." *Journal of Applied Physics*, 35(10), 2908-2913.
Coumoulos, D. G. (1968). "A radiographic study of soils," Cambridge University, Cambridge, UK.
Cundall, P. A., and Strack, O. D. L. (1979). "A discrete numerical model for granular assemblies." *Géotechnique*, 29(1), 47-65.
de Beer, F. C., and Middleton, M. F. (2006). "Neutron Radiography Imaging, Porosity and Permeability in Porous Rocks." *South African Journal of Geology*, 109(4), 541-550.
Desrues, J., Chambon, R., Mokni, M., and Mazerolle, F. (1996). "Void ratio evolution inside shear bands in triaxial sand specimens studied by computed tomography." *Géotechnique*, 46(3), 529-546.
Fredlund, D. G., and Rahardjo, H. (1993). *Soil Mechanics for Unsaturated Soils* John Wiley & Sons.
Hassanein, R., Meyer, H. O., Carminati, A., Estermann, M., Lehmann, E., and Vontobel, P. (2006). "Investigation of Water Imbibition in Porous Stone by Thermal Neutron Radiography." *Journal of Physics D: Applied Physics*, 39(19), 4284-4291.
Hazlett, R. D., Chen, S. Y., and Soll, W. E. (1998). "Wettability and rate effects on immiscible displacement: Lattice Boltzmann simulation in microtomographic images of reservoir rocks." *Journal of Petroleum Science and Engineering*, 20(3-4), 167-175.
Hounsfield, G. N. (1973). "Computerized transverse axial scanning (tomography): Part 1. Description of system." *British Journal of Radiology*, 46(552), 1016-1022.
Hoyos, L. (2013). "Recent Advances in Experimental Modelling of Unsaturated Soil Behaviour over a Whole Range of Paths and Modes of Deformation." Multiphysical Testing of Soils and Shales, L. Laloui and A. Ferrari, eds., Springer Berlin Heidelberg, 3-20.
Hunt, A., and Ewing, R. (2009). *Percolation Theory for Flow in Porous Media*, Springer, Berlin Heidelberg.
Iwashita, K., and Oda, M. (1998). "Rolling Resistance at Contacts in Simulation of Shear Band Development by DEM." *Journal of Engineering Mechanics*, 124(3), 285-292.
Jaeger, H. M., Nagel, S. R., and Behringer, R. P. (1996). "Granular solids, liquids, and gases." *Reviews of Modern Physics*, 68(4), 1259.
Jasti, J. K., and Fogler, H. S. (1992). "Application of neutron radiography to image flow phenomena in porous media." *AIChE Journal*, 38(4), 481-488.

Jasti, J. K., Jesion, G., and Feldkamp, L. (1993). "Microscopic imaging of porous media with X-ray computer tomography." *SPE Formation Evaluation*, 8(3), 189-193.

Kainourgiakis, M. E., Kikkinides, E. S., Steriotis, T. A., Stubos, A. K., Tzevelekos, K. P., and Kanellopoulos, N. K. (2000). "Structural and Transport Properties of Alumina Porous Membranes from Process-Based and Statistical Reconstruction Techniques." *Journal of Colloid and Interface Science*, 231(1), 158-167.

Kallmann, H. (1947). *Research*, 1, 254.

Kardjilov, N., Dawson, M., Hilger, A., Manke, I., Strobl, M., Penumadu, D., Kim, F. H., Garcia-Moreno, F., and Banhart, J. (2011). "A Highly Adaptive Detector System for High Resolution Neutron Imaging." *Nuclear Instruments and Methods in Physics Research Section A: Accelerators, Spectrometers, Detectors and Associated Equipment*, 651(1), 95-99.

Kim, F. H., Penumadu, D., and Hussey, D. S. (2012). "Water Distribution Variation in Partially Saturated Granular Materials Using Neutron Imaging." *Journal of Geotechnical and Geoenvironmental Engineering, American Society of Civil Engineers (ASCE)*, 138(2), 147-154.

Kim, T.-H., and Sture, S. (2004). "Effect of Moisture on Attraction Force in Beach Sand." *Marine Georesources & Geotechnology*, 22(1-2), 33-47.

Kim, T.-H., and Sture, S. (2008). "Capillary-induced tensile strength in unsaturated sands." *Canadian Geotechnical Journal*, 45(5), 726-737.

Lambe, T. W., and Whitman, R. V. (1969). *Soil Mechanics*, John Wiley & Sons.

Lewis, J. T., and Krinitzsky, E. L. (1976). "Neutron Radiation in the Study of Soil and Rock." Practical Applications of Neutron Radiography and Gaging, H. Berger, ed., American Society for Testing and Materials, Baltimore, Md, 241-251.

Lopes, R. T., Bessa, A. P., Braz, D., and de Jesus, E. F. O. (1999). "Neutron computerized tomography in compacted soil." *Applied Radiation and Isotopes*, 50(2), 451-458.

Lu, N., Kim, T., Sture, S., and Likos, W. (2009). "Tensile Strength of Unsaturated Sand." *Journal of Engineering Mechanics*, 135(12), 1410-1419.

Lu, N., and Likos, W. (2006). "Suction Stress Characteristic Curve for Unsaturated Soil." *Journal of Geotechnical and Geoenvironmental Engineering*, 132(2), 131-142.

Lu, N., Wu, B., and Tan, C. P. (2007). "Tensile Strength Characteristics of Unsaturated Sands." *Journal of Geotechnical and Geoenvironmental Engineering*, 133(2), 144-154.

Manke, I., Markötter, H., Tötzke, C., Kardjilov, N., Grothausmann, R., Dawson, M., Hartnig, C., Haas, S., Thomas, D., Hoell, A., Genzel, C., and Banhart, J. (2011). "Investigation of Energy-Relevant Materials with Synchrotron X-Rays and Neutrons." *Advanced Engineering Materials*, 13(8), 712-729.

Matsushima, T., Katagiri, J., Uesugi, K., Tsuchiyama, A., and Nakano, T. (2009a). "3D Shape Characterization and Image-Based DEM Simulation of the Lunar Soil Simulant FJS-1." *Journal of Aerospace Engineering*, 22(1), 15-23.

Matsushima, U., Graf, W., Zabler, S., Kardjilov, N., and Herppich, W. B. (2009b). "Application of cold neutron and synchrotron X-ray imaging to investigate rose bent neck syndrome." *Acta Hort. (ISHS)*, 847, 279-286.

Miller, C. T., Christakos, G., Imhoff, P. T., McBride, J. F., Pedit, J. A., and Trangenstein, J. A. (1998). "Multiphase flow and transport modeling in heterogeneous porous media: challenges and approaches." *Advances in Water Resources*, 21(2), 77-120.

Mitchell, J. K., and Soga, K. (2005). "Fundamentals of Soil Behavior (3rd Edition)." John Wiley & Sons.

Muhunthan, B., and Chameau, J. L. (1997). "Void Fabric Tensor and Ultimate State Surface of Soils." *Journal of Geotechnical and Geoenvironmental Engineering*, 123(2), 173-181.

Oda, M. (1972a). "Initial Fabrics and Their Relations to Mechanical Properties of Granular Material." *Soils and Foundations*, 12(1), 17-36.

Oda, M. (1972b). "The Mechanism of Fabric Changes During Compressional Deformation of Sand." *Soils and Foundations*, 12(2), 1-18.

Oda, M. (1972c). "Deformation Mechanism of Sand in Triaxial Compression Tests." *Soils and Foundations*, 12(4), 45-63.

ØRen, P.-E., and Bakke, S. (2002). "Process Based Reconstruction of Sandstones and Prediction of Transport Properties." *Transport in Porous Media*, 46(2), 311-343.

Otani, J. (2010). "X-ray Computed Tomography for Geotechnical Engineering." Advances in X-ray Tomography for Geomaterials, J. Desrues, C. Viggiani, and P. Bésuelle, eds., ISTE Ltd, London, UK, 95-115.

Pleinert, H., and Degueldre, C. (1995). "Neutron radiographic measurement of porosity of crystalline rock samples: a feasibility study." *Journal of Contaminant Hydrology*, 19(1), 29-46.

Radon, J. (1917). "Über die Bestimmung von Funktionen durch ihre Integralwerte längs gewisser Mannigfaltigkeiten." *Berichte Sächsische Akademie der Wissenschaften*, 69, 262–277.

Radon, J. (1986). "On the determination of functions from their integral values along certain manifolds." *Medical Imaging, IEEE Transactions on*, 5(4), 170-176.

Razavi, M. R., Muhunthan, B., and Al Hattamleh, O. (2007). "Representative elementary volume analysis of sands using X-ray computed tomography." *ASTM Geotechnical Testing Journal*, 30(3), 212-219.

Röntgen, W. C. (1896). "On a New Kind of Rays." *Science*, 3(59), 227-231.

Roscoe, K. H. (1970). "The influence of strains in soil mechanics." *Géotechnique*, 20(2), 129-170.
Schulz, V. P., Becker, J., Wiegmann, A., Mukherjee, P. P., and Wang, C.-Y. (2007). "Modeling of Two-Phase Behavior in the Gas Diffusion Medium of PEFCs via Full Morphology Approach." *Journal of The Electrochemical Society*, 154(4), B419-B426.
Thewlis, J. (1956). "Neutron radiography." *British Journal of Applied Physics*, 7(10), 345.
Vogel, H.-J., Tölke, J., Schulz, V. P., Krafczyk, M., and Roth, K. (2005). "Comparison of a Lattice-Boltzmann Model, a Full-Morphology Model, and a Pore Network Model for Determining Capillary Pressure–Saturation Relationships." *Vadose Zone J.*, 4(2), 380-388.
Wang, L. B., Frost, J. D., and Lai, J. S. (2004). "Three-Dimensional Digital Representation of Granular Material Microstructure from X-Ray Tomography Imaging." *Journal of Computing in Civil Engineering*, 18(1), 28-35.
Wellington, S. L., and Vinegar, H. J. (1987). "X-Ray Computerized Tomography." *Journal of Petroleum Technology*, 39(8), 885-898.
Yang, X. (2005). "Three-Dimensional Characterization of Inherent and Induced Sand Microstructure," Gerogia Institute of Technology.
Yeong, C. L. Y., and Torquato, S. (1998a). "Reconstructing random media." *Physical Review E*, 57(1), 495-506.
Yeong, C. L. Y., and Torquato, S. (1998b). "Reconstructing random media. II. Three-dimensional media from two-dimensional cuts." *Physical Review E*, 58(1), 224-233.
Yimsiri, S., and Soga, K. (2010). "DEM analysis of soil fabric effects on behaviour of sand." *Géotechnique*, 60(6), 483-495.

CHAPTER 2. X-RAY AND NEUTRON IMAGING

2.1 Abstract

In this chapter, important background information related to author's PhD research is provided. Characteristics of X-ray and neutron are introduced and basics of radiation based imaging are summarized. Lambert – Beer's Law that is fundamental to analysis and tomography reconstruction is explained. Principles of reconstruction are explained, and two different types of reconstruction methods are presented. Motives and limitations of dual modality imaging technique to be used in this research are presented.

2.2 X-ray and Neutron

X-ray is a form of electromagnetic radiation. X-rays are in the range of 100 eV to 100 keV which corresponds to wavelengths range of 0.1 to 100 Å. X-ray can be generated from X-ray tubes, and it is readily available for imaging. Synchrotron light sources can generate very intense and bright X-ray for high spatial resolution even for a monochromatic beam. The energy of X-ray photon and wavelength follows the relationship shown in equation 2.1 where h = 6.6260755(40) × 10^{-34} J·s denotes Planck's constant and c = 2.99792458 × 10^{8} m/s denotes the speed of light.

$$E = \frac{hc}{\lambda} \tag{2.1}$$

A neutron is an electrically neutral subatomic particle with a mass slightly greater than a proton. It has both a wave and a particle state called wave-particle

duality. Unlike X-rays, neutron's wavelength and energy follows de Broglie wavelength of equation 2.2 and 2.3 respectively where *h* is the Planck's constant, m_n = 1.6749 × 10^{-27} kg and *v* is the neutron velocity. A neutron with an energy characteristic of room temperature (300 K) corresponding to 25.85 meV will have a velocity of 2224 m/s and a wavelength of 0.18 nm. For the same wavelength of X-ray photon would have energy of 6.89 keV. When neutron is generated, it has high energy of several MeV. The neutrons are often moderated to lower energy where the interaction with material is higher. Neutron classifications are shown in Table 2.1. Most neutron imaging beam lines use thermal or cold neutrons.

$$\lambda = \frac{h}{m_n v} \qquad 2.2$$

$$E = \frac{1}{2} m_n v^2 \qquad 2.3$$

Table 2.1: Neutron characteristics at various energy ranges (Herwig 2009).

Neutron Classification	Energy, *E* (MeV)	Velocity, *v* (m/s)	Wavelength, *λ*(nm)
Ultra-cold	0.00025	6.9	57
Cold	1	437	0.9
Thermal	25	2187	0.18
Epithermal	1000	13832	0.029

2.3 Interaction Mechanism

Both X-rays and neutrons can interact with a material by absorption, scattering, and penetration. The amounts of radiation that do not get absorbed or scattered are penetrating.

For X-rays, the interaction can be through photoabsorption, Compton scattering, and Rayleigh (or coherent) scattering. The amount of photoabsorption, Compton scattering and Rayleigh scattering depends on the energy of X-rays and the elemental composition of the material. Details of individual interaction mechanism are available from other references (Bushberg et al. 2003; Knoll 2000).

For neutrons, the interactions are scattering and absorption as well. Scattering involves inelastic and elastic scattering. Neutron interaction is with the nucleus, and the scattering cross section is random for not only on the individual element but also on the particular isotope of that element. In a coherent scattering process, neutron waves that are scattered by different nuclei combine with one another to produce an interference pattern that depends on the relative locations of the atoms in the material. Incoherent scattering may arise when more than one isotope is present in the sample or when a given isotope has a non-zero nuclear spin (Herwig 2009).

The amount of attenuation is the sum of absorption and scattering. It can be described by cross section. A cross section is an effective interaction area.

The microscopic cross section is typically expressed in the unit of barn (1 barn = 10^{-24} cm^2).

Each element has microscopic cross section (σ). There are microscopic cross sections for absorption and scattering in case of neutron imaging. In X-ray imaging, there are contribution from photoabsorption, Compton scattering, and Rayleigh scattering. The total microscopic cross section (σ_t) can be converted to total macroscopic cross section (Σ_T) for neutron or attenuation coefficient (μ) by multiplying with number density (*N*) as shown in equation 2.4.

$$\Sigma = N \cdot \sigma \qquad 2.4$$

2.4 Lambert – Beer's Law

The image formation process of neutrons and X-rays shares common theory and mathematics. Both X-ray and neutron imaging assumes linear attenuation of the penetrating radiation particles. When a radiation particle interacts with a material, it can be absorbed, scattered or penetrating as mentioned earlier. The particles do not get absorbed or scattered penetrates through material. The amount of attenuation is the sum of scattering and absorption. The attenuation is represented with the attenuation coefficient (μ) for X-ray imaging or the total macroscopic cross section (Σ_T) for neutron imaging. The total macroscopic cross section is the sum of absorption (Σ_a) and scattering (Σ_s) cross sections as shown in equation 2.5. X-ray attenuation coefficient is also

a sum of absorption and scattering. The following discussion will be in terms of neutron imaging, but all equations are also valid for X-ray imaging with slight modification.

$$\Sigma_T = \Sigma_a + \Sigma_s \qquad 2.5$$

The amount of attenuation is characterized by the Lambert-Beer's law, and it is the most fundamental equation for analysis with imaging. The number of radiation particles (X-ray or neutron) or the beam intensity decreases exponentially while traveling through an object along the incident direction. Each radiation particle is removed individually from the incident beam by an interaction (absorption or scattering) (Buzug 2008).

A homogenous material is assumed to have a single total macroscopic cross section Σ_T. The monochromatic beam intensity is proportional to the number of radiation particle after passing a distance of Δx is illustrated in Figure 2.1, and it is determined by equation 2.6.

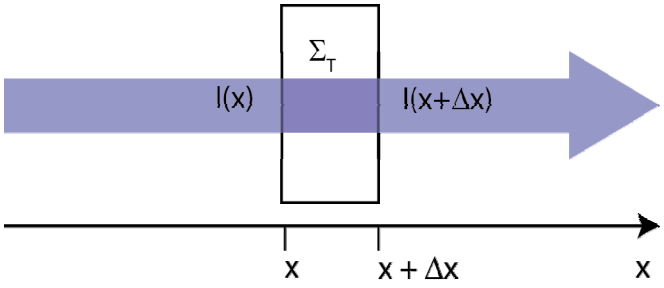


Figure 2.1: Mathematical model of monochromatic neutron attenuation where the neutrons are running through an object of thickness Δx with a constant total macroscopic cross section, Σ_T

$$I(x+\Delta x) = I(x) - \Sigma_T(x) I(x) \Delta x \qquad 2.6$$

By simple reordering of equation 2.6, equation 2.7 is obtained.

$$\frac{I(x+\Delta x) - I(x)}{\Delta x} = -\Sigma_T(x) I(x) \qquad 2.7$$

By taking the limit, it leads to the differential equation as shown in equation 2.8.

$$\lim_{\Delta x \to 0} \frac{I(x+\Delta x) - I(x)}{\Delta x} = \frac{dI}{dx} = -\Sigma_T(x) I(x) \qquad 2.8$$

Since we assumed that the medium is homogenous, we can say that the medium has a single attenuation coefficient $\Sigma_T(x) \equiv \Sigma_T$ along the entire length of penetration. This leads to an ordinary linear and homogenous, first-order differential equation with constant coefficients. The solution is obtained by separation of variables as shown in equation 2.9.

$$\frac{1}{I(x)}dI = -\Sigma_T dx \qquad 2.9$$

By taking integral on both sides equations 2.10 and 2.11 are obtained.

$$\int \frac{1}{I(x)}dI = -\Sigma_T \int dx \qquad 2.10$$

$$\ln|I| = -\Sigma_T x + C \qquad 2.11$$

Due to the physical fact than intensity is positive, the absolute sign goes away, and the equation 2.12 is obtained.

$$I(x) = e^{-\Sigma_T x + C} \qquad 2.12$$

With the initial condition of $I(0) = I_0$, the special solution of the equation becomes as equation 2.13, and it is also known as Lambert-Beer's law of attenuation.

$$I(x) = I_0 e^{-\Sigma_T x} \qquad 2.13$$

In reality, the macroscopic cross-section is energy, material density, and material atomic composition dependent as shown in equation 2.14.

$$\Sigma_T = \Sigma_T(\rho, Z, E) \qquad 2.14$$

When the equation is integrated for a narrow beam of monoenergetic neutrons with energy E_0 and intensity I_0 passes through a homogenous attenuator of thickness x can be expressed as equation 2.15 where Σ_T is the total macroscopic cross section, ρ is the density of the attenuating material, and Z is the atomic number. In case of neutron, the total macroscopic cross section is sensitive to different isotopes of same element as well.

$$I = I_0 e^{-\Sigma_T(\rho, Z, E_0)x} \quad 2.15$$

If the material is not homogenous or is a combination of different materials, the equation 2.16 can be obtained.

$$I = I_0 e^{-\int \Sigma_T(\rho, Z, E_0)dx} \quad 2.16$$

In most neutron imaging facilities, the beam is polychromatic. When a polychromatic beam passes through a sample with a line *l* characterized by various total macroscopic cross sections, the intensity of the exit beam may be expressed as equation 2.17.

$$I = \int_{E_{\min}}^{E_{\max}} I_0(E) e^{-\int_l \Sigma_T(\rho, Z, E_0)dl} dE \quad 2.17$$

During tomography reconstruction, monochromatic beam is generally assumed. Thus, we are finding an average total macroscopic cross section or attenuation coefficient over the wavelengths present in polychromatic beam. The effective energy is defined as the monochromatic energy at which a given material will exhibit the same attenuation coefficient as is measured by the scanner. Therefore, the attenuation value of the voxel is only an approximation and caution is required.

2.5 Radiography

An example layout of neutron imaging facility is illustrated in Figure 2.2. Four major components of neutron imaging include a neutron source, an aperture, an object and a detector. Details of each component can be slightly

different for different facilities. Neutron imaging facility of NIST will be used as an example here. At NIST, neutrons are generated from a 20 MW fission reactor. The neutrons are moderated to thermal neutrons in heavy water resulting in a neutron energy spectrum described by a Maxwell-Boltzmann distribution with a characteristic temperature of about 37 °C which corresponds to a neutron kinetic energy of about 25 meV. At this neutron energy range, the neutrons have a reasonable interaction probability for hydrogenous material, high penetration through metals, and most neutron imaging detectors have at least 20% thermal neutron detection efficiency. The moderated neutrons are ballistically transported to an aperture with diameter D (D = 10 mm at NIST) that defines the beam collimation. The aperture diameter can often be changed to different size for spatial and temporal resolution required for different applications. The sample is placed at a distance L from the aperture (L = 6 m at NIST), and the detector is placed directly behind the sample. To reduce scattering in air, an evacuated flight tube is placed between the sample and the aperture. Picture of the setup at NIST is shown in Figure 2.3.

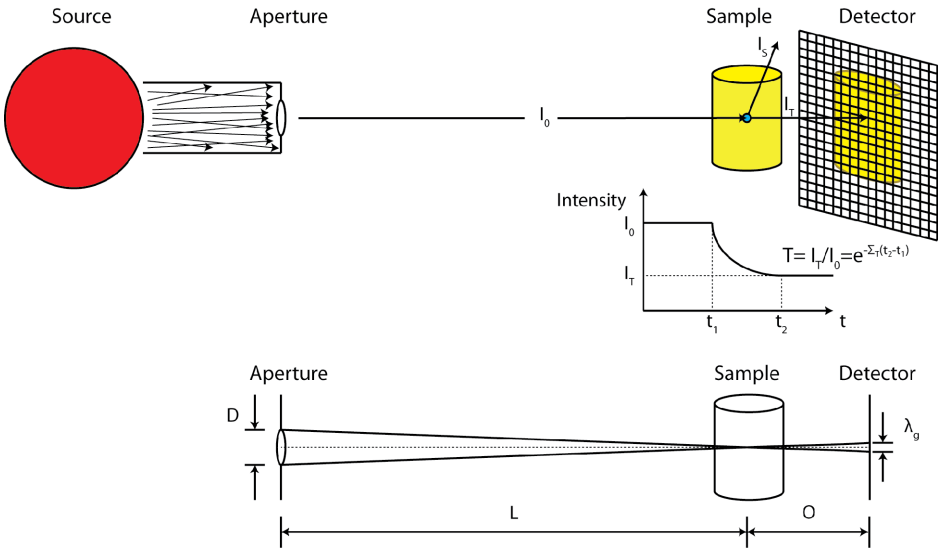


Figure 2.2: Typical neutron imaging setup; neutron interaction mechanism with matter and the effect of L/D on image resolution

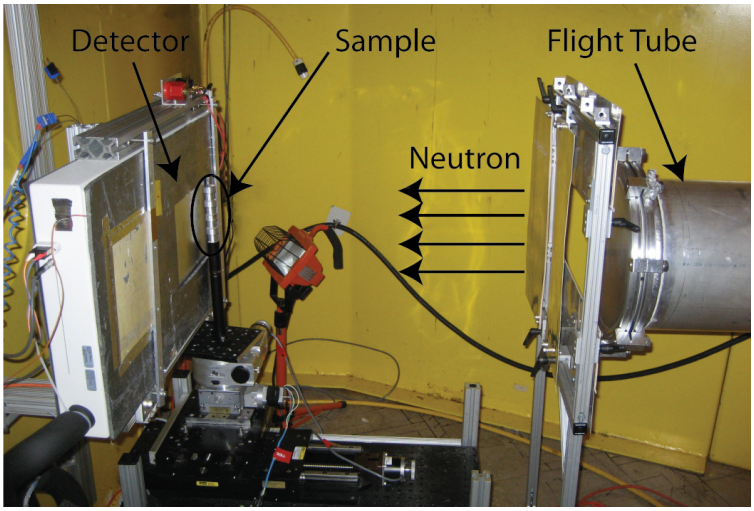


Figure 2.3: Neutron imaging setup at NIST

The spatial resolution of a neutron imaging system is affected by the geometry of the beam line and the detector resolution. Assuming a linear shift invariant system, the two components can be convolved together to estimate and model the resolution of the system. In theory, the geometry of the beam line is the fundamental limit to the resolution, while in practice the detector resolution has the larger contribution. The geometry of the beam is represented by the collimation ratio *L/D* which can be found by dividing *L* by *D*. For a sample at a distance *O* from the detector, the geometric unsharpness λ_g at full width half maximum is given by equation 2.18.

$$\lambda_g = O/(L/D) \tag{2.18}$$

2.6 Tomography

Tomography experiment can be performed by taking several radiographs at different angular orientations of the sample for at least 180° full rotation. CT scans of human or biological samples are often performed by rotating the source and detector around the object due to the size and movement of living objects. For many other applications, the source and detector is fixed while the sample rotates on a rotation stage. At neutron or synchrotron facilities, the source is fixed and sample rotates for tomography experiments.

2.7 Reconstruction

A radiograph can only show the information through the thickness of the sample. In order to obtain the information of the volume, one can perform a tomography experiment. Computed Tomography (CT) can be taken by obtaining several radiographs at different angular orientations. The data can be combined to produce reconstructed slices along the height of the specimen. The data can be reconstructed by using filtered back projection (FBP) or iterative reconstruction algorithms.

2.7.1 Filtered Backprojection

Filtered backprojection (FBP) method is an approximate method to reconstruct tomography slices. This summary is written based on several references (Buzug 2008; Gonzalez and Woods 2008; Kak and Slaney 2001). As the name indicates, the algorithm is composed of the filtering process and the backprojection process.

Figure 2.4 shows the projection process and the coordinate systems used for the following discussion. A straight line in Cartesian coordinates can be described either by its slope intercept form, $y = ax + b$, or by its normal representation as shown in equation 2.19

$$x\cos\theta + y\sin\theta = t \qquad 2.19$$

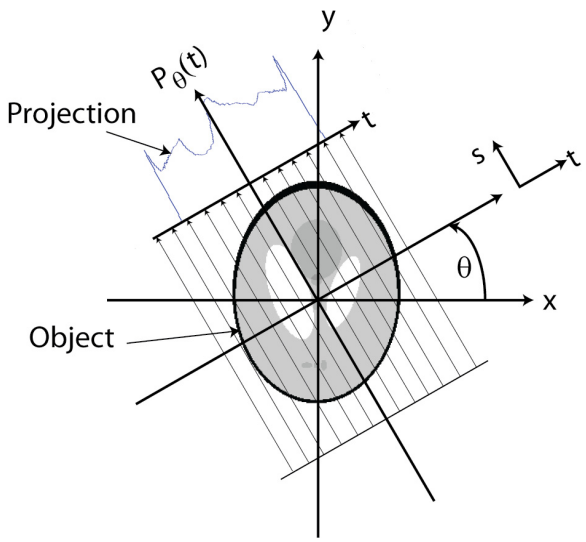


Figure 2.4: Projection process and coordinate system

The projection of a parallel-ray beam can be modeled by a set of such lines. An arbitrary point in the projection signal is given by the raysum along the line $x\cos\theta + y\sin\theta = t$ as shown in equation 2.20. θ is the given angle for the projection, and t is the given ray for the arbitrary point chosen.

$$P_\theta(t) = \int_{-\infty}^{\infty}\int_{-\infty}^{\infty} f(x,y)\delta(x\cos\theta + y\sin\theta - t)dxdy \qquad 2.20$$

δ is an impulse function which is zero unless the argument of δ is zero. This means the integral is computed only along the line $x\cos\theta + y\sin\theta = t$. This is also called the Radon transform.

The backprojection process will be explained first, and it will show the need for a filtering process. It is difficult to tell whether the beam passed through

is a single material or multiple of materials by just looking at the projection data. The backprojection process is to project the 1-D signal back across the direction from which the beam came. The process of back projecting a 1-D signal across a 2-D area sometimes is referred to as smearing the projection back across the area. An example of projection and backprojection of a circular cross section is shown in Figure 2.5.

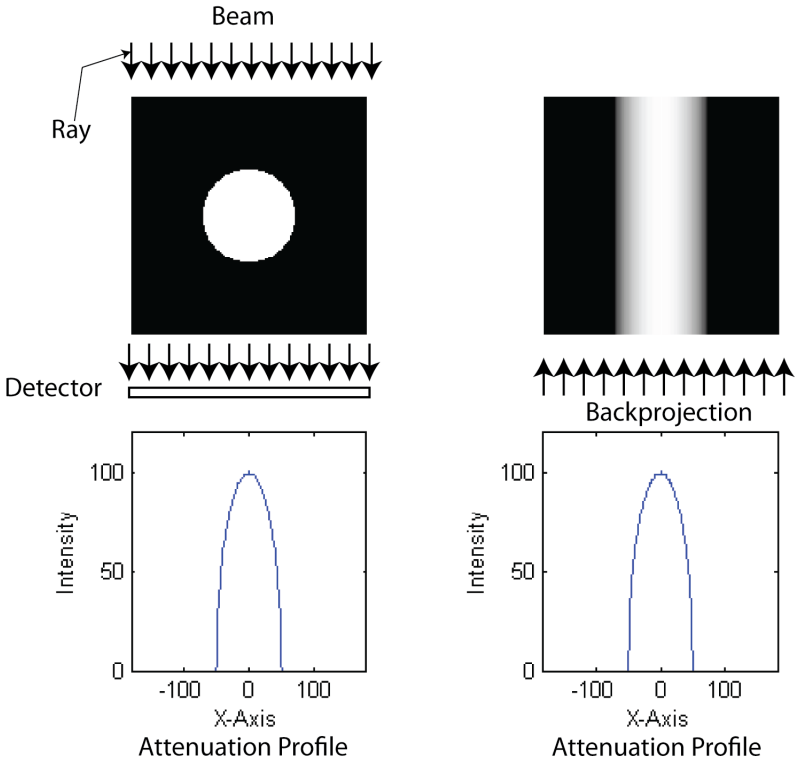


Figure 2.5: Projection and backprojection of circular cross section

When backprojections at different angles are summed together, the object of interest is detected whose amplitude is the summation of cross sectioned amplitudes of different backprojections. After the summation, the image will be scaled for display. The reconstructed image is a good approximation of the actual object, but the image is blurred by a “halo” effect as shown in Figure 2.6.

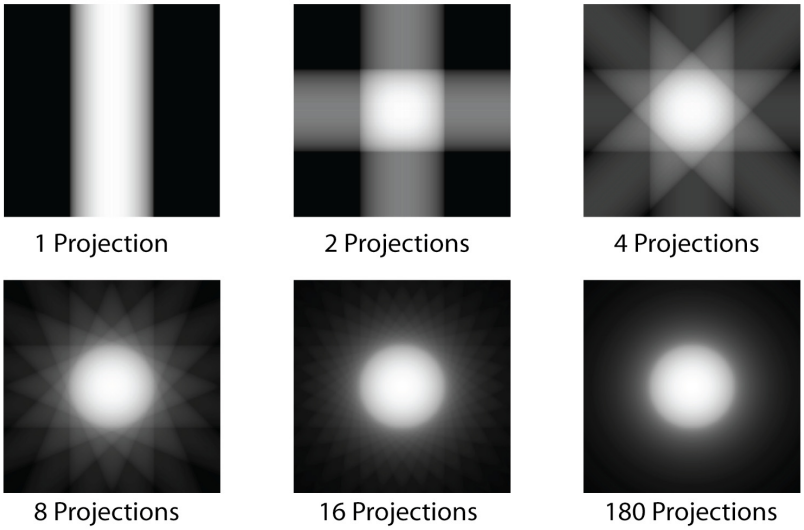


Figure 2.6: Simple backprojection of circular cross section with different number of projections

In order to solve the blurring problem with simple backprojection, Fourier slice theorem is used. The Fourier slice theorem states that 1-D Fourier transforms of a projection is equal to a slice of the 2-D Fourier transform of the

original object as shown in Figure 2.7. The Fourier slice theorem can be used to show the equality in equation 2.21. Instead of performing backprojection in the spatial domain, the backprojection can be summed in the Fourier domain with some manipulation.

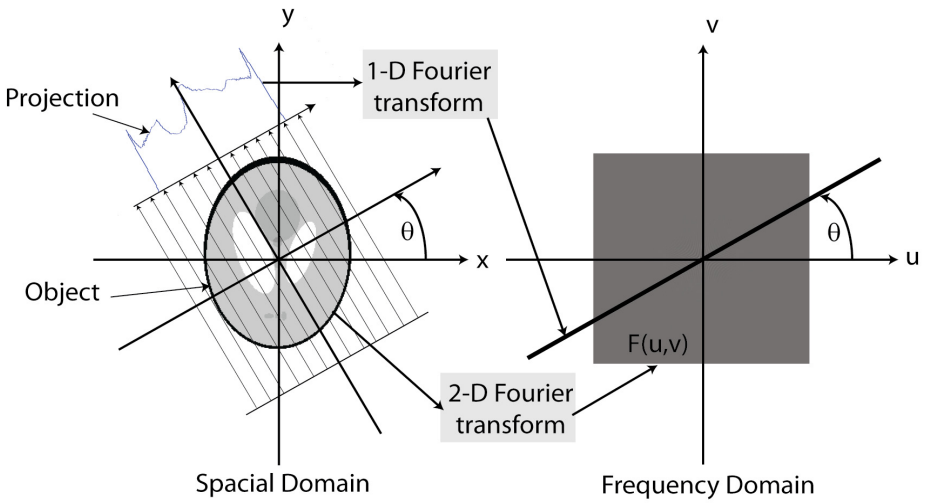


Figure 2.7: Fourier slice theorem

$$F(\omega\cos\theta, \omega\sin\theta) = F(\omega,\theta) \qquad 2.21$$

The inverse Fourier transform of *F* (*u*, *v*) is shown in equation 2.22, where $\theta = \tan^{-1}\left(\frac{v}{u}\right)$ and $\omega = \sqrt{u^2+v^2}$. The *f*(*x*, *y*) refers to the image of the reconstructed slice.

$$f(x,y)=\int_{-\infty}^{\infty}\int_{-\infty}^{\infty}F(u,v)e^{j2\pi(ux+vy)}\,du\,dv \qquad 2.22$$

By using the equalities in equation 2.23, the equation 2.22 can be modified to equation 2.24.

$$\begin{vmatrix}\frac{\partial u}{\partial \omega} & \frac{\partial u}{\partial \theta}\\ \frac{\partial v}{\partial \omega} & \frac{\partial v}{\partial \theta}\end{vmatrix}=\begin{vmatrix}\cos\theta & -\omega\sin\theta\\ \sin\theta & \omega\cos\theta\end{vmatrix}=\omega\cos^2\theta+\omega\sin^2\theta=\omega \qquad 2.23$$

$$f(x,y)=\int_{0}^{2\pi}\int_{0}^{\infty}F(\omega\cos\theta,\omega\sin\theta)e^{j2\pi(x\cos\theta+y\sin\theta)}\,\omega\,d\omega\,d\theta \qquad 2.24$$

By using the equation 2.21 derived from Fourier Slice Theorem, equation 2.25 is derived.

$$f(x,y)=\int_{0}^{2\pi}\int_{0}^{\infty}F(\omega,\theta)e^{j2\pi(x\cos\theta+y\sin\theta)}\,\omega\,d\omega\,d\theta \qquad 2.25$$

By using the fact that $F(\omega,\theta+180^\circ)=F(-\omega,\theta)$, equation 2.25 can be simplified to equation 2.26

$$f(x,y)=\int_{0}^{\pi}\int_{-\infty}^{\infty}|\omega|F(\omega,\theta)e^{j2\pi(x\cos\theta+y\sin\theta)}\,d\omega\,d\theta \qquad 2.26$$

In terms of integrating with respect to ω, the term $x\cos\theta+y\sin\theta$ is constant which is *t*. Thus, the equation 2.26 can be written as shown in equation 2.27.

$$f(x,y)=\int_{0}^{\pi}\left[\int_{-\infty}^{\infty}|\omega|F(\omega,\theta)e^{j2\pi\omega t}\,d\omega\right]_{t=x\cos\theta+y\sin\theta}d\theta \qquad 2.27$$

Equation 2.27 can be further simplified to equation 2.28 where $\hat{P}_\theta=\int_{-\infty}^{\infty}|\omega|S_\theta(\omega)e^{j2\pi\omega t}\,d\omega$ and $t=x\cos\theta+y\sin\theta$. $S_\theta(\omega)$ is the 1-D Fourier transform

of the projection at angle θ. The $|\omega|$ function is a one-dimensional ramp filter function.

$$f(x,y) = \int \hat{P}_\theta(x\cos\theta + y\sin\theta)d\theta \qquad 2.28$$

To summarize, the 1-D projection profile is first Fourier transformed and filtered in the frequency domain. Then the filtered Fourier transformed projection profile is inverse Fourier transformed to spatial domain, and subsequently backprojected in 2-D. Due to the filtering process, the halo effect is removed in the reconstructed slice. A result of FBP in comparison to Figure 2.6 is shown in Figure 2.8 where halo effect is removed.

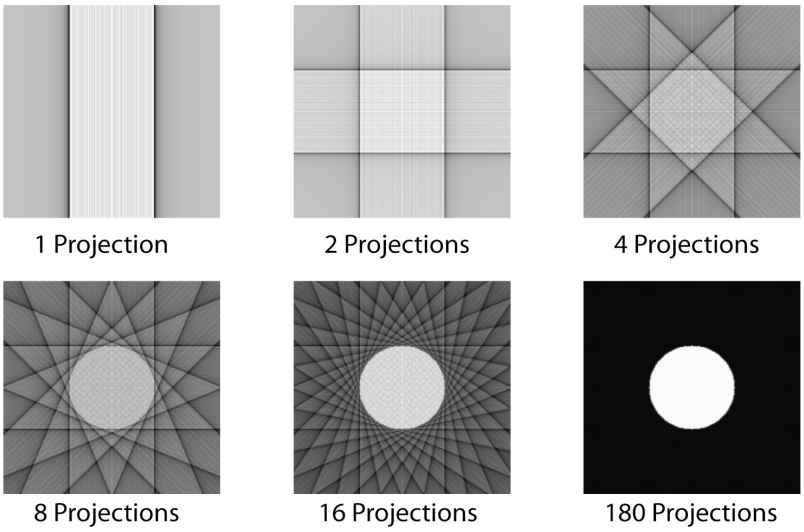


Figure 2.8: FBP of circular cross section for different number of projections

2.7.2 Iterative Reconstruction

Iterative reconstruction (ITR) method is a method solves the problem iteratively based on the linear attenuation behavior of radiation particle. This summary was written based on several references (Benson 2006; Kak and Slaney 2001). It is assumed that each ray of all projections have a linear relationship with the material interacted. When all rays of the entire projection data are combined, a linear matrix system can be set up as shown in equation 2.29.

$$Ax = b \tag{2.29}$$

In this case, *A* is the m x n matrix that governs the linear relationship between each ray and each pixel of the reconstructed slice of interest, *x* is the n x 1 matrix of each pixel value (attenuation coefficient) of the reconstructed slice, and *b* is the m x 1 matrix of summed attenuation of each ray. The total number of rays is m, and the total number of pixel in the reconstructed slice is n. A_{ij} means the coefficient of the i^{th} ray against the j^{th} pixel in the image plane.

The first step of iterative reconstruction is to create a system matrix which describes the relationship between each ray and the reconstructed slice image pixels. The accuracy of the system matrix governs the quality of image reconstructed. There are a few different type of system model such as line intersection model, linear interpolation model, and volumetric model. The process of creating a binary system model is shown in Figure 2.9. The pixels that the ray

crosses get the values of 1 and other pixels are 0. This is done for every ray of the entire projection and all the coefficients are added.

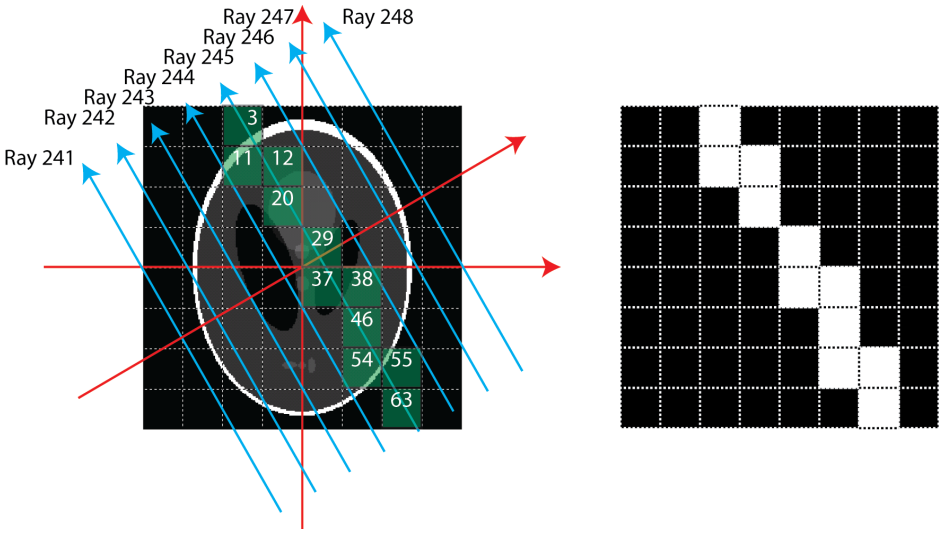


Figure 2.9: Binary system model

A bilinear interpolation model is also developed. It is a more accurate system model than binary system model. A point in a ray, (x, y), is interpolated between the pixel center of the nearest 4 pixels ((x_i, y_i), (x_{i+1}, y_i), (x_i, y_{i+1}), and (x_{i+1}, y_{i+1})) as shown in Figure 2.10 where $0 \leq u, v \leq 1$. Each 4 pixels add up respective coefficients shown in Table 2.2 for each equidistant point in every ray to create a system matrix.

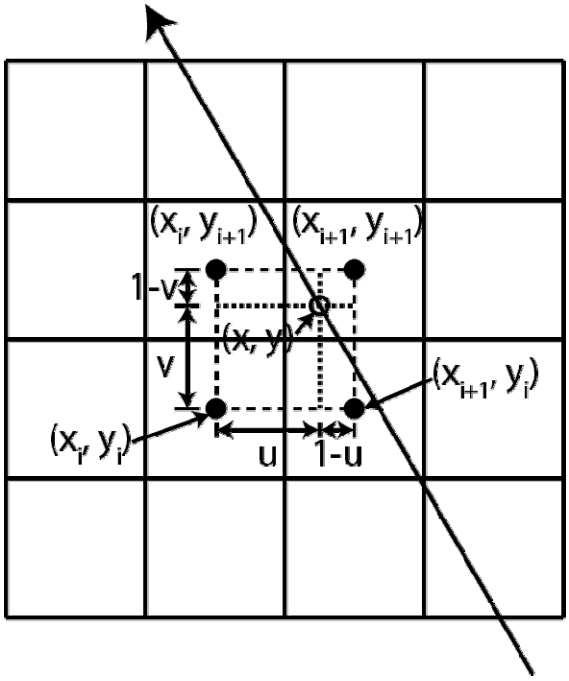


Figure 2.10: Bilinear interpolation model

Table 2.2: The four points representing pixel centers and the associated interpolation coefficients used in bilinear interpolation

Pixel Center	Interpolation Coefficient
(x_i, y_i)	$(1-u)\cdot(1-v)$
(x_{i+1}, y_i)	$u\cdot(1-v)$
(x_i, y_{i+1})	$(1-u)\cdot v$
(x_{i+1}, y_{i+1})	$u\cdot v$

The matrix A is usually not a square matrix. As a result, the system is generally over determined or underdetermined. Additionally, there is always some noise included in the projection data, and it prevents the linear system from having a unique solution. Thus, an iterative approach using some convergence properties needs to be considered. As a result, the linear system in equation 2.30 is modified to equation 2.31.

$$Ax \approx b \tag{2.30}$$

$$x \approx \min \left\| Ax - b \right\|_2 \tag{2.31}$$

Equation 2.31 becomes a least square problem as shown in equation 2.32.

$$A^T Ax = A^T b \tag{2.32}$$

The exact solution of the normal equation is the solution for the least square problem (Saad 2003).

$$AA^T y = b \tag{2.33}$$

Alternative normal equation is also often used where $x = A^T y$ as shown in 2.33. It is the normal equation associated with the equation 2.34.

$$\min \left\| x - A^T y \right\| \tag{2.34}$$

Once a system matrix is created, one should find a suitable iterative algorithm to solve the linear system. The iterative algorithms can be divided to algebraic and statistical algorithms. The algebraic algorithms include Algebraic Reconstruction Technique (ART), Simultaneous Algebraic Reconstruction

Technique (SART), and Simultaneous Iterative Reconstruction Technique (SIRT) techniques. Statistical algorithms include Expectation Maximization (EM) and Weighted Least Squares (FWLS).

2.7.3. Reconstruction Results

A filtered backprojection code for parallel beam was written as part of my independent study with Dr. Jens Gregor of EECS department. High resolution neutron tomography data of partially saturated sand specimen was reconstructed by using the code I developed and commercial software Octopus 8.4. As shown in Figure 2.11, the profile A-A was almost identical for both cases. The slight difference between the two data is thought to be due to applying different smoothing filters during the reconstruction process.

An iterative reconstruction code is also developed. A simpler binary code was initially developed, but a more realistic bi-linear interpolation code was developed recently. ART was used as the iteration method. The system matrix developed can take as high as several GB of memory for large data sets. Sparse storage scheme was used to reduce the memory requirement. A result of currently developed code of binary model is shown with the Shepp-Logan phantom in Figure 2.12. The Shepp-Logan phantom is also reconstructed with iterative reconstruction by using interpolation model in Figure 2.13. It shows that the current iterative reconstruction result shows higher contrast closer to the original result, but is somewhat noisier compared to that of filtered

backprojection. Additional processing is expected to improve iterative reconstruction technique, and it is left as a future work. Filtered backprojection reconstruction and iterative reconstruction is performed on a real neutron imaging data set as shown in Figure 2.14. Several small holes are made in an aluminum cylindrical stock and the holes are filled with water. The data was obtained at NIST with amorphous silicon detector with 127 μm pixel size. The projection image has 101 pixels horizontally, and the number of projection is 361. The current iterative reconstruction code is limited by the amount of memory available on the computer, and only a small data set is used for iterative reconstruction. Additional optimization such as parallelization will be explored in the future.

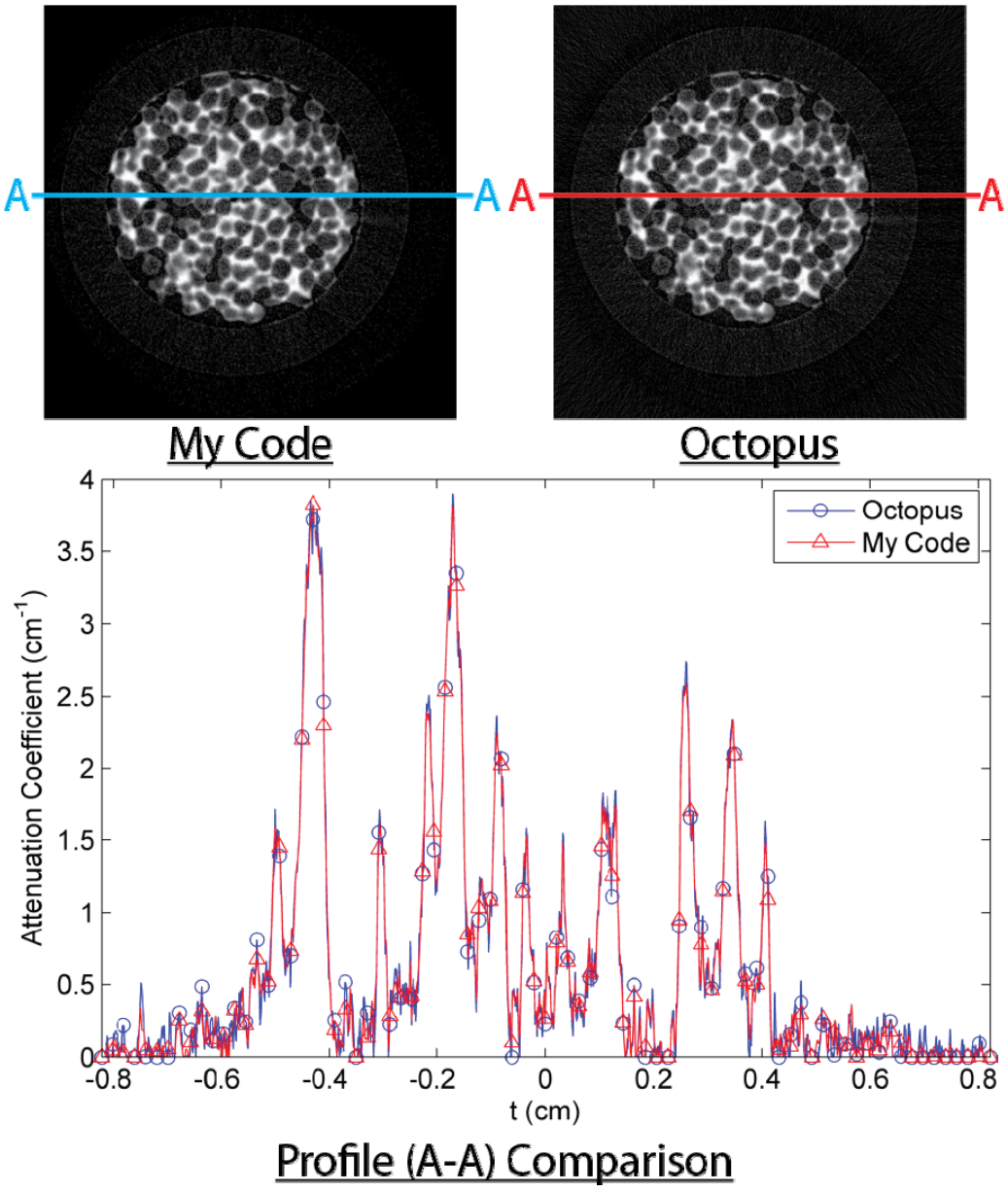


Figure 2.11: FBP result of high resolution neutron tomography data of partially saturated sand sample

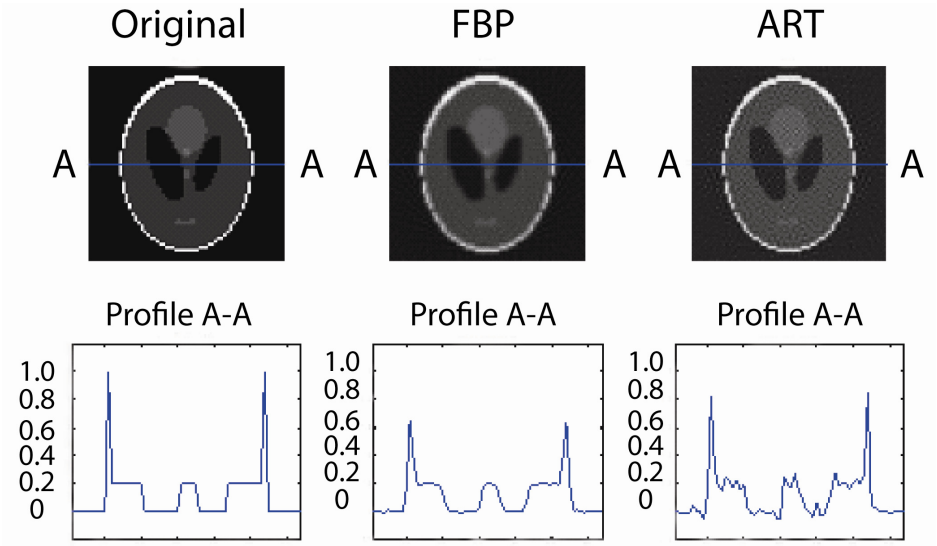


Figure 2.12: Comparison of original, filtered backprojection and iterative reconstruction (binary model with ART) result of 64 × 64 Shepp-Logan phantom

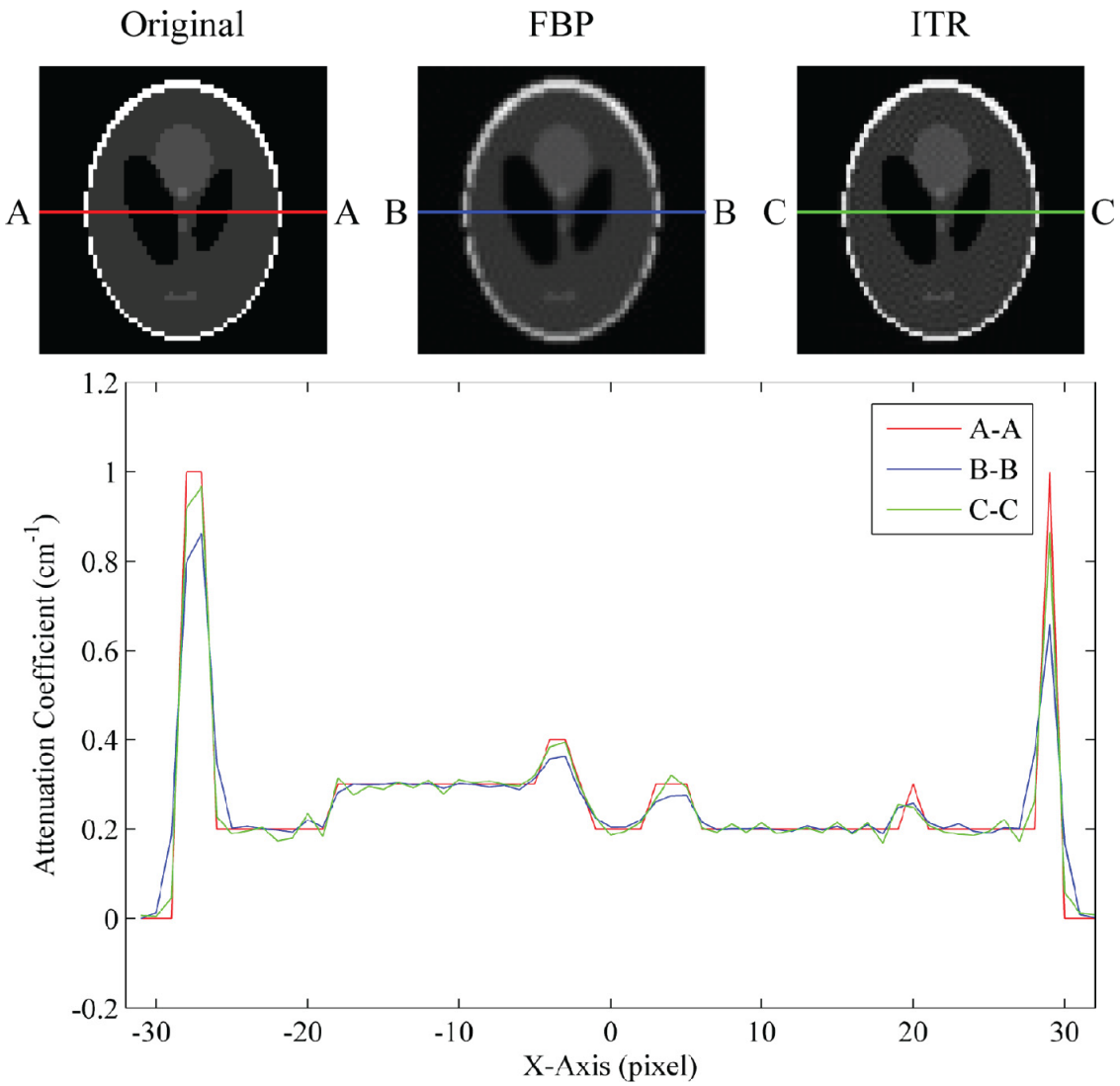


Figure 2.13: Comparison of original, filtered backprojection and iterative reconstruction (interpolation model with ART) result of 64 × 64 Shepp-Logan phantom

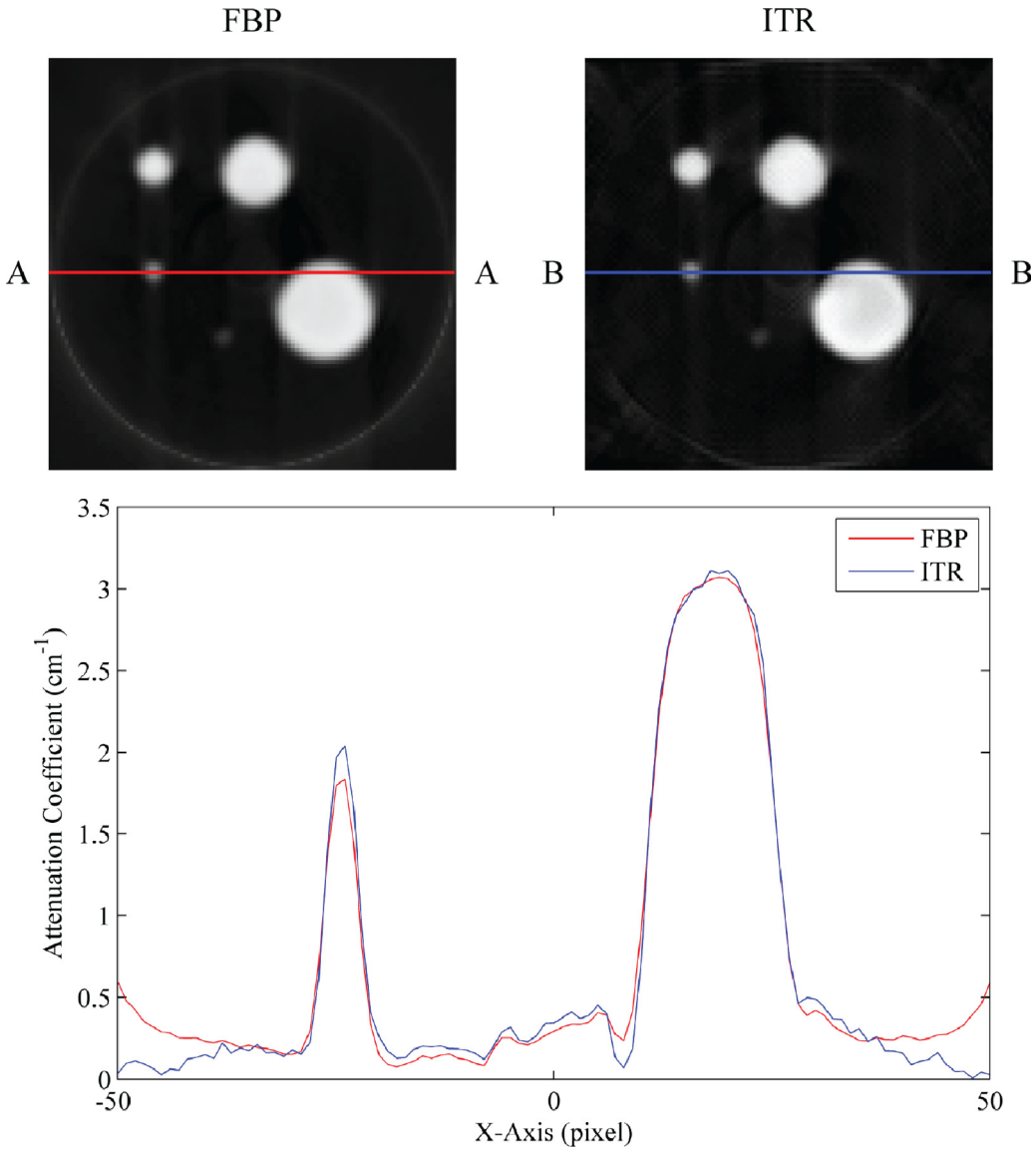


Figure 2.14: Comparison of filtered backprojection and iterative reconstruction (interpolation model) result of neutron tomography data of various holes filled with water

2.7.4 Comparison of FBP and ITR

FBP is a very fast algorithm and produces acceptable results. It is one of the most commonly used algorithms, and commercial software is available for easy implementation. Relatively large size of data sets can be reconstructed in the order of a few minutes or less with a normal personal computer. However, the algorithms are based on the line integrals which don't describe the process of X-ray attenuation accurately. Also, the noise in the projection data is not properly modeled with FBP. FBP assumes that the projection data is noise free, but noise is inherent in projection data especially for low-count projection data.

On the other hand, ITR use a more complicated system model than line integrals. It is also possible to account for scatter and other additive noise factors using the iterative algorithms which require complicated modeling process. Statistical approach can be used for low-count projection data. ITR tends to hold better with limited number of projections compared to FBP. ITR also tends to show better contrast in the image compared to FBP. However, ITR requires high memory storage space and computational powers.

2.8 Dual Modality Imaging

The motive of this work comes from different contrast mechanism of neutron and X-ray. Both X-ray and neutron are penetrating radiations, but their fundamental interaction mechanisms with materials are different. While X-ray mainly interacts with the electron cloud of an atom, neutrons mainly interact with

the nucleus of an atom as shown in Figure 2.15. As neutrons are electrically neutral unlike X-rays, they interact mainly with the nucleus of an atom.

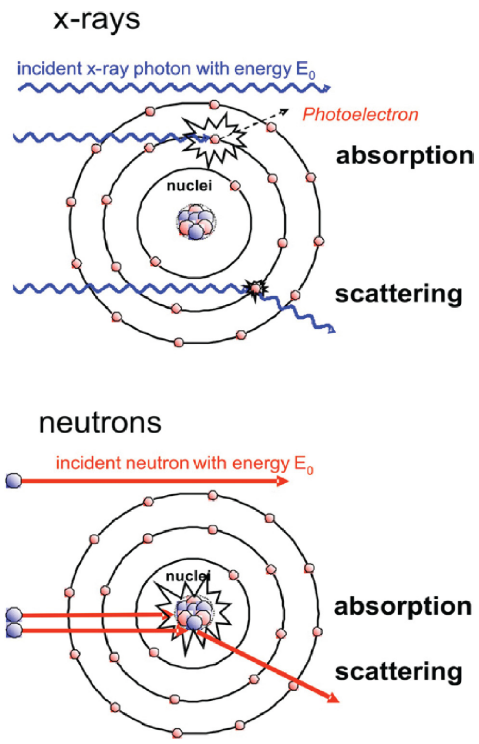


Figure 2.15: Interaction of matter with X-rays and neutrons (Strobl et al. 2009). (© IOP Publishing. Reproduced by permission of IOP Publishing. All rights reserved.)

As a result, the X-ray attenuation coefficient and neutron macroscopic cross section trends are different as shown in Figure 2.16. As the atomic number increases, the X-ray mass attenuation coefficient increases since the size of

electron clouds increases. However, there is no particular trend for neutron total macroscopic cross sections since neutron directly interacts with the nucleus. Thus, neutron provides strong contrast for some elements that are close to one another in the periodic table, and it can even distinguish between different isotopes. For example, neutron has high attenuation coefficient for light atoms such as hydrogen while X-ray hardly provides contrast. Neutrons can also penetrate through heavy metals such as steel and lead more easily compared to X-rays. Thus, we can obtain complementary contrast in the images obtained from neutron and X-ray. This is called dual-modal contrast.

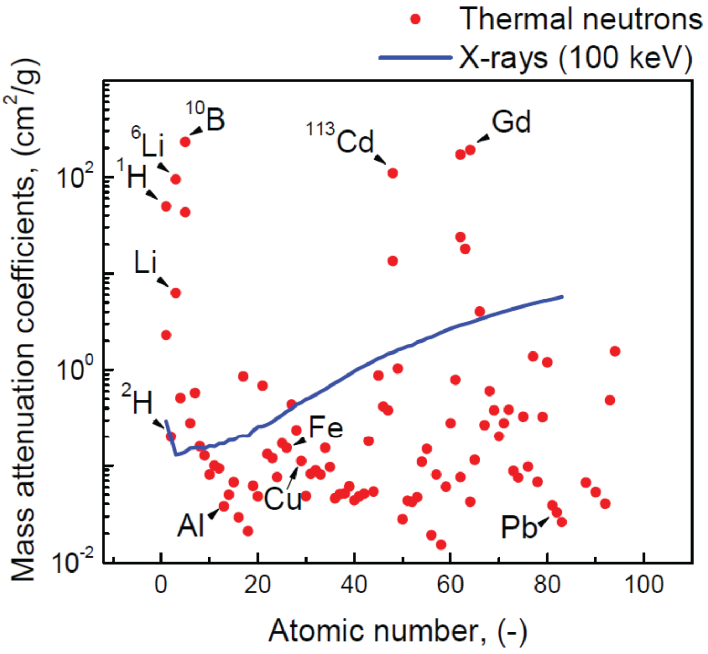


Figure 2.16: Mass attenuation coefficients for thermal neutrons and100 keV x-rays for the elements. (Reprinted with permission from Kardjilov et al. (2006). Copyright (2006), IOS Press)

Dual-modal (X-rays and neutrons) contrast can be obtained for the three phases of partially saturated sand. The attenuation coefficients of silica, air and water phases of X-ray (100 keV) and neutron (cold) are graphically compared in Figure 2.17.

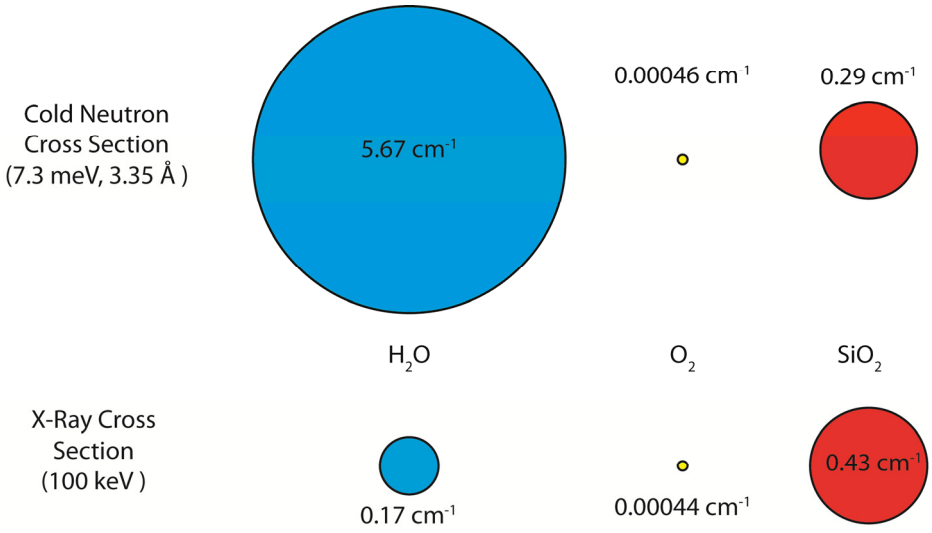


Figure 2.17: Attenuation coefficient comparison of water, air and sand phase for cold neutron and X-ray (100 keV)

However, it is not impossible to obtain good contrast between the three phases with X-ray only. The author has learned this idea far advanced in PhD work, and was not able to pursue the idea further. However, some example results are still presented here. The X-ray attenuation coefficients and penetration depth of silica, air and water are compared in Figure 2.18. The attenuation coefficient of air is very close to 0. As the energy decreases, the contrast of water improves, but the attenuation of silica increases as well. At low X-ray energy (<~40 keV), good contrast of water phase is achievable, but the penetration depth of silica is fairly low (<~1.5 cm). As a result, only a smaller volume of soil specimen may be imaged. In addition to attenuation of silica and

water, there can be attenuation of container the soil specimen is placed in. The container's material and thickness determines the attenuation of container. Material such as acrylic/Plexiglas has low attenuation for X-ray, and it can be used as a simple container or a flow chamber. For an experiment such as 1-D compression test, a rigid material is needed and acrylic is not stiff enough. Most metallic material such as steel with reasonable thickness almost cannot be used as container due to its high attenuation to X-rays. Due to the size limitation and low contrast of water, a contrast agent such as Cesium Chloride (CsCl) is often added to improve the contrast of liquid phase. Addition of such contrast often involves question of fluid interfacial property by changing contact angle depending on type and amount of contrast agent used.

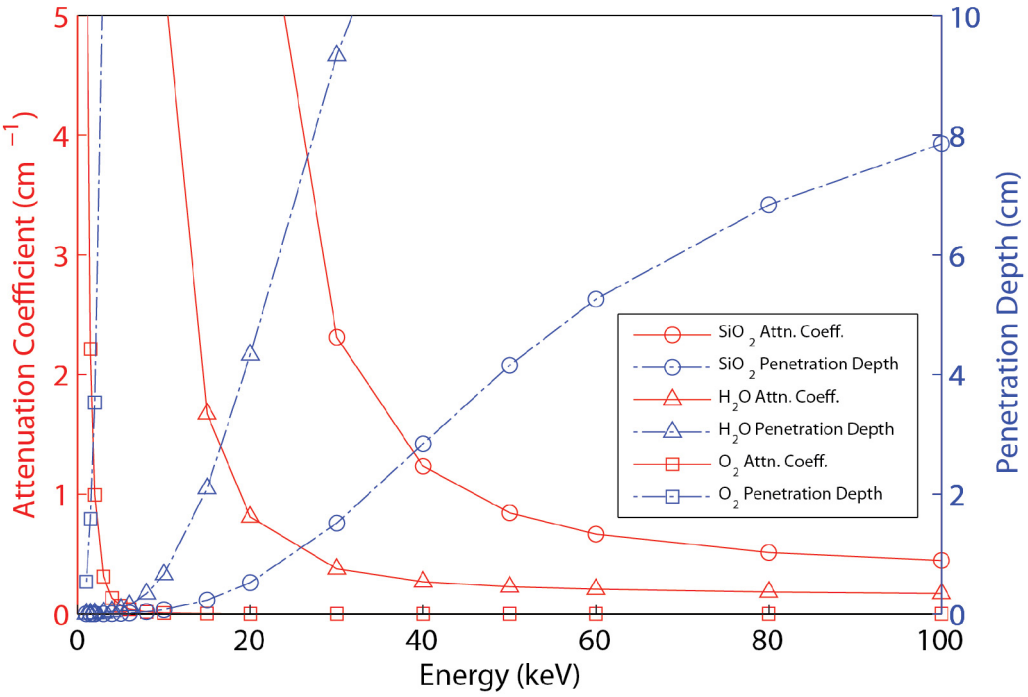


Figure 2.18: Comparisons of X-ray energy and attenuation coefficients for water and silica

An example of how water contrast is improved with X-ray image is shown in Figure 2.19. A partially saturated sand specimen is imaged with Xradia microfocus X-ray imaging system in collaboration with Xradia (Kim et al. 2012). Different optical magnification by switching lens was used to image the sand. High contrast of water is achieved at relatively low energy (~35 keV for low magnification, ~40 keV for high magnification). The high resolution segmentation results are shown is Figure 2.20. Advanced image smoothing algorithm (non-local mean) was applied.

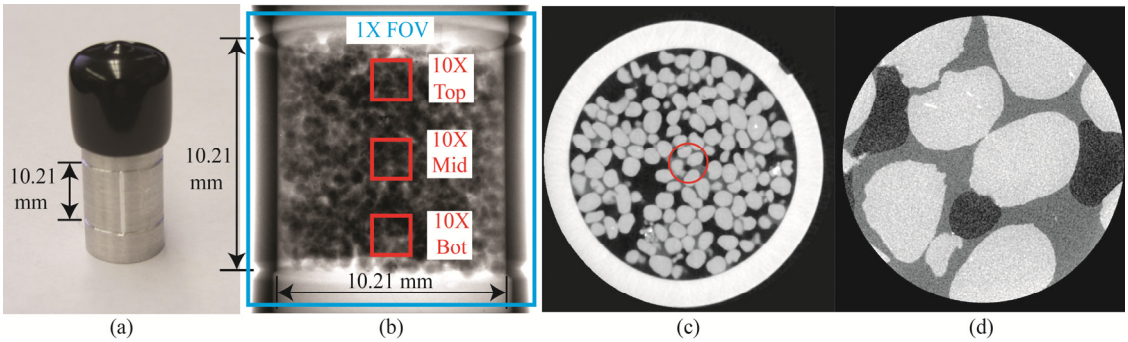


Figure 2.19: Picture of the partially saturated sand specimen (a), radiography of partially saturated sand specimen showing 1X and 10X magnification FOV size and location (b), tomography slice of partially saturated sand specimen at 1X magnification (c), and tomography slice of partially saturated sand specimen at 10X magnification (d)

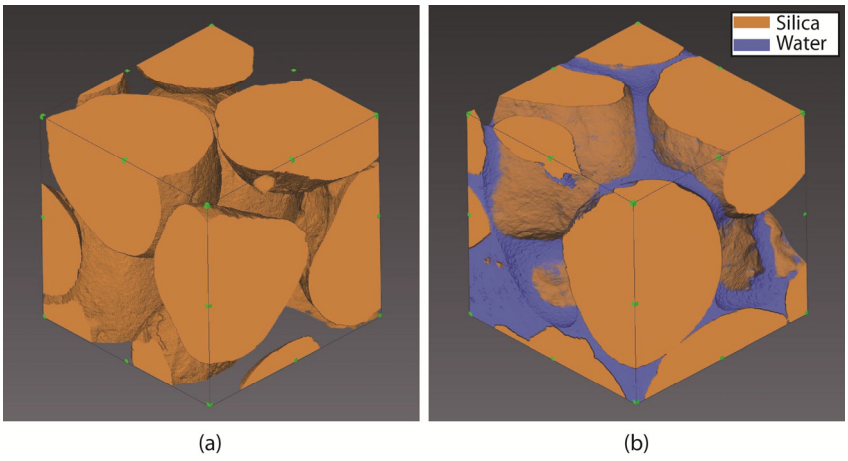


Figure 2.20: Three dimensional visualization (1mm^3) of dry (a) and partially saturated (b) sand specimen at 10X magnification

In this research, dual modality imaging approach was used to study partially saturated sand and flow through compacted sand. Possibility of thresholding water phase by using X-ray imaging modality alone is acknwoledged as shown with the imaging results of Xradia imaging results. However, the low attenuation of water to X-ray makes it relatively difficult to monitor fluid flow in radiography which is planned to be used in this research. It is also very difficult to penetrate through large soil specimen with low energy X-rays whicvh will show good enough contrast of water. Having additional information with neutron imaging combined with X-ray imaging results will also improve possibility of thresholding water phase. The dual-mopdality imaging technique provides an alternative approach to using a contrast agent to improve contrast of liquid and possibly used on samples from the environment where the addition of a contrast agent is not possible.

2.8 References

Benson, T. M. (2006). "Iterative Reconstruction of Cone-Beam Micro-CT Data," University of Tennessee, Knoxville, Knoxville.

Bushberg, J. T., Seibert, J. A., Leidholdt, J. E. M., Boone, J. M., and Goldschmidt, J. E. J. (2003). "The Essential Physics of Medical Imaging." *Medical Physics*, 30(7), 1936-1936.

Buzug, T. M. (2008). *Computed Tomogrpahy From Photon Statistics to Modern Cone-Beam CT*, Springer, Verlag Berlin Heidelberg.

Gonzalez, R. C., and Woods, R. E. (2008). *Digital Image Processing*, Pearson Prentice Hall, Upper Saddle River, NJ.

Herwig, K. W. (2009). "Introduction to the Neutron." Neutron Imaging and Applications, I. S. Anderson, McGreevy, R.L., Bilheux, H.Z., ed., Springer Science+Business Media, LLC New York, NY.

Kak, A. C., and Slaney, M. (2001). *Principles of Computerized Tomographic Imaging*, Society for Industrial and Applied Mathematics, Philadelphia, PA.

Kardjilov, N., Fiori, F., Giunta, G., Hilger, A., Rustichelli, F., Strobl, M., Banhart, J., and Triolo, R. (2006). "Neutron tomography for archaeological investigations." *Journal of Neutron Research*, 14(1), 29-36.

Kim, F. H., Penumadu, D., Gu, A., Yun, S., and Gelb, J. (2012). "High Resolution Imaging of Porous Geomaterials and Geological Cores with Micro Computed X-Ray Tomography." 2012 Society of Core Analysts Symposium, Aberdeen, Scotland.

Knoll, G. F. (2000). *Radiation Detection and Measurement*, John Wiley & Sons.

Saad, Y. (2003). *Iterative methods for sparse linear systems*, SIAM.

Strobl, M., Manke, I., Kardjilov, N., Hilger, A., Dawson, M., and Banhart, J. (2009). "Advances in neutron radiography and tomography." *Journal of Physics D: Applied Physics*, 42(24), 1-21.

CHAPTER 3. NEUTRON IMAGING OF PARTIALLY SATURATED SAND

This chapter is revised based on a paper published by Felix Kim, Dayakar Penumadu and Daniel Hussey:

Kim, F. H., Penumadu, D. and Hussey, D. S. (2012). Water Distribution Variation in Partially Saturated Granular Materials Using Neutron Imaging. Journal of Geotechnical and Geoenvironmental Engineering, American Society of Civil Engineers (ASCE), 138(2), 147-154.

My primary contributions to the paper included: (i) understanding of thermal neutron imaging technique, (ii) gathering and reviewing literature, (iii) performing neutron imaging experiment at NIST, (iv) processing, analyzing, and interpretation of the experimental data, (v) most of the writing.

3.1 Abstract

The use of neutron imaging is demonstrated for visualizing and quantifying water distribution in partially saturated granular porous media. Due to the unique difference in the total neutron cross sections of water, sand and air, a significant contrast for the three phases is observed in a neutron transmission image, and a quantitative analysis provides detailed information on the arrangement and distribution of particles, voids, and water. The experiments in this study are performed at the Neutron Imaging Facility (NIF) at the National Institute of Standard and Technology (NIST). An amorphous silicon flat panel detector was used in this research with a spatial resolution of approximately 250 μm (127 μm/pixel). The effect of particle morphology on water distribution in compacted granular columns is investigated by using round and angular silica sand. Silica sand specimens with different bulk gravimetric water contents (0%, 6%, 9% and 12%) are studied for evaluating the water phase distribution spatially for compacted sand specimens in an aluminum cylinder.

3.2 Introduction

The physics and mechanics of wet granular materials are important to understand in many real world applications since it is inevitable to have water in a granular material assembly. The mechanical behavior of partially saturated sand is largely affected by the nature of pore air, pore water, and wetting

interfaces with sand particle contacts. It is well known that due to negative capillary pore pressure, an assemblage of partially saturated sand particles can gain additional shear strength and stiffness, or modify the flow properties and mixing behavior of granular materials. However, the basic physics and mechanics of wet granular materials are only qualitatively understood at the macro scale and remain to be explored at the particle scale. The geometry and the distribution of water in a granular system are very complex and vary with water content. Water in a granular system is not uniformly distributed due to varying contact surfaces and complex inter-particle void spaces. Water typically concentrates at the contact surfaces of the sand particles, creating stability of the granular system (Schiffer 2005). The mechanical properties of a partially saturated granular system are expected to be strongly dependent on the spatial distribution of the local water content at the particle scale.

X-ray tomography has been used routinely to study the physics of granular materials (Alshibli et al. 2000; Jaeger et al. 1996; Oda et al. 2004). X-ray imaging has been used effectively to study dry granular materials due to its high attenuation on silica. One of the earliest applications of X-ray tomography on rock and soil was performed by Wellington and Vinegar in studying petrophysical and fluid flow analysis (Wellington and Vinegar 1987). Desrues et al. have studied shear bands of soil samples with X-ray tomography (Desrues et al. 1996). The local void ratio in porous media systems has been measured with X-

ray microtomography (Al-Raoush and Alshibli 2006). The distribution of liquid in a glass bead system using an aqueous zinc iodide solution as a wetting liquid was measured with X-ray microtomography (Scheel et al. 2008). It was demonstrated that the mechanical properties of a granular pile are affected by the local liquid organization in the granular system. Some researchers have visualized fluid phase in partially saturated soils by using dual energy method with a contrast agent (CsCl) to separate the water phase from the air phase with a resolution in the order of 10 μm/pixel (Al-Raoush and Willson 2005; Han et al. 2006; Lu et al. 2010). In general, the contrast agents are typical salts and could change the wetting behavior of water due to having a different contact angle. For example, Schnaar and Brusseau estimated 15 – 20° decrease of contact angle for ionic strength of 0.36 M CsCl solution based on the result of Barranco et al. even though they determined that the presence of CsCl is not expected to significantly influence the phase-distribution behavior for the given condition (Barranco et al. 1997; Schnaar and Brusseau 2005). In many cases, however, it is difficult to estimate the effect of the change of contact angle on the water retention behavior especially on a porous media. Using the pure water without any contrast agent would eliminate any concern with the change of contact angle. In addition, contrast agents are not an option for studying samples from the environment.

Neutron imaging, a complementary method to the X-ray imaging technique for studying materials, provides unique contrast to locate small

amounts of hydrogenous matter. Similar to X-rays, neutrons have the capability of penetrating materials for non-destructive evaluation. However, neutrons have different attenuation values (cross sections) from those of X-rays for all elements, since the neutron primarily interacts with the nucleus whereas X-rays primarily interact with the electron cloud. In particular, neutrons have relatively large cross sections for light elements such as hydrogen and relatively low cross sections for many metals such as aluminum and steel. These characteristics make neutrons ideal for imaging hydrogenous materials in a metallic matrix. In addition, in the past 10 years, the achievable spatial and temporal resolutions of neutron radiography have significantly improved primarily due to advances in digital detector technology. In particular, image spatial resolution of about 200 μm with temporal resolution less than 1 s is routine at most facilities and detectors with spatial resolution less than 20 μm are also widely available. This sensitivity to hydrogen and good spatial resolution have been used extensively to study water transport in proton exchange membrane fuel cells (Arif et al. 2008; Trabold et al. 2009) as well as in research areas including biology, material science, plant physiology, and homeland security (Lanza 2008; Nakanishi 2008; Penumadu 2008; Watkin et al. 2008).

In studying water transport in sand, there are three phases to consider, sand (SiO_2), air (N_2 and O_2) and water (H_2O). The total scattering cross sections for thermal neutrons (25 meV) and 40 keV X-rays of H_2O, O_2, and SiO_2 are

compared in Figure 3.1, and it is seen that the total neutron cross section of H_2O is about 16 times larger than that of SiO_2, while for 40 keV X-rays, SiO_2 has a cross section 6 times that of H_2O. One of the earliest applications of neutron imaging on soil and rock was performed by Lewis and Krinitzsky with 2-D radiography (Lewis and Krinitzsky 1976). The factor of 16 difference in neutron cross sections between water and silica phases means that there is excellent contrast for water in porous media which has been exploited to study acid etching of limestone and sandstone in the early 90s (Jasti and Fogler 1992). The instability of a wetting front breaking up into finger-like flow path in porous media using Ottawa sand was visualized with neutron radiography and tomography (Tullis et al. 1994). A feasibility study to measure the porosity of crystalline rock has been performed (Pleinert and Degueldre 1995). A tomography study of wet sand was performed, though at a low resolution on the order of 1 mm (Lopes et al. 1999). More recently, neutron imaging was also used for the measurement of the water diffusion in brick (Milczarek et al. 2005), two phase flow in porous concrete using a Hassler cell to simulate petroleum recovery (de Beer and Middleton 2006), and water sorption and dehydration with and without salt in three different limestones from the United States (Hassanein et al. 2006).

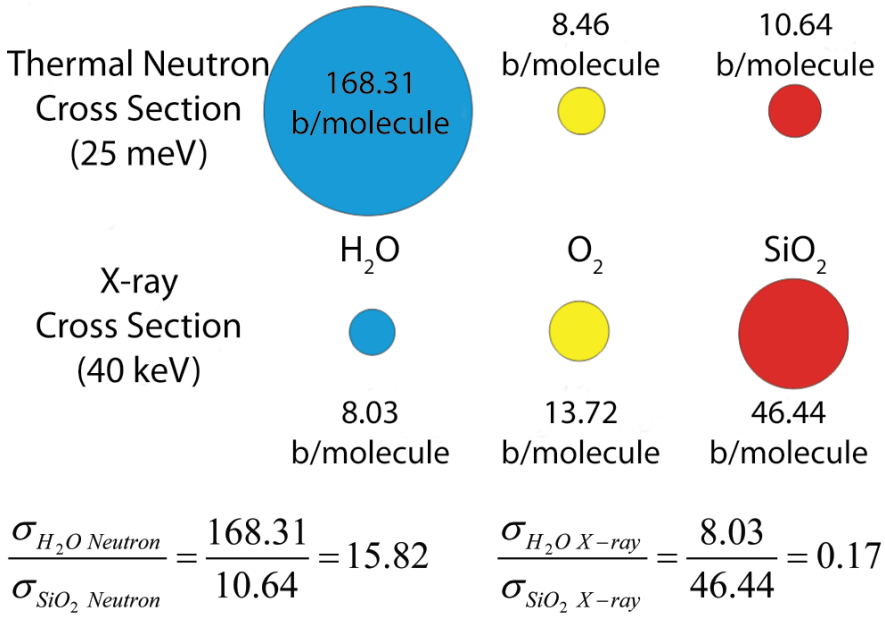


Figure 3.1: Cross section comparison of H_2O, O_2 and SiO_2 for neutrons and X-rays (1 b = 10^{-24} cm^2)

In this paper, the water distribution of partially saturated compacted specimens of naturally occurring Ottawa sand and Q-ROK® sand was obtained from both two dimensional (2-D) neutron radiography and three dimensional (3-D) neutron tomography under static conditions. While much of the earlier research using neutron imaging has focused on flow through porous media, we approached the problem of static compacted sand from a soil mechanics point of view. A comparison of the spatial distribution of different water contents is visualized with a contour plot. The effect of particle morphologies on the spatial distribution of water content is also presented using quantitative plots.

3.3 Sample Description

Two different sands were used to compare the effect of particle morphology on water content: Ottawa sand (spherical) and Q-ROK sand (angular). The morphologies are shown in Figure 3.2 with Scanning Electron Microscopy (SEM) images (Penumadu et al. 2009). The sands were obtained from U.S. Silica, Berkeley Springs, WV having mineralogy with approximately 99.8% SiO_2 for Ottawa sand (20/40 Oil Frac) and 99.7% SiO_2 for #1 Q-ROK sand (U.S.Silica 1997). The specific gravity of both sands is 2.65. The grain size distributions for both sand types are shown in Figure 3.4. Four specimens were prepared for each sand morphology (Ottawa sand and Q-ROK sand) by adding an amount of water (0 g, 0.36 g, 0.54 g, and 0.72 g) to 6 g of dry sand yielding four different gravimetric water contents (GWC): 0%, 6%, 9%, and 12%. The water contents were chosen based on the typical water content in the field. The specimen containers were aluminum cylinders with an inner diameter of 12.7 mm and a height of 25.4 mm. After mixing the dry sand with water, the moist sand was split into three approximately equal amounts and compacted in three layers using an equal amount of tamping energy by dropping an aluminum rod with a mass of 71.12 g from an approximate height of 10 mm. Depending on the morphology and water content, each specimen has a different mass of sand placed in the container. Based on the mass of wet sand and its gravimetric water content, the

volumetric water content (VWC) of each specimen was obtained assuming that the sand was homogenously mixed, as shown in

Table 3.1. The estimated void ratios of each specimen are also shown in

Table 3.1. Radiographs of the specimens are shown in Figure 3.2. About 24 hours of equilibration time was allowed before acquiring the radiography and tomography data sets. Tomography experiments were performed with 360 projections for 180° of total rotation with a 0.5° increment. Ten images were taken at each projection for 1 s exposure time, and they were averaged to improve the signal to noise ratio. Additional experimental parameters are shown in Table 3.2.

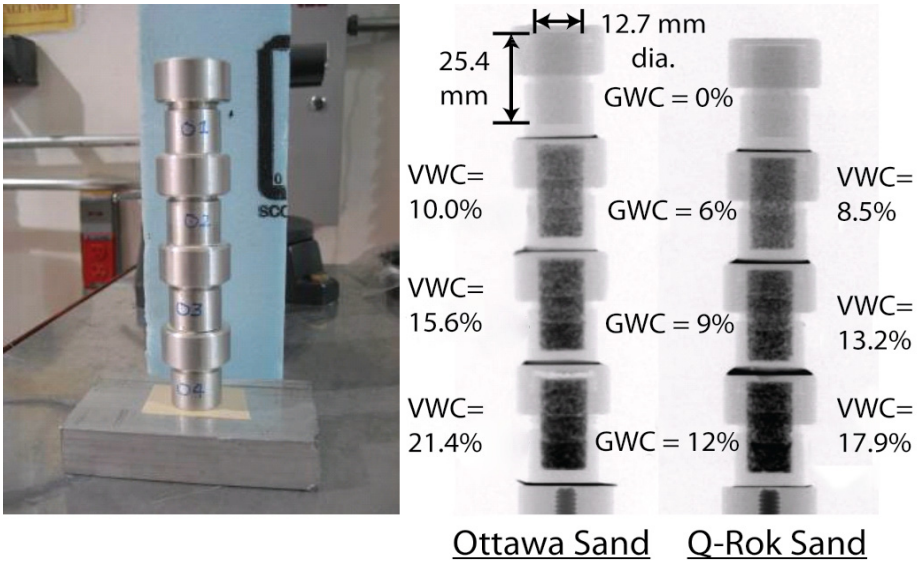


Figure 3.2: Picture of sand specimens contained in aluminum specimen holders and radiographs of Ottawa sand and Q-ROK sand

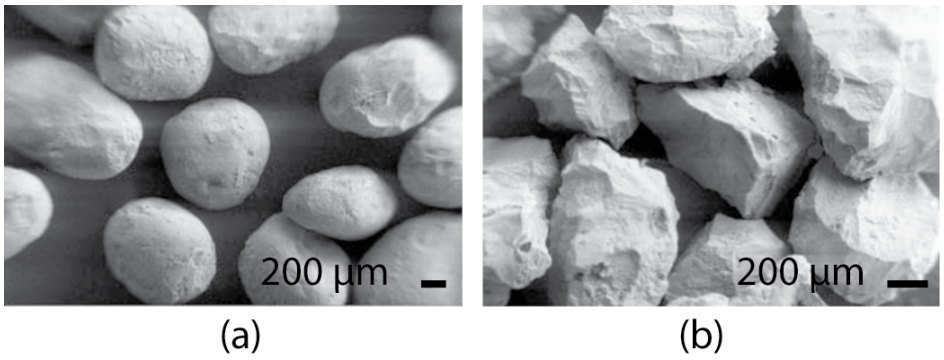


Figure 3.3: Morphology comparison of (a) Ottawa sand and (b) Q-ROK sand

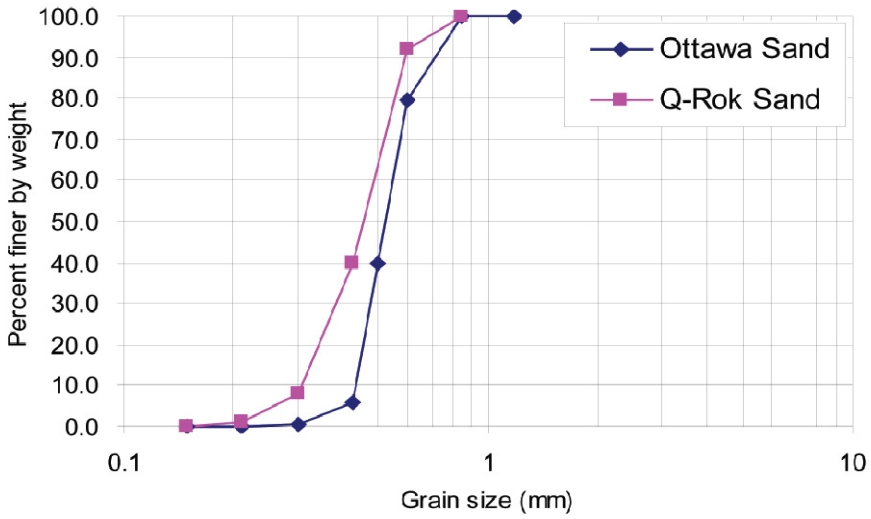


Figure 3.4: Grain Size distribution of Ottawa sand and Q-ROK sand

Table 3.1: Gravimetric water content (GWC), volumetric water content (VWC), total mass (mT) and void ratio (e) for each sand specimen

Sand Type	GWC (%)	6	9	12
Ottawa Sand	m_T (g)	5.38	5.57	5.74
	VWC (%)	10	15.6	21.4
	e	0.686	0.682	0.688
Q-ROK Sand	m_T (g)	4.57	4.72	4.79
	VWC (%)	8.5	13.2	17.9
	e	0.985	0.985	1.023

Table 3.2: Neutron imaging experimental parameters

Experimental Parameters	Value
L	6 m
D	10 mm
L/D	600
Fluence Rate	4.3×10^6 $cm^{-2}s^{-1}$
Avg. Diameter of the Sand	800 μm
Neutron Energy Range	Thermal (25 meV)
Spatial Resolution	250 μm (127 μm/pixel)
Number of Projections	360
Exposure Time	10 s/projection

3.4 Water Distribution Variation of Partially Saturated Sand

The dry sand and 3 wet sands with different gravimetric water contents are used for analysis. The dry sand image is formed from the attenuation of neutrons through sand and air. The wet sand image is a result of the sum of attenuations associated with water, sand, and air. The intensity of pixels corresponding to wet sand ($I_{Wet\ Sand}$) and dry sand (I_{Sand}) can be represented using equations 3.1 and 3.2, respectively. The macroscopic cross sections of

water and dry sand are denoted as Σ_w and Σ_s, respectively. The thicknesses of water and sand layers in the neutron ray path are denoted as t_w and t_s.

$$I_{Wet\ Sand}(x,y) = I_o(x,y)e^{-(\Sigma_w t_w + \Sigma_s t_s)} \quad 3.1$$

$$I_{Sand}(x,y) = I_o(x,y)e^{-\Sigma_s t_s} \quad 3.2$$

The image of wet sand is divided by the image of dry sand, as shown in Figure 3.5 to isolate the attenuation resulting from water only. An assumption is made that the mode of sand compaction was the same for each specimen of the same sand regardless of the water content. In reality, there is liquid between grains at the point of contact, and the mode of compaction of wet sand is different from that of dry sand due to pore pressure. Line plots of sand specimens with different GWC are shown in Figure 3.6. It is shown that the attenuation of dry sand is comparably lower than that of water. The dominant phase for neutrons in the granular system is the water. Thus, the error resulting from differences in sand compaction is negligible.

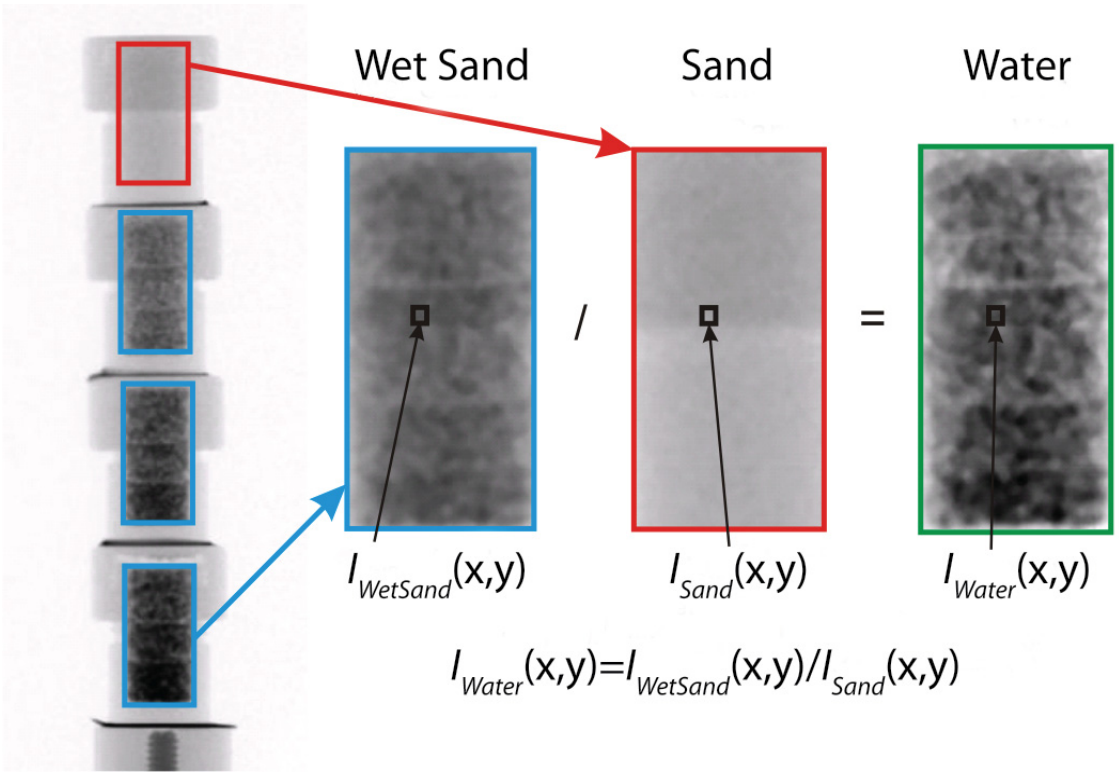


Figure 3.5: Image division process

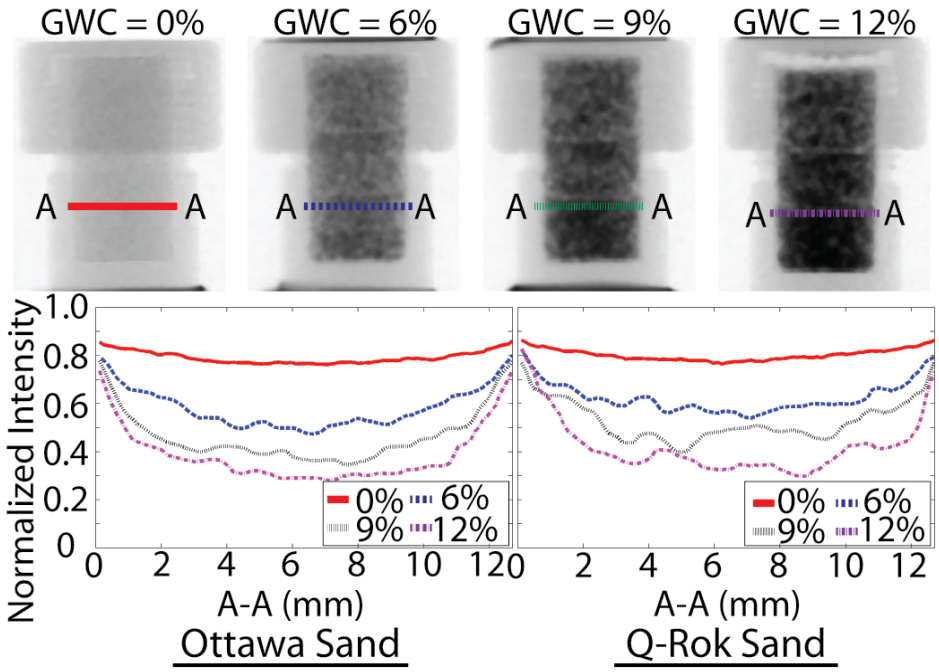


Figure 3.6: Attenuation comparison of line A-A for 0%, 6%, 9%, and 12% gravimetric water content (GWC) Ottawa sand and Q-ROK sand

A radiography image of water distribution is typically used to measure the 2-D water distribution in flow experiments. By normalizing a wet image with a dry reference image, one directly obtains the 2-D distribution of the water thickness t_w from equation 3.3.

$$t_w(x,y) = -\ln\left(I_{WetSand}(x,y) / I_{Sand}(x,y)\right) / \Sigma_w \qquad 3.3$$

By dividing the total water thickness (t_w) by the total container interior thickness (t_c) at each pixel, the water content (WC) at each pixel can be simply calculated from equation 3.4.

$$WC(x,y) = t_w(x,y)/t_c(x,y)\cdot 100\% \quad (3.4)$$

The *WC* distributions of both Ottawa sand (round particle shape) and Q-ROK sand (angular particle shape) are shown in Figure 3.7. The amount of water found along the height of the porous media increased with depth and could be the result of the compaction process coupled with gravity. For example, the sand specimen was prepared using three layers, each subjected to a similar amount of compaction energy from the tamping rod. This resulted in the largest compaction energy for the bottom layer. It is interesting to note that the interfaces of the three layers of compaction are clearly visible with significant variation in local water content (*WC*). In addition to the compaction layers, the morphology and packing density also introduce variations in the local *WC*. For example, 12% GWC sand has 21.4% VWC, and 12% GWC Q-ROK sand has 17.9% VWC. For the 21.4% VWC Ottawa sand specimen, the local *WC* varied approximately from 5% to 28%, and for the 17.9% VWC Q-ROK sand specimen, the local *WC* was distributed approximately from 5% to 25%. The large variation of local *WC* indicates that the current practice of measuring global water content does not consider the rather complex geometry of water content distribution. There is some possible error of the *WC* values at the boundaries of the images due to the manual selection process of image areas and a slight difference in the size of the actual sample area during the aluminum container fabrication process, but the

WC values in the interior of the image should correspond to equation 3.4, as this region averages over many sand particles.

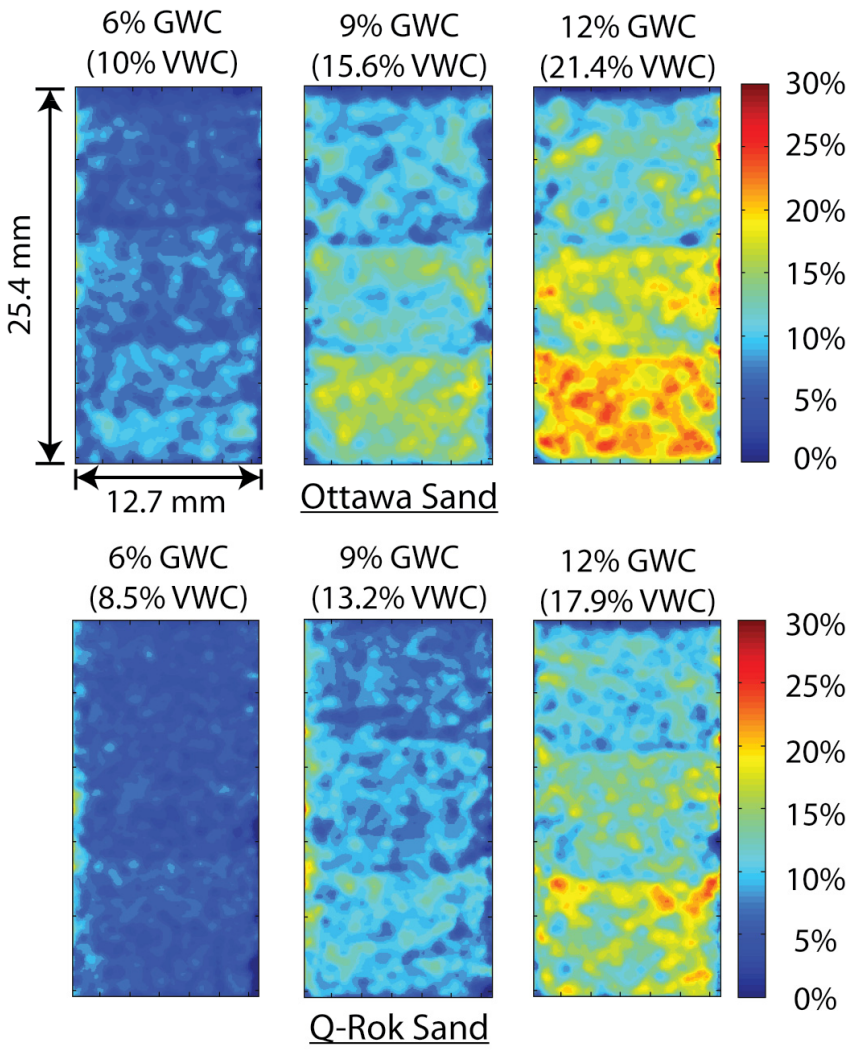


Figure 3.7: Contour plots of water content (WC) distribution from neutron radiography images

In the reconstructed tomography slices, water distribution analysis is performed for both Ottawa sand and Q-ROK sand. Equation 3.5 is used to approximate the water saturation (*WS*) in a voxel in the reconstructed slice.

$$WS(x,y,z) = \Sigma_{recon}(x,y,z)/\Sigma_{w} \cdot 100\% \quad 3.5$$

The macroscopic cross section value on each pixel of the reconstructed slice is denoted as Σ_{recon} and is the combination of attenuation values of the volumetric percentages of water, sand, and air. Since the total macroscopic cross section of water is 20 and 10^4 times larger than that of sand and air, respectively, equation 3.5 at most is discrepant by about 5%; thus it is a good approximation for the *WS*.

The effect of particle shape on water distribution was studied by comparing reconstructed slices of Ottawa sand and Q-ROK sand. The reconstructed slices at the interface between the bottom and middle compaction layers of each sand specimen were used for comparison. It can be visually inspected that the water spatial distribution of Q-ROK sand is less uniform than that of Ottawa sand, as shown in Figure 3.8. The standard deviations of pixel intensity histogram of tomograms were evaluated for each specimen with different global GWC as shown in Figure 3.9. It is shown that the standard deviation of Q-ROK sand is higher than that of Ottawa sand despite the lower VWC of Q-ROK sand. The standard deviation also increases as the GWC increases. The water distribution is more homogeneous for Ottawa sand than for

Q-ROK sand. The water saturation variation increases as the global GWC increases. There are many voids not filled with water between groups of sand grains in Q-ROK sand. For 12% GWC (21.4% VWC) Ottawa sand, the local *WS* was anywhere from 25% to 55%. For 12% GWC (17.9% VWC) Q-ROK sand, the local *WS* ranged from 20% to 50%. *WS* did not reach 100% due to the partially saturated state of specimen and the partial voxel effect. As the global water content increases, the maximum *WS* value increases, as shown in Figure 3.8. It is inferred that the volume of the water capillary films and bridges increases as the global water content increases. It was also observed from other research work that the volume of capillary bridges increase as the water content increases based on experiments using optical microscopy (Kohonen et al. 2004). The 100% *WS* value can be reached when the pore is fully filled with water. The imaging system also needs to have a resolution much smaller than the pore size. A comparison between the interfaces of each compaction layer is shown in Figure 3.10. Higher *WS* values and more uniform distribution are observed from top to bottom layer as the lower layer received more compaction energy in addition to gravity effect than the higher layer.

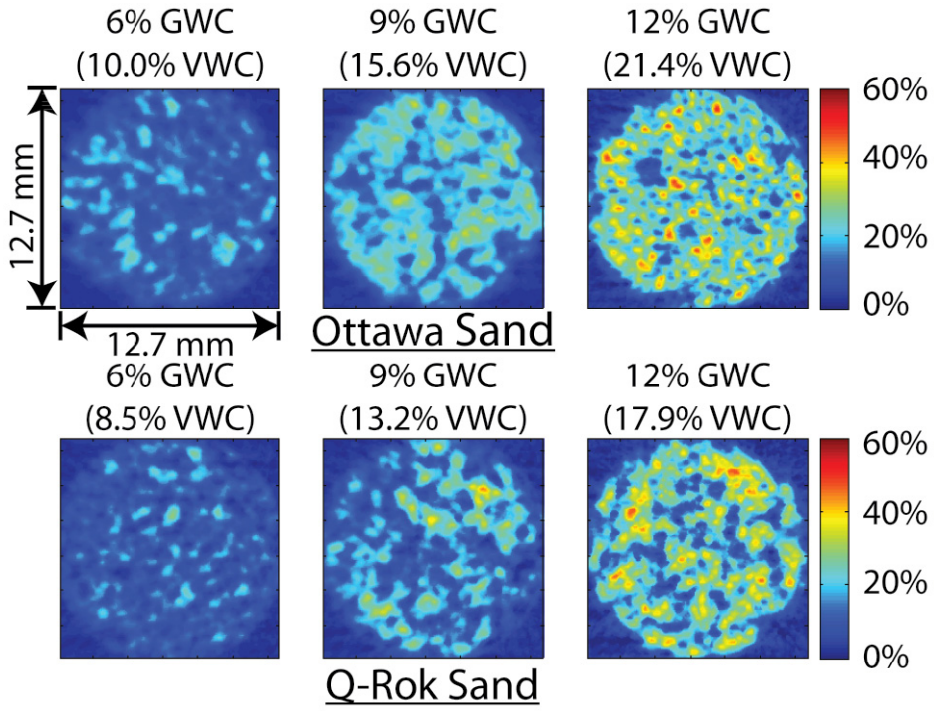


Figure 3.8: Contour plots of water saturation (WS) distribution on reconstructed tomography slices

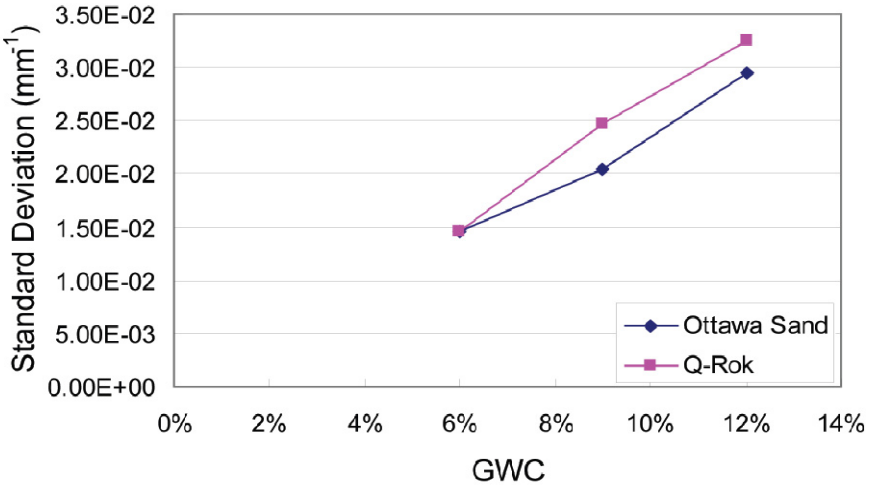


Figure 3.9: Comparison of standard deviation of histogram between Ottawa sand and Q-ROK sand

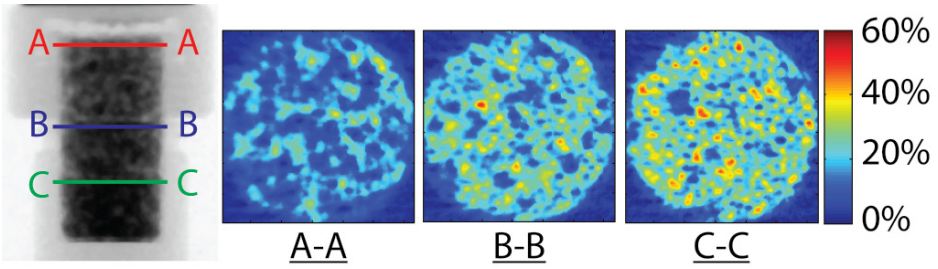


Figure 3.10: Comparison of the 3 compaction layers of top (A-A), middle (B-B) and bottom (C-C) for 12% GWC Ottawa sand

The obtainable measurement precision of the system with respect to the prepared GWC of each specimen was determined. The 10 raw images using one second exposure time were used to create an average projection image with 10 second exposure time for Ottawa sand. Then, the standard deviation of each pixel was calculated from 10 sets of tomography data. Three tomography slices corresponding to GWC of 6%, 9% and 12% were selected for each of 10 tomography sets. The maximum and average standard deviation values in mm^{-1} were divided by Σ_w = 0.3708 mm^{-1} and multiplied by 100% for each GWC to show the error bounds of the *WS* values. The result is plotted in Figure 3.11.

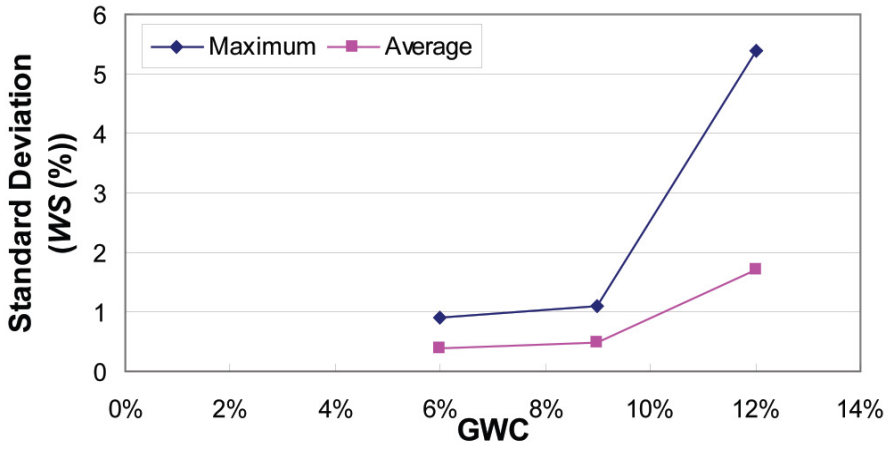


Figure 3.11: Maximum and average uncertainty of attenuation value comparison of Ottawa sand at GWC of 6%, 9%, and 12%

3.5 Conclusions

This paper explored the use of neutron imaging for studying water distribution in partially saturated granular materials. Silica sand specimens with two different morphologies (round and angular) were imaged using the neutron imaging facility at NIST. Neutron imaging is an alternative method to X-ray imaging for visualizing the three phases of wet granular materials without adding a contrast agent due to high natural contrast of neutrons for water, sand, and air phases with a large penetration depth suitable for investigating laboratory size samples non-destructively. The 250 μm spatial resolution (127 μm/pixel) images taken in this study was used to visualize features of water distribution around the sand particles (about 0.7 to 0.8 mm) adequately for 8 different specimens. Some example contour plots were presented to visualize the water distribution variation quantitatively from 2-D radiographs and 3-D tomograms. For example, the specimens with 12% GWC (21.4% VWC Ottawa sand and 17.4% VWC Q-ROK sand) showed local WC variation of 5% to 28% for Ottawa sand and 5% to 25% for Q-ROK sand. For 12% GWC sand, the highest saturation value (*WS*) was around 50%. Some difference in water distribution from specimens of two different grain morphologies was also observed. The rounded Ottawa sand qualitatively showed a more uniform distribution than the angular Q-ROK sand. The specimens were compacted with three layers, and the bottom compaction layer showed higher saturation of water than the top compaction layer possibly

due to the effect of the compaction process coupled with gravity effect. The technique of neutron imaging has a great potential for studying the mechanics of wet granular materials under loading and soil with transient flow in the future, and the approach presented in this study can be extended.

3.6 Appendix

The effect of sample scattering on image formation of the given sample is estimated by assuming that there is an infinite line charge of neutron scattering from water with a square cross-section (w), at a distance from the detector (O) as shown in Figure 3.12. The scattered neutron intensity I_S (with unit counts per unit time) and transmitted neutron intensity I_T on a detector pixel with area dp^2 can be shown in equation 3.6 and 3.7.

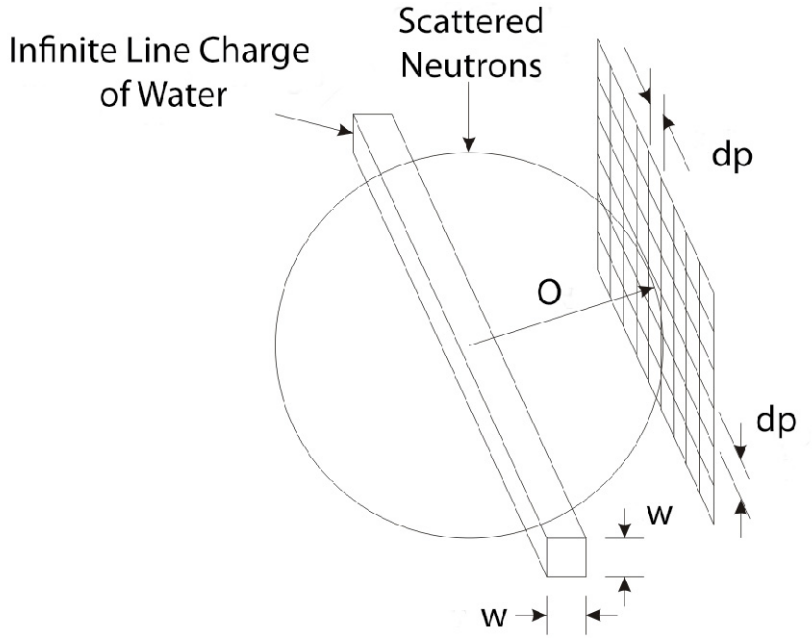


Figure 3.12: Effect of scattered neutrons on image formation from an infinite line charge

$$I_S = I_0 \cdot w \cdot (1 - e^{-\Sigma_w \cdot w}) \cdot dp^2 / (2 \cdot \pi \cdot O) \quad 3.6$$

$$I_T = I_0 \cdot e^{-\Sigma_w \cdot w} \cdot dp^2 \quad 3.7$$

For the images in this study, w = 1 mm, Σ_w = 0.3708 mm^{-1}, and O = 20 mm. The ratio of scattered neutrons to the transmitted neutrons can be estimated as in equation 3.8.

$$I_S / I_T = (e^{\Sigma_w \cdot w} - 1) \cdot w / (2 \cdot \pi \cdot O) = 0.0036 \quad 3.8$$

To determine if a correction is necessary to account for this scattered beam, one can compare I_S/I_T to the relative uncertainty due to counting statistics of the flat field I_{ff} for an image exposure time t_I, $\sigma = (I_{ff}\, t_I)^{-1/2}$. In particular, a

correction is required if I_S/I_T ~σ. For a fluence rate of 4.3 × 10^6 cm^{-2} s^{-1}, a detection efficiency of 20%, and a pixel pitch of 127 μm, $I_{ff} \approx 140$. Hence, $\sigma \sim 0.0036$ for an exposure time of 565 s. The integration time for each projection image during the experiment was only 10 s, and the infinite line charge assumption is the worst case scenario. Therefore, the authors concluded that the scattered beam effect introduces negligible uncertainty in this study.

3.7 References

Al-Raoush, R., and Alshibli, K. A. (2006). "Distribution of Local Void Ratio in Porous Media Systems from 3D X-ray Microtomography Images." *PHYSICA A*, 361(2), 441-456.

Al-Raoush, R. I., and Willson, C. S. (2005). "A pore-scale investigation of a multiphase porous media system." *Journal of Contaminant Hydrology*, 77(1-2), 67-89.

Alshibli, K. A., Sture, S., Costes, N. C., Frank, M. L., Lankton, M. R., Batiste, S. N., and Swanson, R. A. (2000). "Assessment of Localized Deformations in Sand Using X-Ray Computed Tomography." *Geotecnical Testing Journal*, 23(3), 274-299.

Arif, M., Hussey, D. S., and Jacobson, D. L. (2008). "Neutron Imaging for the Hydrogen Economy." Neutron Imaging and Applications, I. S. Anderson, McGreevey, R.L., and Bilheux, H.Z., ed., Springer Science+Business Media, LLC New York, NY.

de Beer, F. C., and Middleton, M. F. (2006). "Neutron Radiography Imaging, Porosity and Permeability in Porous Rocks." *South African Journal of Geology*, 109(4), 541-550.

Desrues, J., Chambon, R., Mokni, M., and Mazerolle, F. (1996). "Void ratio evolution inside shear bands in triaxial sand specimens studied by computed tomography." *Géotechnique*, 46(3), 529-546.

Han, J., Jin, Y., and Willson, C. S. (2006). "Virus Retention and Transport in Chemically Heterogeneous Porous Media under Saturated and Unsaturated Flow Conditions." *Environmental Science & Technology*, 40(5), 1547-1555.

Hassanein, R., Meyer, H. O., Carminati, A., Estermann, M., Lehmann, E., and Vontobel, P. (2006). "Investigation of Water Imbibition in Porous Stone by Thermal Neutron Radiography." *Journal of Physics D: Applied Physics*, 39(19), 4284-4291.

Jaeger, H. M., Nagel, S. R., and Behringer, R. P. (1996). "Granular solids, liquids, and gases." *Reviews of Modern Physics*, 68(4), 1259.

Jasti, J. K., and Fogler, H. S. (1992). "Application of Neutron Radiography to Image Flow Phenomena in Porous Media." *AIChE Journal*, 38(4), 481-488.

Kohonen, M. M., Geromichalos, D., Scheel, M., Schier, C., and Herminghaus, S. (2004). "On capillary bridges in wet granular materials." *Physica A: Statistical Mechanics and its Applications*, 339(1-2), 7-15.

Lanza, R. C. (2008). "Homeland Security and Contraband Detection." Neutron Imaging and Applications, I. S. Anderson, McGreevey, R.L., and Bilheux, H.Z., ed., Springer Science+Business Media, LLC, New York, NY.

Lewis, J. T., and Krinitzsky, E. L. (1976). "Neutron Radiation in the Study of Soil and Rock." Practical Applications of Neutron Radiography and Gaging, H. Berger, ed., American Society for Testing and Materials, Baltimore, Md, 241-251.

Lopes, R. T., Bessa, A. P., Braz, D., and de Jesus, E. F. O. (1999). "Neutron computerized tomography in compacted soil." *Applied Radiation and Isotopes*, 50(2), 451-458.

Lu, N., Zeidman, B. D., Lusk, M. T., Willson, C. S., and Wu, D. T. (2010). "A Monte Carlo paradigm for capillarity in porous media." *Geophys. Res. Lett.*, 37(23), L23402.

Milczarek, J. J., Czachor, A., Abd El-Ghany, E. A., and Wisniewski, Z. (2005). "Dynamic Neutron Radiography Observations of Water Migration in Porous Media." *Nuclear Instruments and Methods in Physics Research Section A: Accelerators, Spectrometers, Detectors and Associated Equipment*, 542(1-3), 232-236.

Nakanishi, T. M. (2008). "Neutron Imaging Applied to Plant Physiology." Neutron Imaging and Applications, I. S. Anderson, McGreevey, R.L., and Bilheux, H.Z., ed., Springer Science+Business Media, LLC New York, NY.

Oda, M., Takemiura, T., and Takahashi, M. (2004). "Microstructure in shear band observed by microfocus X-ray computed tomography." *Geotechnique*, 54(8), 539-542.

Penumadu, D. (2008). "Material Science and Engineering with Neutron Imaging." Neutron Imaging and Applications, I. S. Anderson, McGreevey, R.L., and Bilheux, H.Z. , ed., Springer Science+Business Media, LLC New York, NY.

Penumadu, D., Dutta, A., Luo, X., and Thomas, K. (2009). "Nano and Neutron Science Applications for Geomechanics." *KSCE Journal of Civil Engineering*, 13(4), 233-242.

Pleinert, H., and Degueldre, C. (1995). "Neutron radiographic measurement of porosity of crystalline rock samples: a feasibility study." *Journal of Contaminant Hydrology*, 19(1), 29-46.

Scheel, M., Seemann, R., Brinkmann, M., Di Michiel, M., Sheppard, A., Breidenbach, B., and Herminghaus, S. (2008). "Morphological clues to wet granular pile stability." *Nat Mater*, 7(3), 189-193.

Schiffer, P. (2005). "Granular physics: A bridge to sandpile stability." *Nat Phys*, 1(1), 21-22.

Trabold, T. A., Owejan, J. P., Gagliardo, J. J., Jacobson, D. L., Hussey, D. S., and Arif, M. (2009). "Use of Neutron Imaging for Proton Exchange Membrane Fuel Cell (PEMFC)." Handbook of Fuel Cells, W. Vielstich, H. A. Gasteiger, and H. Yokokawa, eds., John Wiley and Sons, West Sussex, England.

Tullis, B. P., Lindsay, J. T., and Wright, S. J. (1994). "The Imaging of Wetting Front Instabilities in Porous Media Using Neutron Radioscopy." *Nondestr. Test. Eval.*, 11(2-3), 97-106.

U.S.Silica. (1997). "Product data sheet."

Watkin, K. L., Bilheux, H. Z., and Ankner, J. F. (2008). "Probing the Potential of Neutron Imaging for Biomedical and Biological Applications." Neutron Imaging and Applications, I. S. Anderson, McGreevey, R.L., and Bilheux, H.Z., ed., Springer Science+Business Media, LLC, New York, NY.

Wellington, S. L., and Vinegar, H. J. (1987). "X-Ray Computerized Tomography." *Journal of Petroleum Technology*, 39(8), 885-898.

CHAPTER 4. HIGH RESOLUTION DUAL MODALITY IMAGING OF PARTIALLY SATURATED SAND

This chapter is revised based on a paper published by Felix Kim, Dayakar Penumadu et al. :

Kim, F. H., Penumadu, D., Gregor, J., Kardjilov, N. and Manke, I. (2013). High resolution neutron and X-ray imaging of granular materials. Journal of Geotechnical and Geoenvironmental Engineering, American Society of Civil Engineers (ASCE), 139(5), 715-723.

My primary contributions to the paper included: (i) Understanding high resolution neutron imaging and micro focus X-ray imaging, (ii) gathering and reviewing literature, (iii) performing neutron and X-ray imaging at Helmholtz-Zentrum-Berlin, (iv) understanding dual modality of neutron and X-ray, (v) processing, analyzing, and interpretation of the experimental data, (vi) most of the writing.

4.1 Abstract

High spatial resolution (~13.7 μm/pixel) neutron tomography was performed on partially water-saturated compacted silica sand specimens with two different grain morphologies (round and angular) at Helmholtz Zentrum Berlin (HZB) using cold neutrons at the CONRAD beam line. A specimen mixed with heavy water (D_2O) was imaged for contrast comparison purposes. Microfocus X-ray imaging was also performed on these specimens with slightly higher resolution (~11.2 μm/pixel) using geometric magnification to locate the solid phase (silica particle boundaries) more precisely. Image processing was performed to remove unwanted gammas detected due to the gadox scintillator used for the high resolution neutron imaging system. The visualization of solid, gas, and liquid phases for different grain morphologies are presented at the grain level. Using dual-modal contrast possible from simultaneous use of neutrons and X-rays, the authors introduce for the first time an improved ability to distinguish solid silica, liquid water, and gas phases. Quantitative analysis using 3D tomography data is demonstrated for obtaining void ratio, void percentage variation over the height and particle size distribution.

4.2 Introduction

Soil is a three-phase material composed of solid, gas, and liquid phases. The solid phase is composed of discrete particles, and the interactions between

solid particles affect the deformation behavior of the soil mass. Applied force on soil mass is transferred through contact forces at the contact points, and it is important to quantify the contact forces to understand soil deformation behavior. However, there can be as many as 5 million contacts within 1 cm^3 of a fine sand for example, and particle scale soil mechanics was impractical (Lambe and Whitman 1969). Therefore, traditional continuum assumption has been applied for interpreting soil and granular mechanics experiments, related theories and numerical simulations at a laboratory specimen scale. However, it has been found that the continuum assumption does not apply well with granular materials (Peters 2005). In order to account for the discrete nature of granular materials, a numerical simulation method, such as discrete element method (DEM), was developed and applied (Bardet and Proubet 1991; Cundall and Strack 1979; Iwashita and Oda 1998; Yimsiri and Soga 2010).

Several experimental studies were also performed to characterize the microstructure of deformed and unsheared soil specimens to improve the understanding of the particle scale behavior of soil by using various imaging techniques including optical imaging, Scanning Electron Microscopy (SEM), X-ray and most recently neutron imaging (Kim et al. 2012; Muhunthan and Chameau 1997; Oda 1972a; Oda 1972b; Oda 1972c; Yang 2005). Due to its nondestructive nature, X-ray and synchrotron imaging has been popularly applied to study granular materials and flow through porous media for the past 20

years (Al-Raoush and Alshibli 2006; Desrues et al. 1996; Otani 2010; Razavi et al. 2007; Wang et al. 2004; Wellington and Vinegar 1987; Wildenschild et al. 2005; Wildenschild et al. 2002). The synchrotron imaging system provides spatial resolution in the order of microns and below with high brilliance (up to 10^{14}~10^{18} photons·s^{-1}·mm^{-2}·$mrad^{-2}$·0.1%BW^{-1}) (Sutton et al. 2002). Brilliance is defined as the number of photons/second/source area/solid angle/band width (Sham and Rivers 2002). However, X-rays have a much lower attenuation coefficient to water than that of the silica solid phase, and the water phase does not show good contrast in the image especially for higher energy X-rays (> 40 to 50 keV) which are needed for a reasonable depth of penetration in soil sample characterization using laboratory based X-ray sources. A contrast agent is often added in water to improve the contrast (Al-Raoush and Willson 2005; Scheel et al. 2008; Schnaar and Brusseau 2005), but it could change the contact angle of the liquid with solid silica phase, which may change the wetting and seepage behavior depending on the type and amount of contrast agent used. It was shown that the contact angle influences the capillary pressure-saturation relations in porous media (Ishakoglu and Baytas 2005). On the other hand, the water phase shows high contrast in the neutron image even with a relatively low flux (10^{6}~10^{7} neutrons·cm^{-2}·s^{-1}). The high contrast mechanism with water has been utilized to visualize the flow through porous media both with radiography and tomography at relatively low resolution (>100 μm/pixel) (Carminati et al.

2007; de Beer and Middleton 2006; Lewis and Krinitzsky 1976; Lopes et al. 1999; Milczarek et al. 2005; Pleinert and Degueldre 1995; Tullis et al. 1994). It is not until recently that improvements in spatial and temporal resolution of neutron imaging detectors have been made.

The water phase in partially saturated sand significantly changes the shear strength and particle level force chain networks significantly from those of the dry state due to capillary bridges formed around sand grain contacts (Schiffer 2005). The complex distribution of water in the pore spaces of rocks and soil also fundamentally affects the conductivity and diffusivity properties (Berkowitz and Hansen 2001), and also provides important information related to modeling two-phase flow associated with wetting and non-wetting phases for studying contaminant transport through the vadose zone. Many studies in the past have duly considered the importance of distribution of the micro-fabric (geometric arrangement of particles) corresponding to solid phase using impregnated sand samples, thin-sectioning and optical micrsocopy. The experimental study of liquid phase and its spatial distribution has not been considered for partially saturated specimens due to a lack of characterization techniques such as the one described in this paper. Additional experimental studies accounting the liquid phase of soil are needed to understand the true and complex deformation behavior of partially saturated soils. Recent work based on discrete element simulations is demonstrating the importance of incorporating micro-fabric tensor

and the need for related experiments to more accurately use critical state concepts to describe anisotropy often observed for granular materials (Li and Dafalias 2012).

In the recent paper published by authors, the concept of neutron tomography was applied to visualize the complex water distribution in partially saturated sand specimens with various water contents at a relatively coarse resolution (127 μm/pixel) neutron imaging detector available at the time (Kim et al. 2012). Due to the coarse resolution, the fine features of grain and water capillary bridges were not clearly visualized.

In this paper, the distributions of water in partially saturated sand specimens are visualized with high spatial resolution neutron (13.7 μm/pixel) tomography images. Recently, the detector technology has improved significantly by applying a very thin (~10 μm) gadox scintillator with high resolution (2048 × 2048 pixels) CCD camera (Kardjilov et al. 2011). Cold neutrons were used instead of thermal neutrons to reduce the integration time for high resolution imaging while improving the contrast of water which is more adequate for detecting finer water capillary films. Due to the high resolution, the three phases (solid, gas, and liquid) are visualized clearly. High resolution X-ray tomography experiments were also performed to provide complementary contrast using a laboratory microfocus X-ray machine. Comparisons between round and angular sand with their water distribution are made by 3D visualization. High resolution

neutron and X-ray tomography techniques are introduced as complementary techniques to study wet granular materials at the grain level. The dual modality (neutron and X-ray) imaging technique is also expected to be applied on flow through porous media simulation based on pore geometry imported from reconstructed images (Auzerais et al. 1996; Ferréol and Rothman 1995; Silin et al. 2011) to validate the numerical results without using a contrast agent.

4.3 Materials and Methods

4.3.1 Materials and Specimen Description

Naturally occurring silica sands with two different grain shape morphologies were obtained from U.S. Silica: 20/40 Oil Frac Ottawa Sand (Round) and #1 Q-ROK Sand (Angular). Ottawa sand is composed of 99.8 % SiO_2 and Q-ROK sand have 99.7% SiO_2. Both sands have an average diameter of approximately 600~700 μm. The morphology comparison of Ottawa sand and Q-ROK sand are shown in Kim et al. (Kim et al. 2012). Two different kinds of liquid were used in the present study: Deionized water (H_2O) and heavy water (D_2O).

Three compacted sand specimens were prepared for high resolution neutron and X-ray tomography experiments: Ottawa sand with water, Q-ROK sand with water, and Ottawa sand with heavy water. The three specimens were imaged with both high resolution neutron and microfocus X-ray imaging systems.

The compacted partially saturated silica sand specimen was prepared first by mixing the silica sand (5 g) with liquid (0.6 g) to make the gravimetric water content of 12 %. Figure 4.1 shows a picture and a transmission neutron radiograph of mixed wet sand placed in a custom made aluminum specimen holder compacted in three layers. The specimen preparation procedure was performed as follows. Approximately 1/3 of the volume of the specimen holder was filled and the layer was compacted by tamping 25 times with an aluminum circular tamping a rod. The mass of the tamping rod was 38.4 g, and it was dropped from about 10 mm height each time. The process is repeated for the next 2 layers. The inner dimension of the aluminum specimen holder was about 10 mm (dia.) × 23 mm (height). Depending on the packing density, the total weight of the specimen varied for each specimen. The mass of the silica sand in the specimen holder after drying was also obtained at the end of imaging as shown in Table 4.1. The specimens were left for at least 24 hours after compaction to reach the equilibrium state with water phase before taking tomography.

Table 4.1: Measured silica sand and water phase compositions and liquid content of each specimen

	Ottawa sand with water	Q-ROK sand with water	Ottawa sand with heavy water
Dry sand (g)	2.94	2.41	3
Liquid (g)	0.36	0.49	0.5
Liquid content (%)	12.24	20.33	16.67

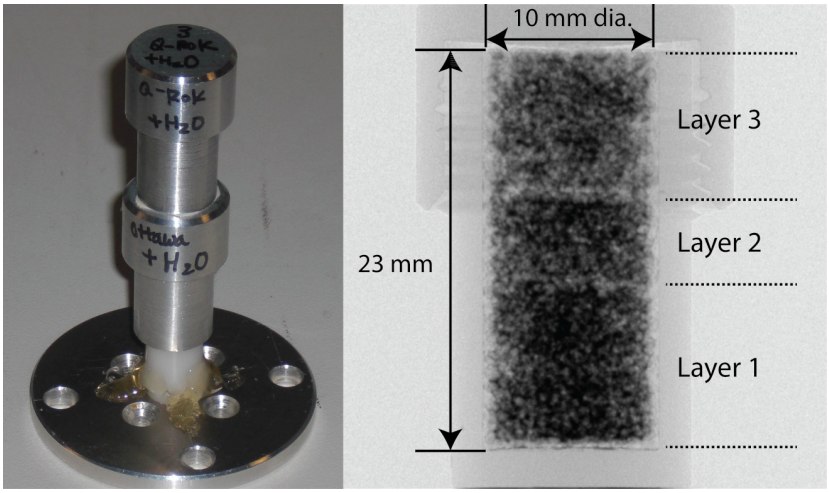


Figure 4.1: Specimen dimension and description

4.3.2 Principles of Neutron and X-ray Imaging and Tomography

The basic principles of neutron and X-ray imaging are well published (Buzug 2008; McCullough 1975; Tobin et al. 2009; Wildenschild et al. 2002), and some of the more relevant and advanced aspects applied to geomaterials are highlighted in this paper. Neutrons and X-rays are both penetrating radiation, but they differ in the interaction mechanism with condensed matter. Neutrons mainly interact with the nucleus of an atom while X-rays mainly interact with the electron clouds. The difference in the interaction mechanism provides difference in the contrast in the images obtained using either neutrons or X-rays.

As X-rays or neutrons penetrate matter, they are subject to attenuation either through absorption or by scattering. Only unattenuated particles are recorded by a detector. The amount of absorption and scattering for a material is described by its attenuation coefficient (μ) for X-rays or total macroscopic cross section (Σ_T) for neutrons. The attenuation coefficient and total macroscopic cross section is energy dependent. The X-ray attenuation coefficients and neutron macroscopic cross sections for the three phases (Water, air and silica) are presented in Table 4.2.

Table 4.2: Neutron macroscopic cross section and X-ray attenuation coefficient comparison of the 3 phases (Water, Air, and Silica)

	Attenuation coefficient, Macroscopic cross section (cm^{-1})	
	X-ray (100 keV)	Cold neutron (7.3 meV)
H_2O	0.17	5.67
O_2	0.00044	0.00046
SiO_2	0.43	0.29

The attenuation of neutron or X-ray is modeled using a linear process, and the transmitted intensity of neutrons through a sample can be described by Lambert - Beer's law shown in equation 4.1.

$$I = I_0 e^{-\int \Sigma_T(x)dx} \qquad 4.1$$

I_0 is the beam intensity before passing through the sample, I is the beam intensity after passing through the sample, Σ_T is the total macroscopic cross section (cm^{-1}), and *e* is 2.718281828. The attenuation coefficient, μ, can be used interchangeably with Σ_T for X-ray imaging. The transmitted beam intensity is detected by a detector, and a radiograph is produced. When several projections are taken at different angular orientations of a sample by rotating the sample with a fine rotational increment through 180°, tomographic reconstruction can then be performed to visualize the sample in 3D. By knowing the overall attenuation from

all directions for the sample being imaged, it is possible to reconstruct the attenuation value (Σ_T) distribution spatially.

Reconstruction is commonly performed with filtered back-projection algorithm (Kak and Slaney 2001). The reconstruction process produces a stack of 2D axial cross sectional images containing attenuation value (Σ_T) distribution. The reconstructed slices can be stacked together to be visualized in 3D. The 3D data taken in the research was visualized with Avizo (version 6.3), using a graphic workstation with 8 cores (3.20 GHz each) and 64 GB memory with ability to analyze large tomography data.

4.3.3 High Resolution Neutron Tomography

Neutron tomography experiments were conducted at the cold neutron radiography and tomography (CONRAD) beam line at Helmholtz Center Berlin for Materials and Energy (HZB) in Germany. It is a dedicated neutron imaging beam line with cold neutron spectrum between 2 and 10 Å with a peak at 3.35 Å. The cold neutrons generated from a 10 MW reactor are transported through a curved neutron guide to minimize high energy neutrons and gammas from the moderator reaching the detector. Cold neutrons have a higher macroscopic cross section for water than thermal neutrons, and it improves the detection capability of smaller amount of water.

The high resolution imaging setup by consisting of a scintillator combined with a charge coupled device (CCD) camera detector was used for the research

(Kardjilov et al. 2011; Kardjilov et al. 2009), and the setup is shown in Figure 4.2. The detector has a flexible option for changing different scintillators, and a 10 μm thick scintillator based on Gadox ($Gd_2O_2S(Tb)$) reduced the light blooming effect significantly. The CCD camera (Andor DW436N-BV) has 2048 × 2048 pixels with 13.5 μm pixel pitch. The camera provides 16 bit dynamic range. Nikon lens (AF Micro-Nikkor 200 mm f/4D) with 1:1 magnification was used. The collimation ratio (*L/D*) was chosen as 500 to minimize the image blurring due to the beam divergence. The aperture diameter (*D*) was chosen as ϕ10 mm, and the distance from the pin hole to the sample (*L*) is about 5 m. The flux at this configuration is approximately 6 × 10^6 neutrons·cm^{-2}·s^{-1}. The combined effect of geometric unsharpness from *L/D*, light blooming effect from scintillator and CCD sensor sampling resulted in approximately 39 μm spatial resolution (13.7 μm/pixel) was determined based on the point where the modulation transfer function reaches 10% of its maximum.

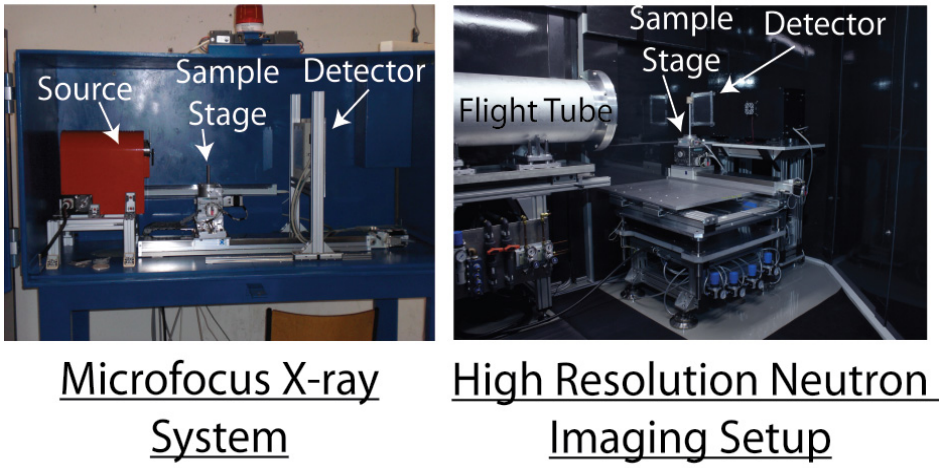


Figure 4.2: Microfocus X-ray system and high resolution neutron imaging setup at HZB

In a conventional neutron imaging setup, a 250 μm thick LiFZnS scintillator is often used, and the thickness of the scintillator is often the limiting factor of the spatial resolution. In this research, spatial resolution was improved significantly by using a much thinner (10 μm) gadox scintillator. Gadox also has a higher cross section to neutrons than Li based scintillator, and it helped reduce the exposure time. However, the gadox scintillator is more sensitive to gammas than the Li based scintillator. Also, the gadox scintillator is approximately two orders of magnitude lower in neutron conversion efficiency than a Li based scintillator. As a result, a significant amount of gammas were detected as higher intensity spots shown in the image. In order to overcome the problem, three images with the same exposure time were taken at each angle of rotation since

the gamma detection is random spatially. The median value of the three images was chosen for each pixel since it is less likely that all three images have detected gammas for the same pixel. The process was performed during image acquisition, and only the final images after the median combination process were analyzed.

Five hundred projections were acquired over a full 360° rotation. Each projection was obtained using a 30 sec exposure time. As three images were taken for each projection to remove gammas, the total acquisition time for each specimen was thus about 12 hours including image readout time. The data was reconstructed using the parallel beam filtered backprojection algorithm implemented by the Octopus® software package (version 8.4). The neutron and X-ray imaging parameters are shown in Table 4.3.

Table 4.3: The imaging parameters of neutron and X-ray tomography

Parameter	Neutron	X-ray
Energy (keV)	7.30E-06 (Peak)	100 (Max)
Pixel size (μm)	13.7	11.2
Detector pixel number	2048 × 2048	2316 × 2316
Field of view (mm × mm)	28 × 28	25.9 × 25.9

4.3.4 Microfocus X-ray Tomography

After completion of high resolution neutron tomography, X-ray tomography experiments were subsequently performed on the sand specimens with a laboratory microfocus X-ray tomography system available at the facility. Hamamatsu 150 kV microfocus X-ray source combined with a flat panel detector (2316 × 2316 pixels) with 50 μm detector pixel pitch was used. The sample was magnified about 4.5 times, resulting in an effective image pixel size of 11.2 μm. The source voltage was set to 100 kV. The exposure time was 2 sec, and 1000 projections were again acquired for a full 360° rotation. Reconstruction was performed using the cone beam filtered backprojection algorithm implemented by the Octopus® software package (version 8.4).

4.4 Results and Discussions

4.4.1 Neutron Contrast Comparison

Radiographs and tomography slices of the three specimens taken with neutron imaging are presented in Figure 4.3. The three compaction layers are visible from the radiographs due to high attenuation of water to neutrons. The contrast difference of water (H_2O) and heavy water (D_2O) is shown. It is also shown that water has migrated to the bottom of the specimen due to gravity effect coupled with compaction process until the specimen reached the equilibrium state. In radiographs, the darker the area, the more water is present

through thickness. In reconstructed slices, the contrast is inverted since the image intensity represents the attenuation value. Water has high attenuation value compared to other phases in the specimen for neutrons, and the water phase is shown as the brighter spots in the reconstructed slices. Heavy water shows a more favorable contrast than that of water. The attenuation coefficient of D_2O is approximately 0.64 cm^{-1} for cold neutrons.

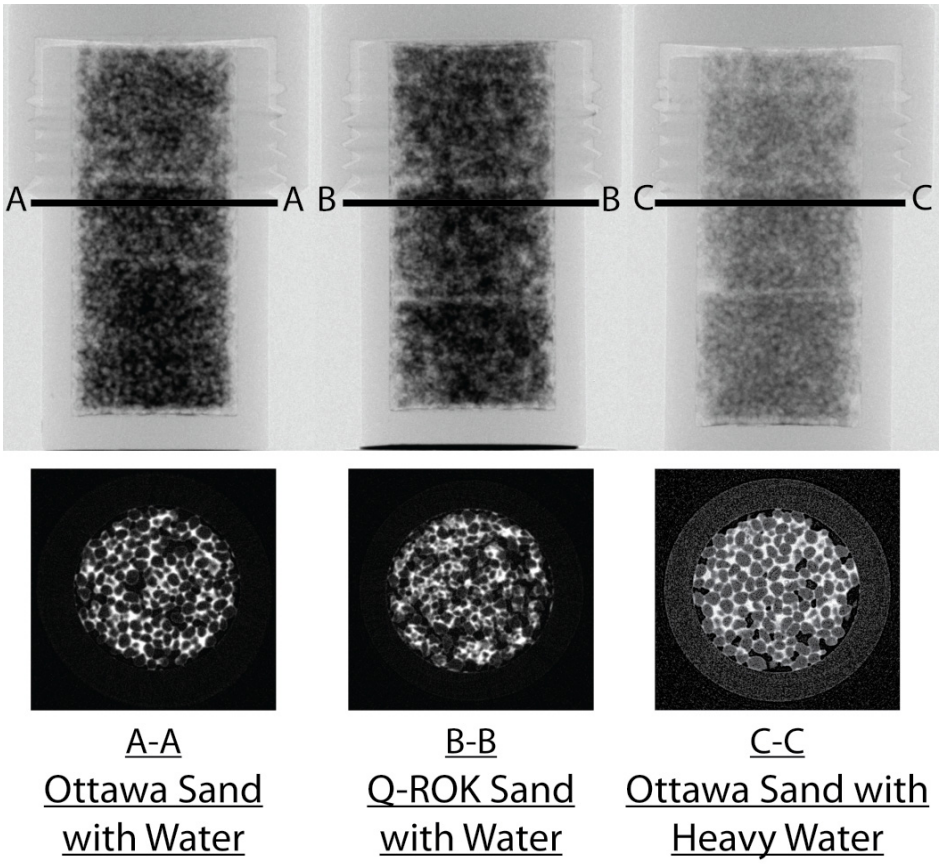


Figure 4.3: Contrast comparison of the three specimens shown from neutron radiographs and tomography slices

4.4.2 Effect of Compaction and Grain Shape Morphology on Void and Water Distribution

The dependency of spatial water distribution for the compacted sand assembly due to different grain shapes are shown by using example neutron tomography slices in Figure 4.4. It is visually observed that water is more

homogenously distributed for Ottawa sand with rounded shape than Q-ROK sand with angular shape.

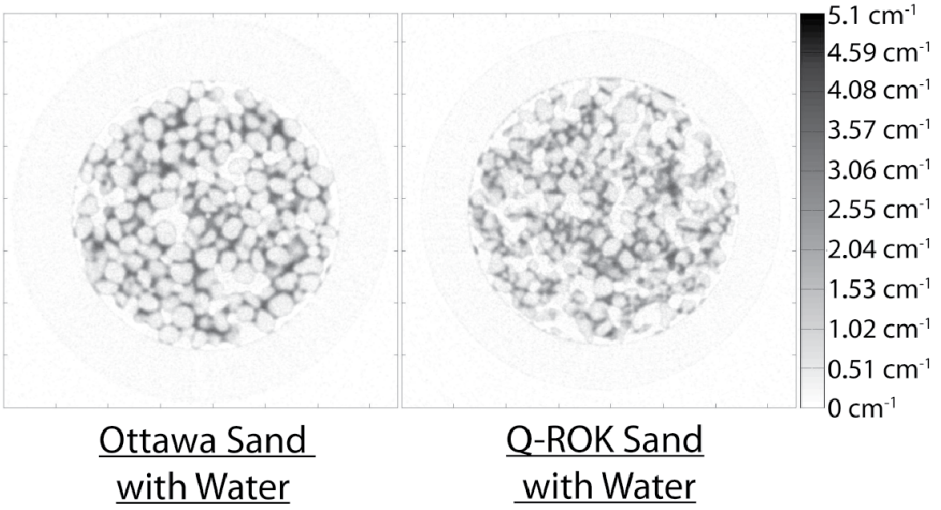


Figure 4.4: Comparison of water distribution resulting from different sand grain shape morphologies

In Figure 4.5, both neutron radiographs and orthoslices are shown. An orthoslice is an interior orthogonal slice of 3D data. The radiographs show the through thickness integrated attenuation behavior, and the orthoslices show the interior sections of the specimens. Bulking structure was observed around the bottom of the compaction layers. Bulking structure is a loose grain structure occurring in moist sand, and a fairly stable structure is obtained due to capillary films and bridges (Holtz and Kovacs 1981). As the neutron radiograph clearly

shows the interface of the compaction layers, one can notice that there are some bulking structures at the bottom of the compaction layers in the orthoslice. The cross sectional orthoslices at the top and bottom of the compaction layer 2 are also shown in Figure 4.5, and a significant difference of void space and additionally the degree of saturation are observed between top and bottom of the compaction layer. It is shown that sand grains are compacted more densely and water has filled the voids more completely at the top area of the compaction layer where the compaction effect was more directly transferred than the bottom area of the compaction layer. It shows that the compaction energy does not reach far enough to compact the sand grains and distribute water uniformly. As an example, one can infer that a failure in a soil specimen can be initiated from the interface of compaction layers due to such large local void ratios. In the Q-ROK sand specimen, bulking effect was observed at the interfaces of compaction layers, but similar structures are also observed throughout the specimen. It shows that the grain shape morphology has also affected the final void and water distribution after compaction for partially saturated compacted specimens.

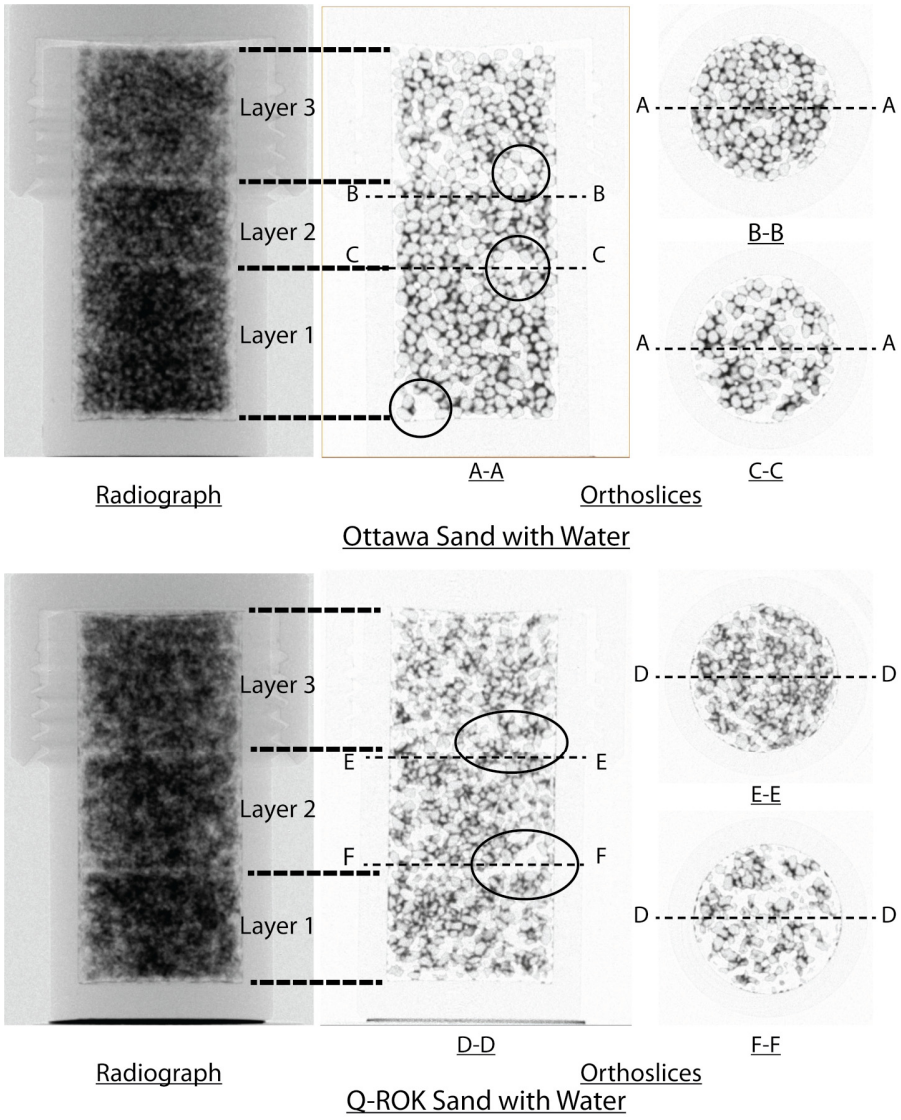


Figure 4.5: Effect of compaction and grain shape morphology on void and water distribution

4.4.3 Dual Modality

Dual-modal contrast of neutrons and X-rays is presented in Figure 4.6 corresponding to the cross section comparison presented in Table 4.2. The water phase showed good contrast in the neutron image, but other phases did not have good enough contrast to be distinguished easily. On the other hand, the particle location of the solid silica phase is presented more precisely in the X-ray image while the water phase had low contrast with the air phase. Thus, neutrons and X-rays have dual-modal contrast for the three-phase system relevant to geotechnical engineering by providing complementary information. The water distribution information can be obtained from neutron images, and the sand fabric information can be obtained precisely from the X-ray images. Using this approach, we now have the ability to image samples from the environment without the need for contrast agents.

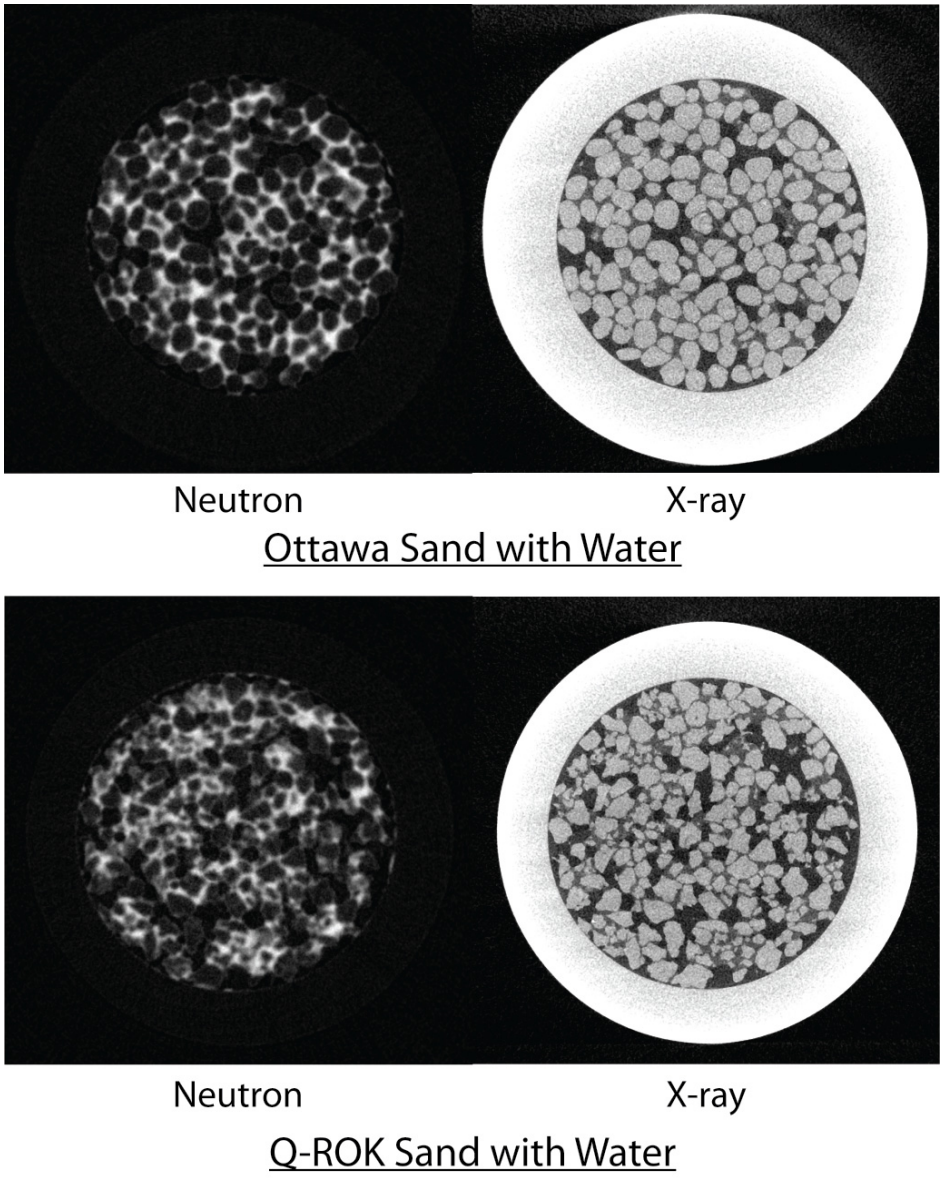


Figure 4.6: Dual modality of neutron and X-ray tomography data

4.4.4 Application to Soil Mechanics

The 3D tomography images provide opportunity to visualize the interior of the soil mass. In order to obtain quantitative information, proper image processing algorithms need to be applied. For verification purposes, the bottom half of the specimen volume was chosen for image processing and quantitative analysis. By taking advantage of the dual modality, the silica sand phase information can be segmented from the X-ray tomography data, and the water phase information can be segmented from the neutron tomography data. The image processing sequences applied on the X-ray tomography data are shown in Figure 4.7. Smoothing of the X-ray tomography data was done by applying a 3D median filter (Figure 4.7a) and was thresholded to obtain the sand grain phase (Figure 4.7b). The images are thresholded by using a factorization algorithm that maximizes the variances in the image histogram (Otsu 1979). The threshold value was verified from image histogram, and the thresholded result was also visually inspected for appropriateness. Opening algorithm was applied to further smooth the images (Figure 4.7c). Due to the limited resolution, the boundaries between different sand grains are difficult to resolve, and they are often connected. The grains are separated by applying a 3D watershed algorithm as shown in Figure 4.7d. The individual sand grains can be labeled and counted as shown in Figure 4.7e. Based on the thresholded results from X-ray tomography data, the void ratio is calculated and compared with the actual measured value in

Table 4.4 in a predictive sense. The values match very closely, and the calculated values are consistently smaller than the measured values. It is thought to be due to inevitable error with the thresholding process. Even though there is a high contrast of silica sand phase compared to the water phase, it is difficult to perfectly threshold only the silica phase and some lower contrast water phase is also included in the segmented results at the grain boundaries. As a result, the sand phase is slightly overestimated and the void phase is slightly underestimated. Based on the thresholded results of X-ray tomography data, the void percentages (void volume/ container volume) were computed over the height of the specimens and compared to the compaction layers presented from neutron radiographs as shown in Figure 4.8. An abrupt change of void percentage is observed at the interface between compaction layer 1 and 2. Additionally, the variation of the local void ratio in a small volume of interest (200 × 200 × 200 voxels) at various locations was studied, and the result is shown in Figure 4.9. It is shown that the local void ratio varies depending on the location in the compaction layer. Based on the separated and labeled sand grain results, image-based sieve analyses were performed on both Ottawa sand and Q-ROK sand specimens based on the sand grain volume, and the results are shown in Figure 4.10. The volume of a 700 μm diameter sphere is 0.180 mm^3. The water phase of the similar location to that of silica sand phase is also thresholded from neutron tomography data. The 3D visualization of the sand grain phase and the

water phase of the Ottawa sand specimen is shown in Figure 4.11. The thresholding of the water phase from the neutron tomography data is more complicated than that of the silica sand phase from X-ray tomography data. While the silica sand grains have much higher dimension (~700 μm) compared to the voxel size (11.2 μm) of the X-ray tomography image, the capillary films and bridges of the water phase can be much smaller than the resolution limit. The fixed spatial resolution (13.7 μm/pixel) of the neutron imaging detector cannot properly resolve the water films smaller than the resolution limit, and partial voxel effect can occur. Depending on the threshold value, the segmented volume of the water can vary significantly. The result shown in Figure 4.11 is based on the threshold found by factorization algorithm. The assessment of properness of the threshold value will be made by aligning the neutron and X-ray tomography data at the same location by using a method such as image registration.

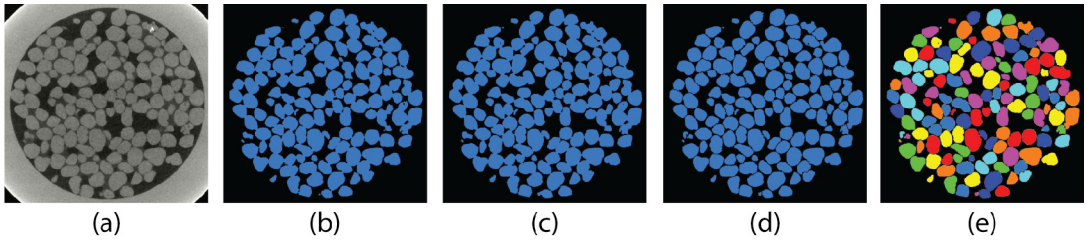


Figure 4.7: Image processing sequence applied to segment the sand grain phase: (a) 3D median filter applied image, (b) Thresholding result by factorization method on the region of interest, (c) Result after opening algorithm applied, (d) Result after 3D watershed algorithm applied, (e) Labeled (color coded) image of individual sand grains

Table 4.4: Void ratios obtained from phase relationship and tomography for Ottawa sand and Q-ROK sand

	Ottawa sand with water		Q-ROK sand with water	
	Obtained from phase relationship	Obtained from tomography	Obtained from phase relationship	Obtained from tomography
Void ratio	0.670	0.622	1.036	0.931

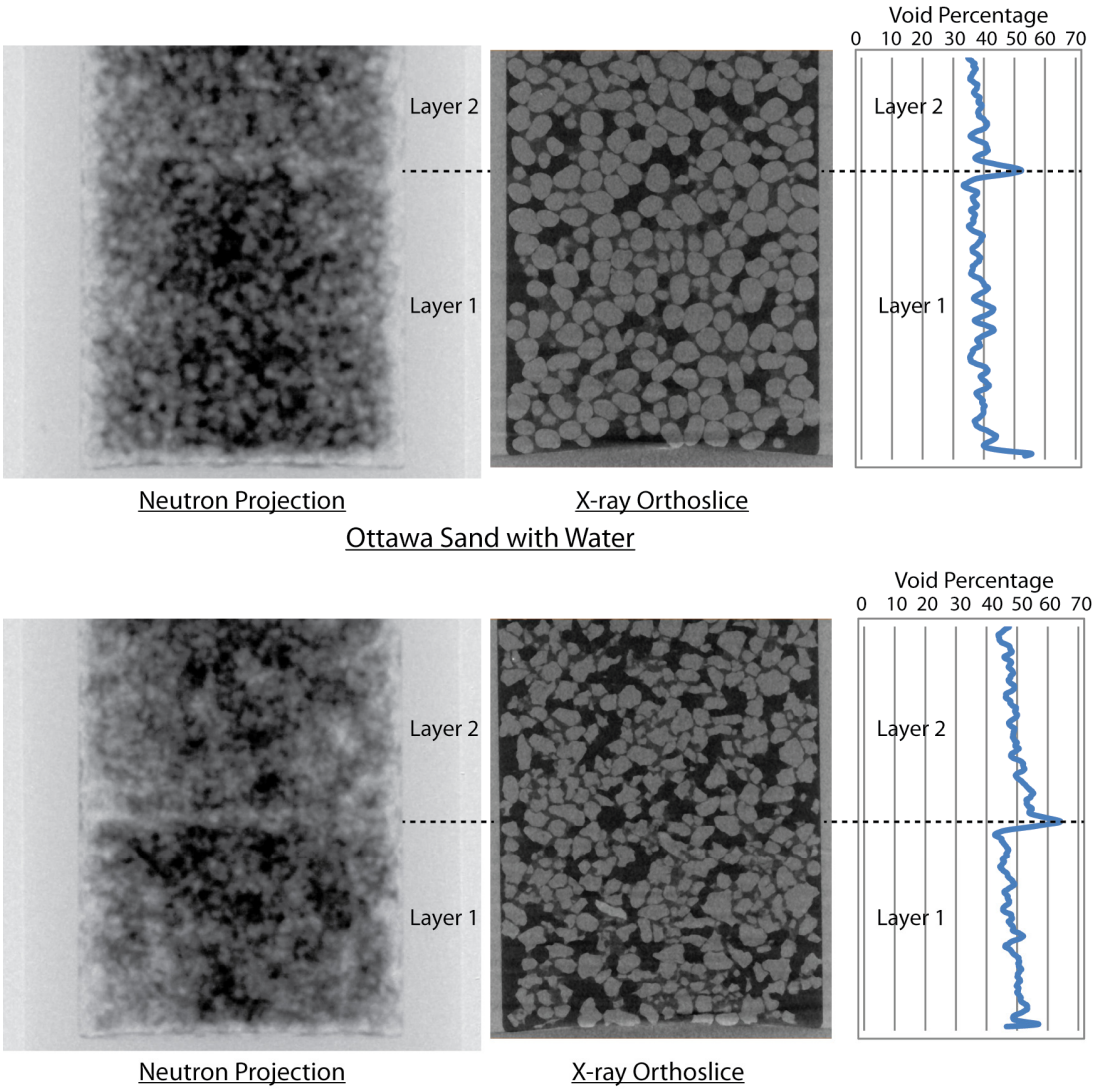


Figure 4.8: Void percentage over the height for Ottawa sand and Q-ROK sand

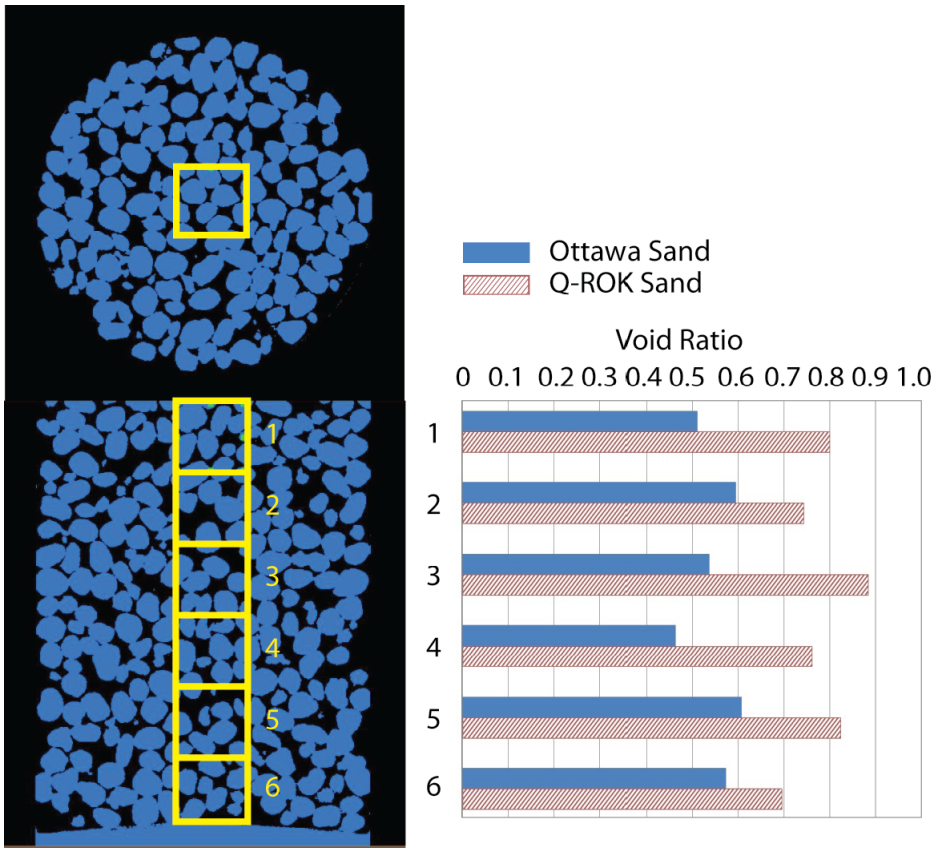


Figure 4.9: Local void ratio comparison of Ottawa sand and Q-ROK sand

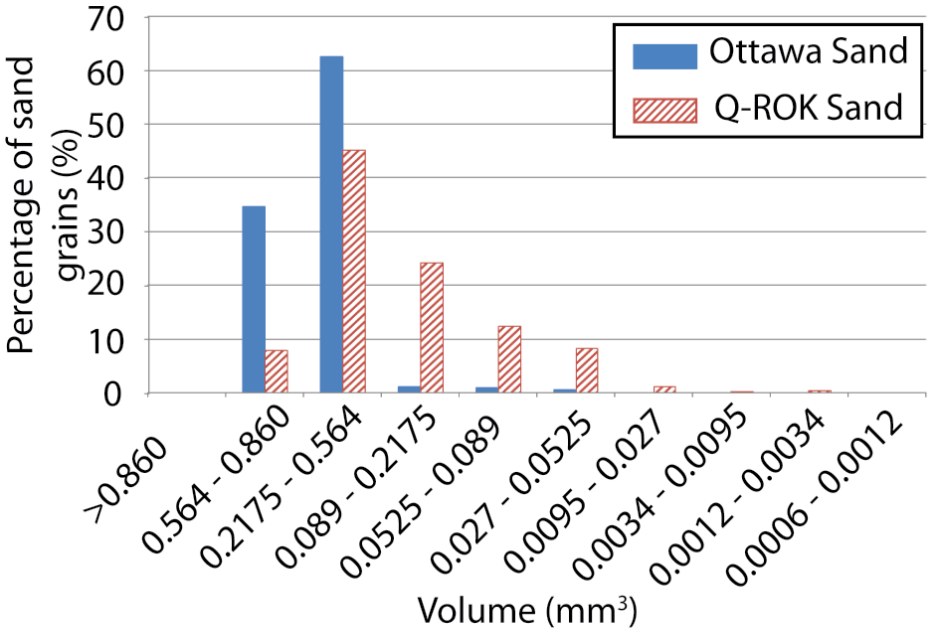


Figure 4.10: Grain size distribution based on sand grain volume obtained from the X-ray tomography data

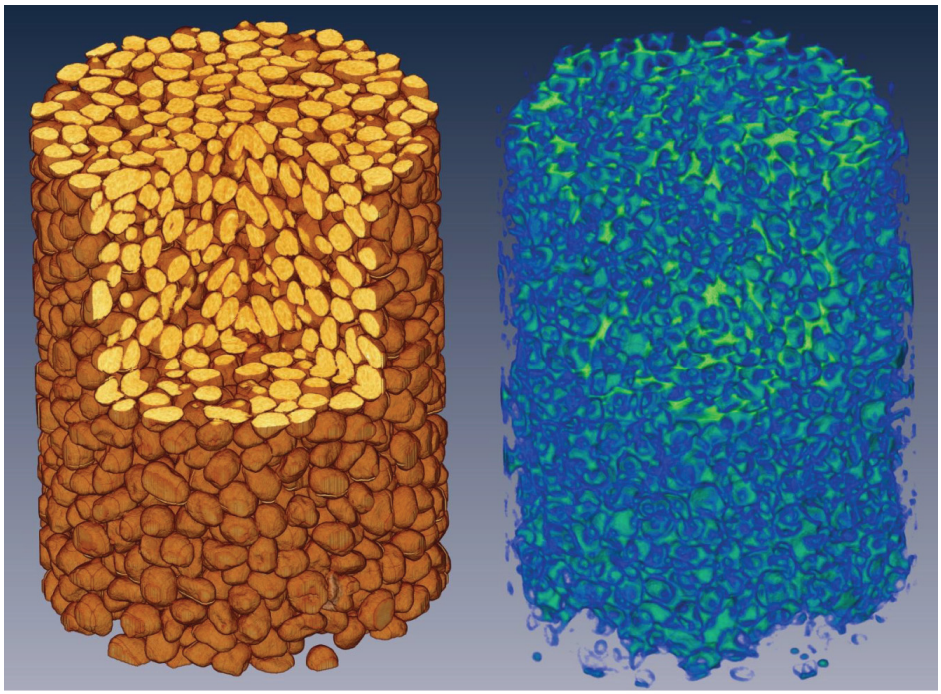


Figure 4.11: Visualization of the sand phase (a), and the water phase (b) in 3D

4.5 Conclusions

High resolution neutron tomography and microfocus X-ray tomography images of three wet silica sand specimens are presented in this paper. Neutron imaging technique is a relatively new imaging technique applied to the field of soil mechanics and geotechnical engineering. The recent development of high resolution capability has provided grain-level imaging of granular materials comparable to the microfocus X-ray tomography technique and promises a bright

future for studying geomaterials from the environment. The water distribution patterns of a compacted specimen and the relationship with grain shape are identified. The dual-modal contrast was demonstrated by the use of combined tomography data of neutrons and X-rays. Image analysis techniques are demonstrated on the tomography data to obtain geotechnical engineering parameters such as spatially resolved void ratio and particle size distribution.

4.6 References

Al-Raoush, R., and Alshibli, K. A. (2006). "Distribution of Local Void Ratio in Porous Media Systems from 3D X-ray Microtomography Images." *PHYSICA A*, 361(2), 441-456.

Al-Raoush, R. I., and Willson, C. S. (2005). "A pore-scale investigation of a multiphase porous media system." *Journal of Contaminant Hydrology*, 77(1-2), 67-89.

Auzerais, F. M., Dunsmuir, J., Ferréol, B. B., Martys, N., Olson, J., Ramakrishnan, T. S., Rothman, D. H., and Schwartz, L. M. (1996). "Transport in sandstone: A study based on three dimensional microtomography." *Geophys. Res. Lett.*, 23(7), 705-708.

Bardet, J. P., and Proubet, J. (1991). "A Numerical Investigation of the Structure of Persistent Shear Bands in Granular Media." *Géotechnique*, 41(4), 599-613.

Berkowitz, B., and Hansen, D. P. (2001). "A Numerical Study of the Distribution of Water in Partially Saturated Porous Rock." *Transport in Porous Media*, 45, 303-319.

Buzug, T. M. (2008). *Computed Tomogrpahy From Photon Statistics to Modern Cone-Beam CT*, Springer, Verlag Berlin Heidelberg.

Carminati, A., Kaestner, A., Ippisch, O., Koliji, A., Lehmann, P., Hassanein, R., Vontobel, P., Lehmann, E., Laloui, L., Vulliet, L., and Flühler, H. (2007). "Water flow between soil aggregates." *Transport in Porous Media*, 68(2), 219-236.

Cundall, P. A., and Strack, O. D. L. (1979). "A discrete numerical model for granular assemblies." *Géotechnique*, 29(1), 47-65.

de Beer, F. C., and Middleton, M. F. (2006). "Neutron Radiography Imaging, Porosity and Permeability in Porous Rocks." *South African Journal of Geology*, 109(4), 541-550.

Desrues, J., Chambon, R., Mokni, M., and Mazerolle, F. (1996). "Void ratio evolution inside shear bands in triaxial sand specimens studied by computed tomography." *Géotechnique*, 46(3), 529-546.

Ferréol, B., and Rothman, D. H. (1995). "Lattice-Boltzmann simulations of flow through Fontainebleau sandstone." *Transport in Porous Media*, 20(1), 3-20.

Holtz, R. D., and Kovacs, W. D. (1981). *An Introduction to Geotechnical Engineering*, Prentice Hall, Englewood Cliffs, NJ

Ishakoglu, A., and Baytas, A. F. (2005). "The influence of contact angle on capillary pressure-saturation relations in a porous medium including various liquids." *International Journal of Engineering Science*, 43(8-9), 744-755.

Iwashita, K., and Oda, M. (1998). "Rolling Resistance at Contacts in Simulation of Shear Band Development by DEM." *Journal of Engineering Mechanics*, 124(3), 285-292.

Kak, A. C., and Slaney, M. (2001). *Principles of Computerized Tomographic Imaging*, Society for Industrial and Applied Mathematics, Philadelphia, PA.

Kardjilov, N., Dawson, M., Hilger, A., Manke, I., Strobl, M., Penumadu, D., Kim, F. H., Garcia-Moreno, F., and Banhart, J. (2011). "A Highly Adaptive Detector System for High Resolution Neutron Imaging." *Nuclear Instruments and Methods in Physics Research Section A: Accelerators, Spectrometers, Detectors and Associated Equipment*, 651(1), 95-99.

Kardjilov, N., Hilger, A., Manke, I., Strobl, M., Dawson, M., and Banhart, J. (2009). "New trends in neutron imaging." *Nuclear Instruments and Methods in Physics Research Section A: Accelerators, Spectrometers, Detectors and Associated Equipment*, 605(1-2), 13-15.

Kim, F. H., Penumadu, D., and Hussey, D. S. (2012). "Water Distribution Variation in Partially Saturated Granular Materials Using Neutron Imaging." *Journal of Geotechnical and Geoenvironmental Engineering, American Society of Civil Engineers (ASCE)*, 138(2), 147-154.

Lambe, T. W., and Whitman, R. V. (1969). *Soil Mechanics*, John Wiley & Sons.

Lewis, J. T., and Krinitzsky, E. L. (1976). "Neutron Radiation in the Study of Soil and Rock." Practical Applications of Neutron Radiography and Gaging, H. Berger, ed., American Society for Testing and Materials, Baltimore, Md, 241-251.

Li, X. S., and Dafalias, Y. F. (2012). "Anisotropic Critical State Theory: Role of Fabric." *Journal of Engineering Mechanics*, 138(3), 263-275.

Lopes, R. T., Bessa, A. P., Braz, D., and de Jesus, E. F. O. (1999). "Neutron computerized tomography in compacted soil." *Applied Radiation and Isotopes*, 50(2), 451-458.

McCullough, E. C. (1975). "Photon attenuation in computed tomography." *Medical Physics*, 2(6), 307-320.

Milczarek, J. J., Czachor, A., Abd El-Ghany, E. A., and Wisniewski, Z. (2005). "Dynamic Neutron Radiography Observations of Water Migration in Porous Media." *Nuclear Instruments and Methods in Physics Research Section A: Accelerators, Spectrometers, Detectors and Associated Equipment*, 542(1-3), 232-236.

Muhunthan, B., and Chameau, J. L. (1997). "Void Fabric Tensor and Ultimate State Surface of Soils." *Journal of Geotechnical and Geoenvironmental Engineering*, 123(2), 173-181.

Oda, M. (1972a). "Initial Fabrics and Their Relations to Mechanical Properties of Granular Material." *Soils and Foundations*, 12(1), 17-36.

Oda, M. (1972b). "The Mechanism of Fabric Changes During Compressional Deformation of Sand." *Soils and Foundations*, 12(2), 1-18.

Oda, M. (1972c). "Deformation Mechanism of Sand in Triaxial Compression Tests." *Soils and Foundations*, 12(4), 45-63.
Otani, J. (2010). "X-ray Computed Tomography for Geotechnical Engineering." Advances in X-ray Tomography for Geomaterials, J. Desrues, C. Viggiani, and P. Bésuelle, eds., ISTE Ltd, London, UK, 95-115.
Otsu, N. (1979). "A threshold selection method from gray-level histograms." *IEEE Transactions on Systems, Man, and Cybernetics* SMC-9(1), 62-66.
Peters, J. F. (2005). "Some fundamental aspects of the continuumization problem in granular media." *Journal of Engineering Mathematics*, 52(1), 231-250.
Pleinert, H., and Degueldre, C. (1995). "Neutron radiographic measurement of porosity of crystalline rock samples: a feasibility study." *Journal of Contaminant Hydrology*, 19(1), 29-46.
Razavi, M. R., Muhunthan, B., and Al Hattamleh, O. (2007). "Representative elementary volume analysis of sands using X-ray computed tomography." *ASTM Geotechnical Testing Journal*, 30(3), 212-219.
Scheel, M., Seemann, R., Brinkmann, M., Di Michiel, M., Sheppard, A., Breidenbach, B., and Herminghaus, S. (2008). "Morphological clues to wet granular pile stability." *Nat Mater*, 7(3), 189-193.
Schiffer, P. (2005). "Granular physics: A bridge to sandpile stability." *Nat Phys*, 1(1), 21-22.
Schnaar, G., and Brusseau, M. L. (2005). "Pore-Scale Characterization of Organic Immiscible-Liquid Morphology in Natural Porous Media Using Synchrotron X-ray Microtomography." *Environmental Science & Technology*, 39(21), 8403-8410.
Sham, T. K., and Rivers, M. L. (2002). "A Brief Overview of Synchrotron Radiation." *Reviews in Mineralogy and Geochemistry*, 49(1), 117-147.
Silin, D., Tomutsa, L., Benson, S., and Patzek, T. (2011). "Microtomography and Pore-Scale Modeling of Two-Phase Fluid Distribution." *Transport in Porous Media*, 86(2), 495-515.
Sutton, S. R., Bertsch, P. M., Newville, M., Rivers, M., Lanzirotti, A., and Eng, P. (2002). "Microfluorescence and Microtomography Analyses of Heterogeneous Earth and Environmental Materials." *Reviews in Mineralogy and Geochemistry*, 49(1), 429-483.
Tobin, K. W., Bingham, P. R., and Gregor, J. (2009). "Mathematics of Neutron Imaging." Neutron Imaging and Applications, I. S. Anderson, McGreevy, R.L., Bilheux, H.Z., ed., Springer Science+Business Media, LLC New York, NY, 109-127.
Tullis, B. P., Lindsay, J. T., and Wright, S. J. (1994). "The Imaging of Wetting Front Instabilities in Porous Media Using Neutron Radioscopy." *Nondestr. Test. Eval.*, 11(2-3), 97-106.

Wang, L. B., Frost, J. D., and Lai, J. S. (2004). "Three-Dimensional Digital Representation of Granular Material Microstructure from X-Ray Tomography Imaging." *Journal of Computing in Civil Engineering*, 18(1), 28-35.

Wellington, S. L., and Vinegar, H. J. (1987). "X-Ray Computerized Tomography." *Journal of Petroleum Technology*, 39(8), 885-898.

Wildenschild, D., Hopmans, J. W., Rivers, M. L., and Kent, A. J. R. (2005). "Quantitative Analysis of Flow Processes in a Sand Using Synchrotron-Based X-ray Microtomography." *Vadose Zone Journal*, 4(1), 112-126.

Wildenschild, D., Vaz, C. M. P., Rivers, M. L., Rikard, D., and Christensen, B. S. B. (2002). "Using X-ray computed tomography in hydrology: systems, resolutions, and limitations." *Journal of Hydrology*, 267(3-4), 285-297.

Yang, X. (2005). "Three-Dimensional Characterization of Inherent and Induced Sand Microstructure," Gerogia Institute of Technology.

Yimsiri, S., and Soga, K. (2010). "DEM analysis of soil fabric effects on behaviour of sand." *Géotechnique*, 60(6), 483-495.

CHAPTER 5. IMAGE REGISTRATION OF DUAL MODALITY DATA

This chapter is revised based on a paper submitted by Felix Kim, Dayakar Penumadu et al. :

Kim, F. H., Penumadu, D., Gregor, J., Marsh, M., Kardjilov, N. and Manke, I. (2013). Image Registration of High Resolution Neutron and X-ray Tomography of Partially Saturated Compacted Sand Specimens. Paper in preparation.

My primary contributions to the paper included: (i) understanding image registration technique based on maximization of mutual information, (ii) gathering and reviewing literature, (iii) understanding image registration metric, (iv) processing, analyzing, and interpretation of the experimental data, (v) most of the writing.

5.1 Abstract

Three dimensional (3D) image registration of dual modality (neutron and X-ray) tomography data of partially saturated sand specimens is presented. Neutron and X-ray imaging provide complementary contrast for precisely identifying the three phases (silica sand, air, and water) of a compacted sand specimen that is partially saturated. Neutron tomography provides high contrast of the water phase while X-ray tomography provides high contrast of the silica sand and voids phases. In this paper, a procedure was developed to integrate the dual modality data obtained at different resolutions and specimen orientations based on the maximization of the normalized mutual information. A more complete structure of the three phase system can thus be obtained by combining the two modalities. Microstructure information for granular assembly including pore size distribution and coordination number was determined from X-ray tomography data due to higher precision in identifying solid particle boundaries. Local values of saturation along the height of the specimen are obtained from the registered pore and water phases from dual neutron and photon attenuation contrast.

5.2 Introduction

The deformation mechanics of partially saturated soil and transport of flow through partially saturated porous media are complex and unresolved problems.

The interaction between the solid, gas and liquid phases in a porous granular material is very complex as it involves sliding and rolling of discrete solid particles and interaction of voids and capillary bridges. The microstructure of the granular system is defined as the combination of fabric, composition, and interparticle forces (Mitchell and Soga 2005). The visualization and quantification of the microstructure of the three phases at a grain/pore level will significantly enhance the understanding of mechanics and fluid physics of partially saturated granular materials.

In order to study mechanical and/or transport properties of soil/porous media at a grain/pore scale, several different imaging techniques including optical microscopy, electron microscopy, X-ray radiography/tomography, and neutron radiography/tomography have been used (Al-Raoush and Alshibli 2006; Andò et al. 2012; Kim et al. 2012; Muhunthan and Chameau 1997; Oda 1972a; Oda 1972b; Oda 1972c; Yang 2005). Segmentation of the three phases (silica, air and water) is critical for quantitative analysis. Recently, an advanced thresholding algorithm was tried to separate the three phases from X-ray tomography data (Kaddhour et al. 2013). Due to the different interaction mechanisms, each imaging technique often shows different features of the same object with better contrast or visualization. Dual-modal contrasts of X-ray and neutron on the images are reported on various samples and objects (Christe et al. 2007; Manke et al. 2011; Matsushima et al. 2009; Winkler 2006; Winkler et al.

2002). Recently, high resolution neutron and X-ray imaging results of partially saturated compacted sand specimens taken at Helmholtz-Zentrum-Berlin (HZB) were presented at meso-scale (grain level) by the authors (Kim et al. 2013a). The neutron images provided good contrast for identifying the water phase, but the air and silica sand phases were not distinguished clearly. On the other hand, X-ray images provided better contrast for the silica sand phase compared to the water and air phases. The result is due to the different contrast mechanisms of neutrons and X-ray. Neutron tomography can provide clear information of the water phase, and X-ray tomography can provide clear information of the silica phase. Since the two tomography data sets are taken at different spatial resolutions and specimen orientations with varying modality, these data need to be properly homogenized and resolved at similar orientations for a complete analysis of the microstructure. Manual identification and correspondence of the two images is fairly difficult and time consuming for registration. It is thus necessary to use an automatic method with a proper measure of alignment to integrate two modalities (X-ray and neutron) obtained at varying resolutions and orientations.

In medical imaging, different imaging modalities are often used to visualize different parts of a body, and various registration methods have been developed to combine the multimodal data (Maintz and Viergever 1998). Magnetic resonance imaging (MRI) or X-ray computed tomography (CT) is used to obtain

the structural anatomical information of the body. Positron emission tomography (PET) or single photon emission computed tomography (SPECT) imaging is used to provide functional information of metabolism of the underlying body. The combined information from registered images helps with understanding of the condition of patient and the planning of surgery. Recently, the multimodal image registration technique is also being used in general science fields for improved visualization and quantification of the objects of interest. Image registration of SEM and X-ray images was performed to investigate the mineral composition information combined with structural information (Kumar et al. 2010; Latham et al. 2008). A limited portion of the sample was used to obtain SEM images due to small field of view (FOV) achievable at a relevant magnification. Registration of neutron and X-ray tomography data of an artificially made objects presenting multi-modality was performed for future application to investigate historical objects of value to measures (Kudejova et al. 2007). Release of water in the cement paste was visualized by a registration of neutron tomographies taken at different time while using X-ray tomography to define the boundaries of the light weight aggregate and cement paste recently (Trtik et al. 2011).

The authors implemented an advanced image registration algorithm for studying high resolution neutron and X-ray tomography images of a compacted partially saturated sand specimen in this study. Registration of neutron and X-ray images of partially saturated sand is performed for the first time at a resolution of

grain scale. Neutron tomography data provides high contrast for the water phase without using a contrast agent while X-ray tomography data provides high contrast of the silica sand phase. The neutron and X-ray tomography data were aligned in three dimensions by using an image registration technique based on maximization of normalized mutual information. Basic explanation of normalized mutual information and image registration process is provided. The complete structure of the three phase system can be studied by combining the fabric information obtained from X-ray tomography data and interparticle water capillary bridges obtained from neutron tomography data. Fabric information such as pore size distribution and coordination number was computed. The degrees of saturation values (volume of water to volume of voids) along the height of the specimen were also calculated from the combined data to evaluate its spatial variation. Representative elementary volume (REV) analysis for porosity and saturation was performed for the compacted partially saturated sand specimens. The image registration technique of dual modality imaging presented in this paper for geo-materials can be extended to study more complex experiments involving in-situ fluid flow and solid deformation, and it is the current direction of the authors' research. The experimental imaging results can be applied for direct validation of numerical simulation results obtained from direct numerical simulation techniques where the actual microstructure can be used to account for

the heterogeneity of porous media structure (Ferréol and Rothman 1995; Hazlett 1995; Kim et al. 2013b; Spanne et al. 1994).

5.3 Specimen Descriptions

The complete details of specimen preparation and imaging are described in a recent paper by the authors (Kim et al. 2013a). Compacted partially saturated silica sand specimens were placed in custom developed aluminum cylinders with 10 mm diameters, 23 mm height and 2 mm wall thickness. The silica sand was mixed with either deionized water (H_2O) or heavy water (D_2O) at target gravimetric water content of 12%. The wet sand was placed in the aluminum specimen holder with three compaction layers and a neutron radiograph of the sand specimen in aluminum holder shown in Figure 5.1. The compaction procedure includes filling 1/3rd of the volume of the specimen holder with sand at target water content and compacted by tamping a rod 25 times for each for three layers. Two types of sand with different particle shape of sand were used: round (Ottawa sand) and angular (Q-ROK sand). The average diameters of both sands are approximately 600-700 μm based on sieve analysis. Mineralogically, Ottawa sand and Q-ROK sand were composed of 99.8% and 99.7% SiO_2 respectively. The region of interest (ROI) used for image registration and analysis is also indicated in Figure 5.1. Due to the computational memory limit, bottom half of each specimen was used for registration and analysis.

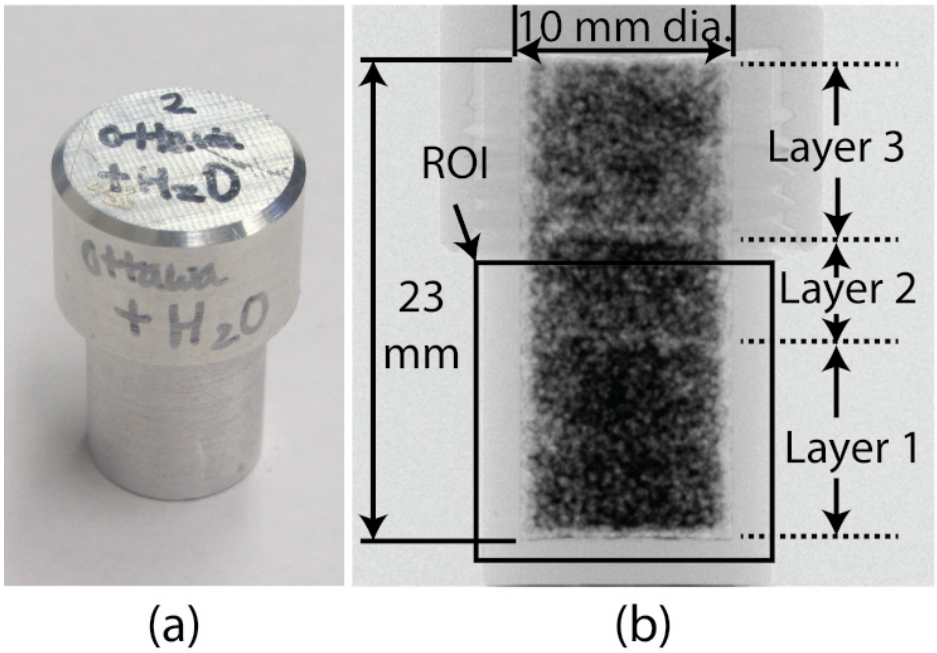


Figure 5.1: Picture of a specimen (a) and neutron radiograph (b) showing specimen description, compaction layer and region of interest

The neutron or X-ray images of these specimens show three-phase systems composed of solid (sand), gas (air) and liquid (water or heavy water) phases. X-rays and neutrons have different interaction mechanisms with materials. X-rays mainly interact with the electron clouds of an atom while neutrons mainly interact with the nucleus of an atom, and the different interaction mechanism results in different contrasts on images. Depending on the material composition, X-ray and neutron images can provide different but complementary contrasts.

The histogram of X-ray data is shown in Figure 5.2. The data is already smoothened by applying a 3D median filter. The peaks of water and air phases in the histogram are merged, and a clear segmentation between the two phases cannot be performed simply. There is inherent noise in the image due to acquisition and reconstruction processes, and it resulted in widening the distribution around the histogram peaks. Due to the relatively high energy of X-ray (100 kV) and the hardening effect of the X-ray energy spectrum after passing through highly attenuating aluminum wall, the attenuation coefficient of the water phase become very close to that of the air phase. As the peaks of air and water phases become too close to each other, it is difficult to separate the two phases in the X-ray data. As a result, neutron tomography data of the same specimen is explored for segmentation of water phase to complement the X-ray data.

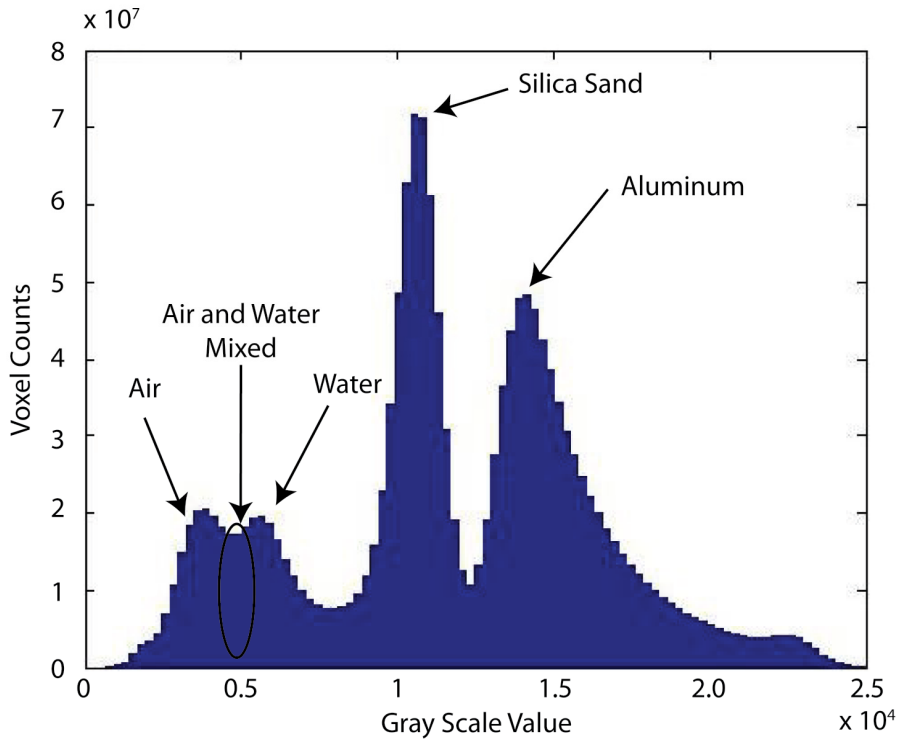


Figure 5.2: Histogram of the X-ray data after median filter (5×5×5) is applied

5.4 Image Registration Based on Maximization of Normalized Mutual Information

5.4.1 Background

Image registration is a task of geometrically aligning two or more images of the same scene that are taken at different times, from different viewpoints, and/or by different sensors (Zitová and Flusser 2003). The registration of images taken from two different sensors (neutron and X-ray tomography) is performed in

this project. Different imaging sensors or modalities can provide different contrasts on some materials within the sample. In order to relate the different microstructural features of interest provided by different modalities, the images need to be aligned in a common coordinate system. Images obtained from multi-modalities have both common and complementary structures within the images. Any shared regions from the two modalities need to be used to align the two images. In this project, normalized mutual information based automatic registration method was used, and a brief overview is provided here. A more comprehensive perspective on image registration is reported by other researchers (Brown 1992; Maintz and Viergever 1998; Pluim et al. 2003).

For automatic alignment of two images, a certain measure to determine the state of registration is required. Measures based on entropy are often used for image registration. Entropy is a measure of information or uncertainty used originally in the field of information theory. Entropy can also be viewed as a measure of uncertainty. Shannon entropy (*H*) is one of the most commonly used ones, and it is shown in equation 5.1 where *p* is the probability distribution function (Shannon 1948). Different definitions of entropy is also available (Esteban and Morales 1995).

$$H = \sum_i p_i \log \frac{1}{p_i} \qquad 5.1$$

The entropy can be computed for an image by using the gray value distribution of the image (histogram). The histogram can be normalized to be

used as the probability distribution function (*p*). Low entropy means low information (uncertainty), and high entropy means high information (uncertainty).

Three different types of entropies between image A and B are classified as shown in Figure 5.3. *H*(*A*) and *H*(*B*) are marginal entropies of A and B respectively, and *H*(*A*,*B*) is the joint entropy of A and B. The cross section of *H*(*A*) and *H*(*B*) are the mutual information *I*(*A*;*B*). The mutual information is the difference between joint entropy and the sum of the marginal entropies, and can be expressed as shown in equation 5.2.

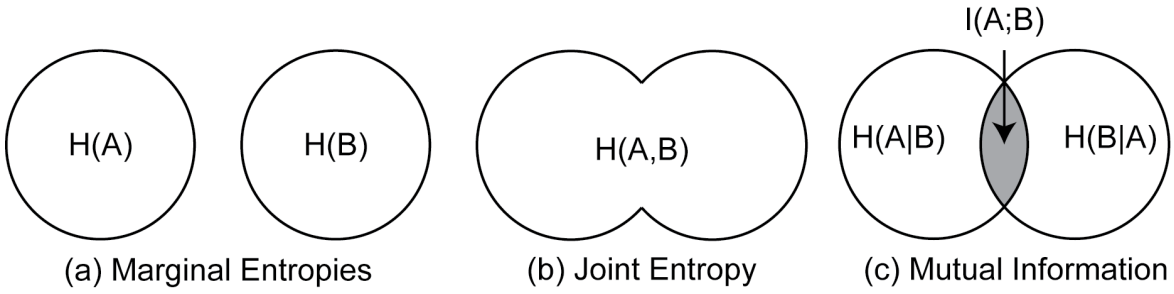


Figure 5.3: Definitions of marginal entropy, joint entropy and mutual information by using Venn diagrams

$$I(A,B) = H(A) + H(B) - H(A,B) \qquad 5.2$$

The minimization of joint entropy as the criterion for image registration was used initially for image registration research, but it was found that it is not so effective when the background area is large (Pluim et al. 2003; Studholme et al.

1999). Instead, maximization of the mutual information was utilized (Collignon et al. 1995; Viola and Wells 1995). The two images are optimally matched when their mutual information is maximized. The minimization of H(A,B) and maximization of I(A,B) are not exactly the same since the marginal entropies H(A) and/or H(B) varies throughout the transformation.

The normalized mutual information based registration has shown to be more effective due to lower sensitivity to changes in overlap between the two images during rigid body transformation (Studholme et al. 1999). The definition of normalized mutual information (*Y*) is shown in equation 5.3.

$$Y(A,B) = \frac{H(A) + H(B)}{H(A,B)} \qquad 5.3$$

During the registration process, one image will be rotated/translated/scaled incrementally compared to the other image. The normalized mutual information of the two images will be computed at each increment. The transformation at which the maximum normalized mutual information was achieved will be determined as the most closely registered state.

5.4.2 Process

The dual modality imaging at HZB required physical relocation of the specimens from the neutron imaging system to the X-ray imaging system. The process can change the specimen orientation, and the process has a possibility of disturbing the specimens even though the moving distance was short. The

calibration of image pixel resolution is not perfect, and this results with discrepancy with the physical size of the object between two different imaging systems. Manual registration of the two data is not only a tedious job, but also almost impossible at a finer level due to the large number of sand grains and the complex geometry of water capillary bridge involved. Automatic registration process based on maximization of normalized mutual information was performed within the environment of Avizo®.

Some preprocessing on the original data was performed for smoother application of the automatic registration technique. X-ray tomography data was smoothed with 3D median filter (5×5×5). The X-ray tomography data had about 11.2 μm pixel size and the neutron tomography data had about 13.7 μm pixel size. The lower resolution neutron tomography data was resampled (upsampled) to the same voxel size as X-ray tomography data by using Lanczos filter.

The neutron data was chosen as the moving volume and X-ray data as the reference volume. The moving volume is translated/rotated/scaled with respect to the reference volume to align them in the same place. Rough manual rotation and translation of the moving volume was performed before applying the automatic registration by maximizing the normalized mutual information of the two volumes. The rigid body transformation (translation and rotation) was performed first, and then isotropic scaling was performed to take any minor voxel size calibration differences into account.

Multi-resolution approach was used in order to reduce the computational time involved and reduce local maxima effect, and Quasi Newton method was used as the optimizing strategy (Maes et al. 1999). The original image is sub-sampled to lower resolution data of various sizes, and registration was fine-tuned from the coarser resolution data to finer resolution data incrementally.

5.4.3 Results

The final results of registration are presented in Figure 5.4 with the tomography slices and Figure 5.5 in 3D by super-positioning the neutron and X-ray data in the same image. The registered image shows the sand grain phase from X-ray tomography data, and the water phase from neutron tomography data after proper rescaling of the intensity. Water and heavy water has different attenuation coefficient, and a different colormap rescaling value was used for better visualization in Figure 5.5.

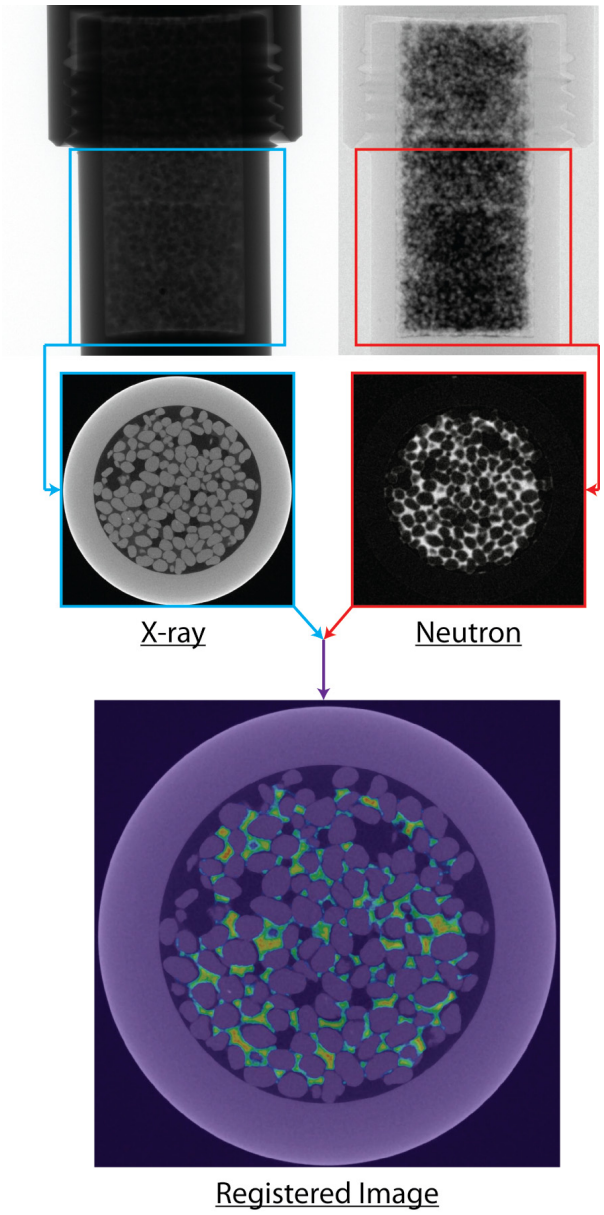


Figure 5.4: Illustration of registration process and result with super-positioned image of neutron and X-ray tomography slice

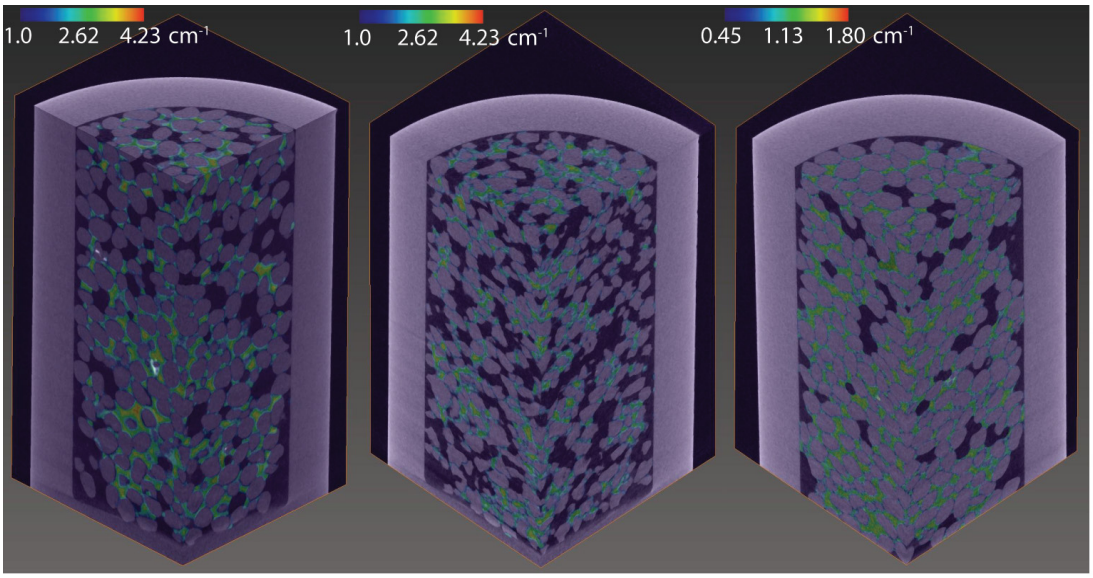


Figure 5.5: Three dimensional super-positioned views neutron and X-ray tomography data of the three specimens after image registrations are performed

An illustrative example of computing mutual information at different angular rotation of registered state of neutron and X-ray tomography slices was performed to verify the result and illustrate the registration process as shown in Figure 5.6 Marginal entropies and joint entropy at different angular rotation was calculated. Mutual information and normalized mutual information were calculated. The two images are exactly the same size. Some artifacts or patterns are expected due to bilinear interpolation process (Pluim et al. 2000; Tsao 2003). Due to transformation of neutron image, marginal entropy of neutron image

changes and the joint entropy also changes. Shannon's entropy was used to compute the entropies. The minimum value of joint entropy was not at 0° degree angle, but the mutual information is maximum at 0° angle. This shows the effectiveness of maximization of mutual information, and confirms that the registration process is working properly. Similar procedures were performed during the registration process in 3D for translation, rotation, and isotropic scaling to find the optimum state of registration.

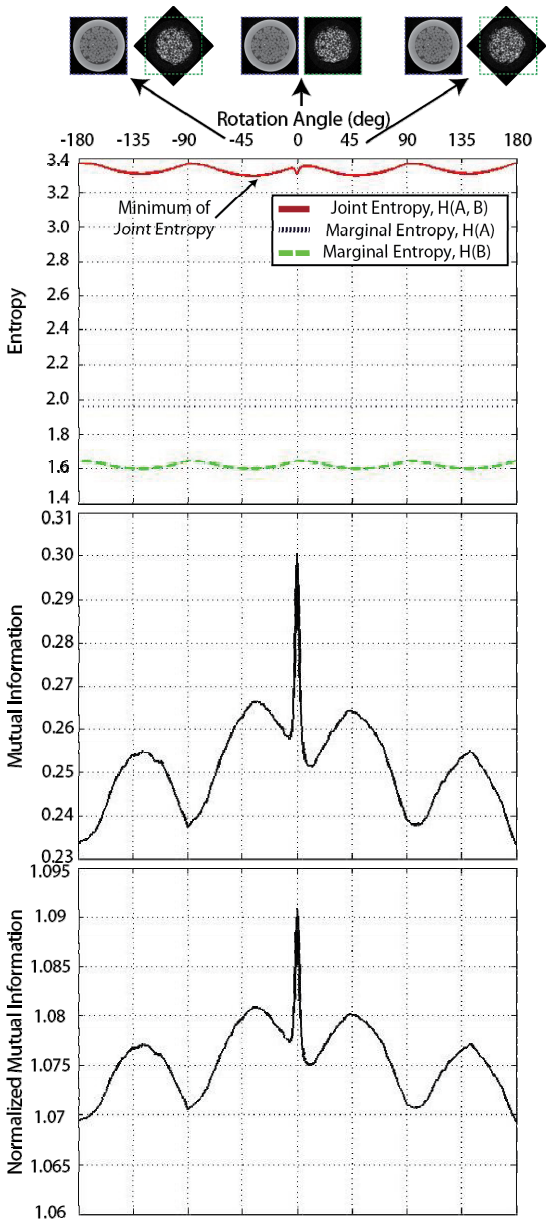


Figure 5.6: Illustrative example of registration process and verification of the result by computing marginal entropies, mutual information and normalized mutual information for different angles of rotation

5.5 Analyses

5.5.1 Image Segmentation

Based on the registered data, more accurate phase quantification is performed by applying proper image processing and segmentation procedures. Image segmentation is a process of subdividing an image into its constituent regions or objects some of which includes thresholding and region splitting/merging (Gonzalez and Woods 2008). X-ray image segmentation of silica sand grain phase is performed with a relatively high accuracy due to a close-to-uniform sand grain distribution with approximately 700 μm diameter of Ottawa and Q-ROK sand compared to the voxel size (~11.2 μm). On the other hand, the segmentation of neutron image is not straight forward due to the varying size of water films and bridges. The size of the water capillary films and bridges vary from submicron to mm level, and the limited spatial resolution of the system was not able to capture the water phase below the neutron image resolution limit properly. As a result, some blurring and partial volume effect is observed at the edge and boundaries. Partial volume effect occurs when a feature is smaller than resolution limit or at the edge of a feature, and the change in attenuation is blurred. Additionally, neutron tomography was taken with a lower spatial resolution compared to X-ray tomography, and partial voxel effect of water phase is more pronounced at the sand grain and water phase boundary in the registered images. More accurate segmentation of the water phase was

achieved by utilizing thresholded sand grain boundaries obtained from the registered X-ray data in addition to thresholded water phase data obtained from the neutron data. The over segmented region of neutron data due to blurring and partial volume effects can be removed by comparing with the X-ray data. The interface between sand grain boundary and water phase is subtracted from the water phase more easily due to the close registration of the dual modality data. The segmentation process and results are illustrated in Figure 5.7.

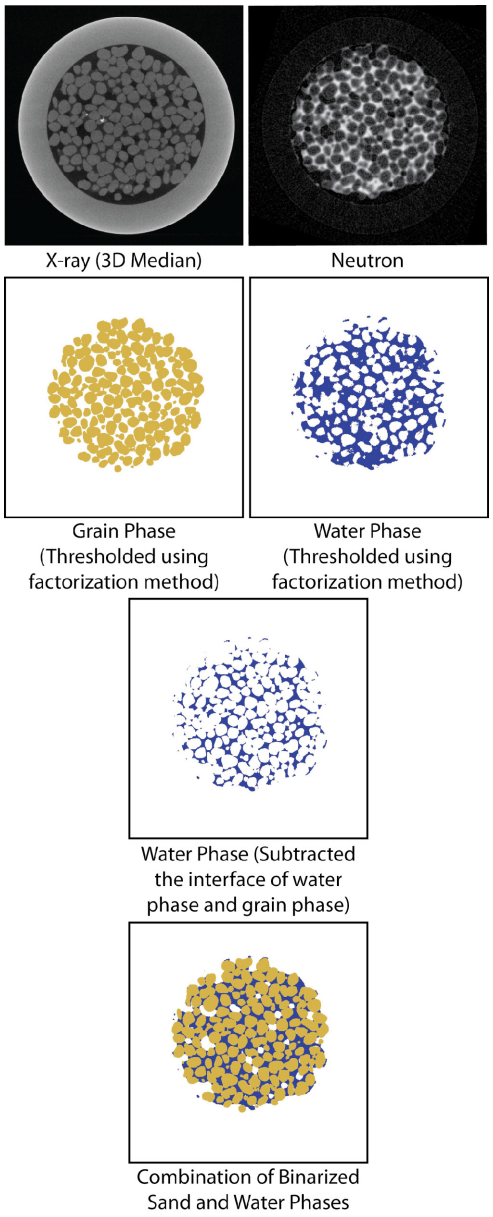


Figure 5.7: Process to segment water phases more accurately by using registered X-ray and neutron data

5.5.2 Saturation Profile

Analysis of the water volume, pore volume and saturation values along the height of the specimen is performed as shown in Figure 5.8. Close attention was given to the compaction layers of the specimen, and the location of the compaction layer interface is more easily identified with the colorized neutron projection image. Orthoslice is a cross sectional image with a thickness of 1 pixel interior of the specimen. It is often shown in the three orthogonal planes (x-y, y-z and x-z planes). Projection image shows an integrated attenuation at a projected plane. The neutron projection view revealed the compaction layers more clearly due to high attenuation of neutron for water phase while it is difficult to interpret the compaction layer from neutron and X-ray orthoslices. Bottom half of the specimen volumes that cover part of compaction layer 2 and full compaction layer 3 are used for the analysis as already explained earlier and illustrated in Figure 5.1. The water volume is calculated from segmented neutron tomography data, and the pore volume is calculated from segmented X-ray tomography data. As evidenced from neutron projection image, there is a sudden change of water volume at the interface of compaction layers. Q-ROK sand has much higher pore volume than that of Ottawa sand with similar water volumes. As a result, Ottawa sand has higher saturation value than Q-ROK sand in general. It shows higher pore volume and lower water volume at the interface between compaction layers, and low saturation value was obtained at the interface. Similar specimens were

visualized from neutron radiography and tomography at a much coarser resolution (127 μm/voxel), and a difference with the complex distribution of water for Ottawa sand and Q-ROK sand was observed (Kim et al. 2012). In the current data, similar distribution pattern is shown. The water volume is almost constant along the height of the compaction layer for Ottawa sand while the water volume decreased toward the bottom for the compaction layer for Q-ROK sand. It indicates that the sand grain shape affects the capillary water distribution and imaging techniques reported in this paper will be very useful for such studies.

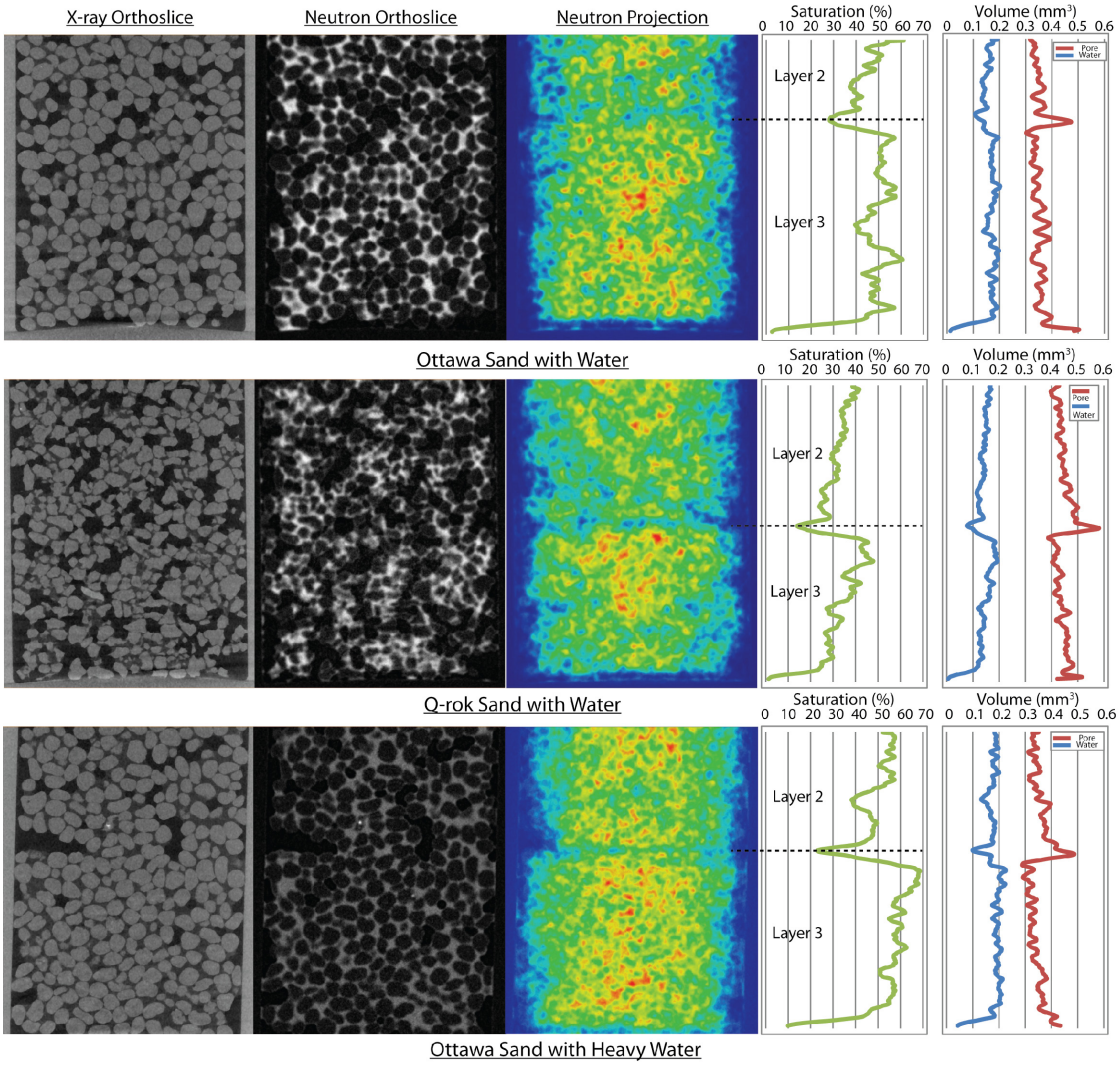


Figure 5.8: Pore volume, water volume and saturation over the height of the specimen

5.5.3 Pore Size Distribution and Coordination Number

Fabric of the partially saturated sand is represented by the pore size distribution and coordination number obtained from the segmented X-ray tomography data. Pore size distribution is found from the pore phase of the X-ray tomography data and the coordination number is found from the grain phase of the X-ray tomography data. Pore phase is essentially the inverse image of the grain phase.

Geometric pore size distribution was found by using GeoDict software (www.geodict.com). The morphological opening with spheres of increasing radius is employed to determine the pore size distribution based on granulometry (Becker et al. 2007; Soille 1999). The results of both Ottawa sand with water and Q-ROK sand with water specimens are shown in Figure 5.9.

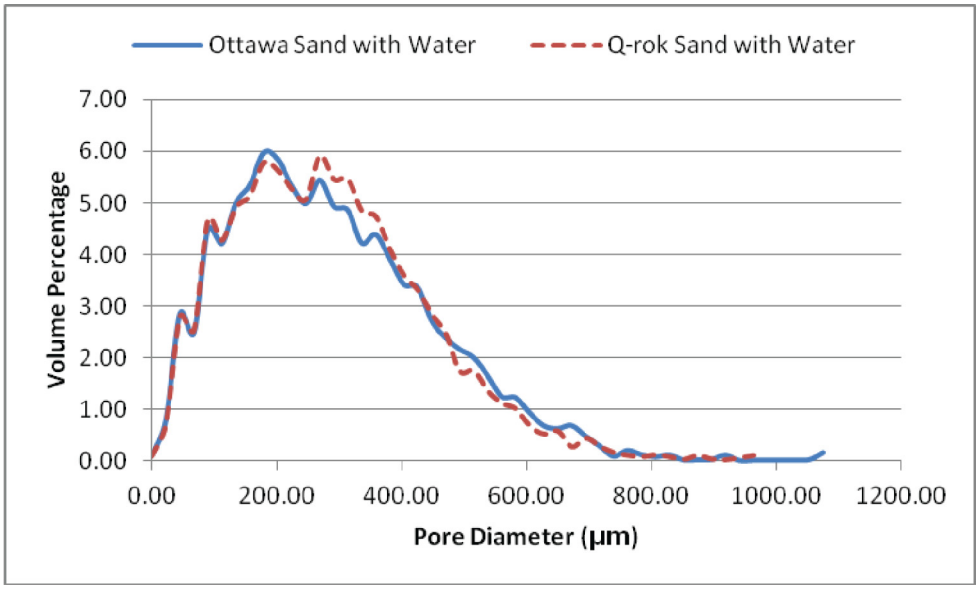


Figure 5.9: Pore size distribution for Ottawa sand with water and Q-ROK sand with water specimens

The coordination number was calculated based on the watershed separated grains results for both Ottawa sand and Q-ROK sand. The procedure for watershed separation is illustrated in earlier paper (Kim et al. 2013a). Before the watershed segmentation algorithm was applied, the X-ray tomography data was further smoothened with non-local mean filter for much clearer thresholding aiding in better separation of sand grains with watershed algorithm (Buades et al. 2005). The contact points are found based on the watershed separation lines and the number of grains in contact is found for coordination number. The results for Ottawa sand with water and Q-ROK sand with water specimens are shown in

Figure 5.10. The average coordination number is 7.8 for Ottawa sand and 6.7 for Q-ROK sand. Based on the Gaussian distribution, the mean coordination number for Ottawa sand is 8.0 and for Q-ROK sand is 6.3. The angular Q-ROK sand found to have lower mean coordination number compared to rounded Ottawa sand. Some outliers are expected as the watershed separation algorithm is not able to identify all particle boundaries precisely, and also some boundary effects from interface of specimen holder surface is likely to affect the coordination number statistics.

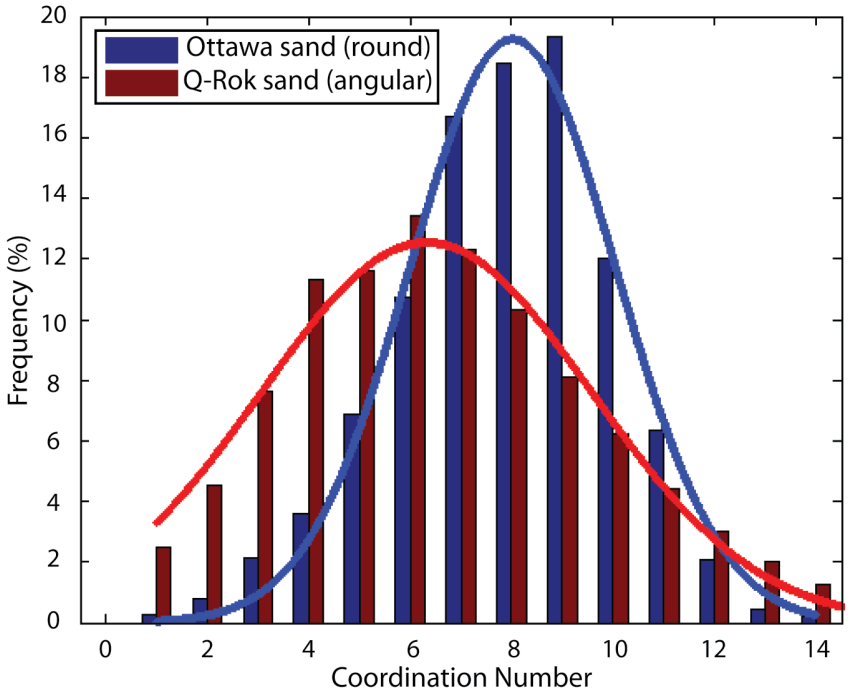


Figure 5.10: Coordination distribution for Ottawa sand with water and Q-ROK sand with water specimen

5.5.4 Representative Elementary Volume Analysis

Representative Elementary Volume (REV) is the volume over which a statistical average can be performed to interpret micro-structural information (Bear 1972). Macroscopic engineering properties can often be obtained from simulation at microscopic level using REVs. The connection between micro scale property and macro scale property is an ongoing research topic (Hopmans et al. 2002). The proper size of the REV for porosity was studied by Clausnitzer and

Hopmans, and found to be 5.15 times the bead diameter for uniform glass bead system (Clausnitzer and Hopmans 1999). Similar analysis with synchrotron tomography images of glass bead system and sand system was also performed (Al-Raoush 2002). In this research, REV analysis was performed for Ottawa sand with water and Q-ROK sand with water specimens for both porosity and saturation. Cubical REV was chosen, and the size of the REV was varied from 1×1×1 mm^3 to 6×6×6 mm^3 at a 0.5 mm difference in the cube length. The result is plotted in Figure 5.11 and Figure 5.12 for porosity and saturation respectively. Example REVs (3×3×3 mm^3) are shown in Figure 5.13.

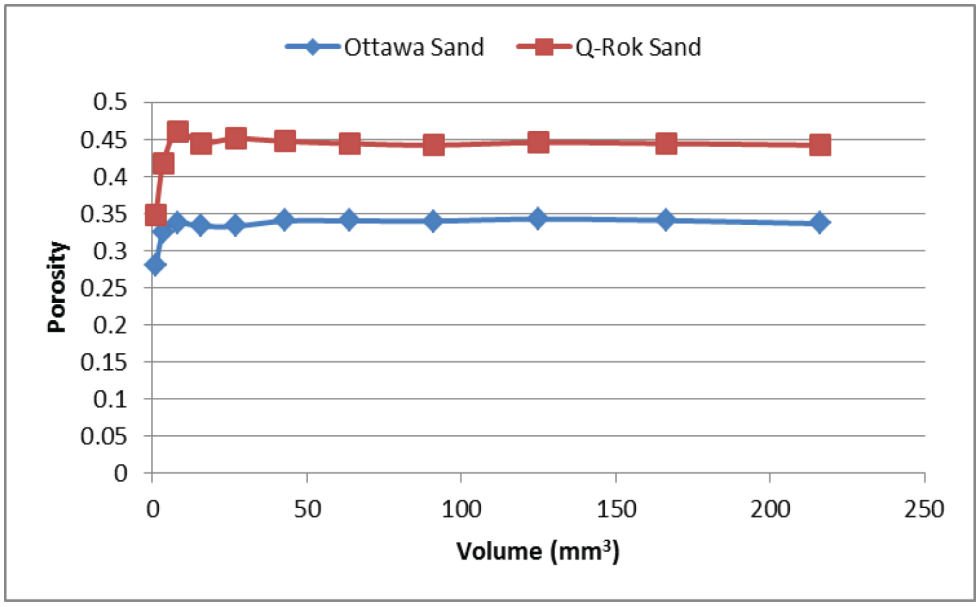


Figure 5.11: REV analysis of porosity

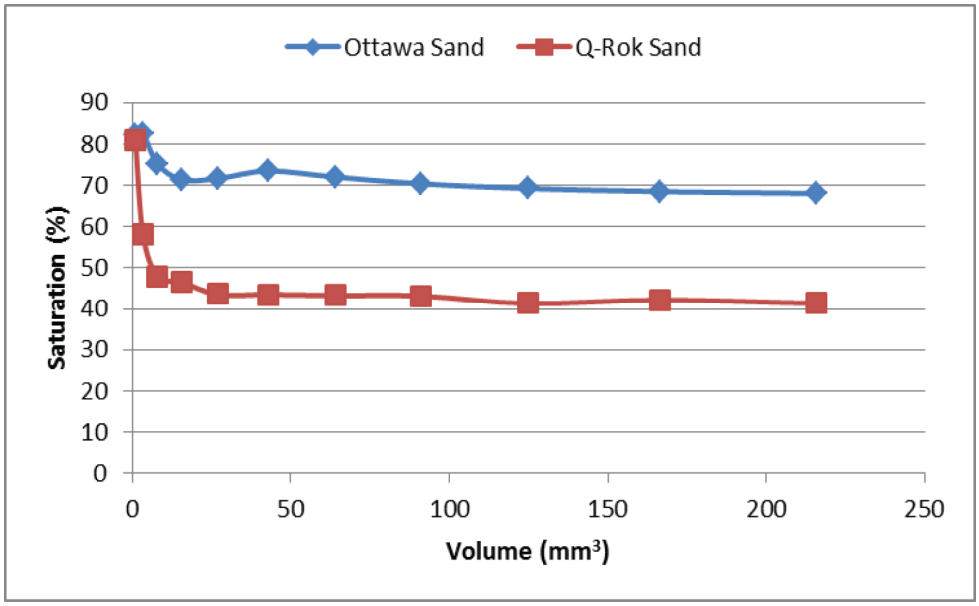


Figure 5.12: REV analysis of saturation

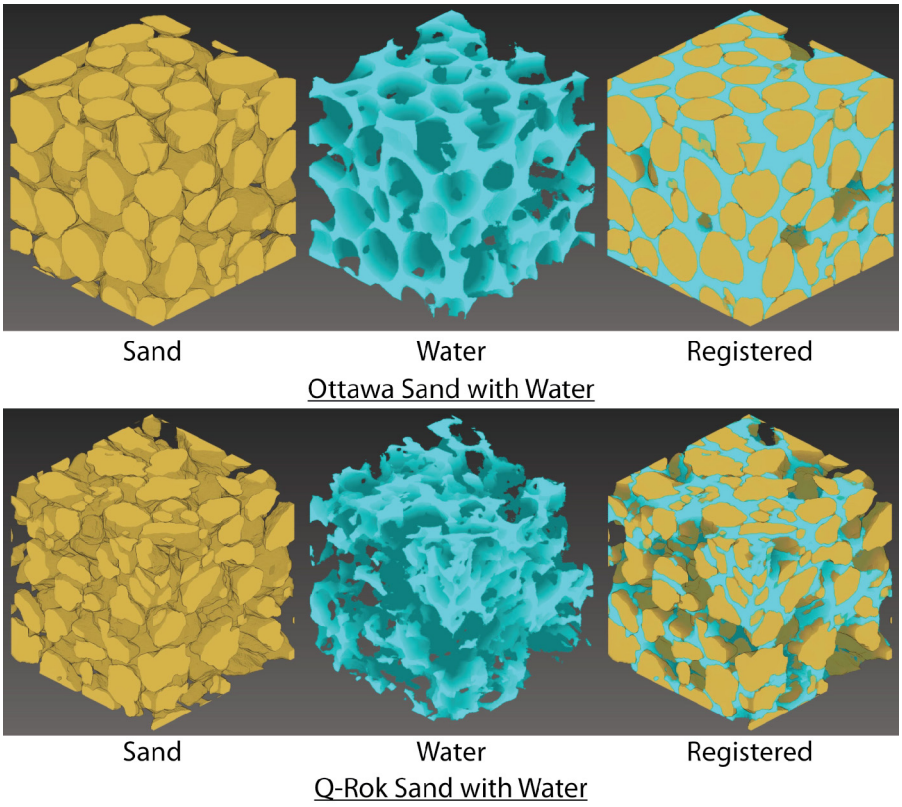


Figure 5.13: Example REV of 12% gravimetric water content Ottawa sand and Q-ROK sand at the third compaction layer with RVE volume of 3×3×3 mm^3

5.6 Conclusions

Dual modality of neutrons and X-rays on partially saturated sand was implemented to study the three phases (Silica sand, water and air) accurately by using image registration technique based on maximization of normalized mutual information. The objective of image registration is to align the neutron and X-ray

tomography data in the same coordinates and at comparable magnification. Using different modalities possible with neutron and X-ray attenuation, different phases of the partially saturated sand were identified with greater precision. The image registration technique enabled the combination of the sand and water phases together from different modalities. Partially saturated specimens were prepared with two different particle shapes (rounded Ottawa sand and angular Q-ROK sand), and the effects of different grain shape on water distribution and fabric were studied. The structure of the soil including the sand grain arrangement and water distributions were clearly visualized in three dimensions from the registered dual modality images. Coordination number and pore size distribution provided information about the fabric of the system. The variation of degree of saturation along the height of the specimen were found by combining the water volume obtained from neutron tomography and pore volume obtained from X-ray tomography. REV analysis was performed for porosity and saturation. The dual modality imaging combined with image registration technique presented in this paper has great potential to be directly applied to more complex in-situ experiments involving water flow and solid deformation. The dual modality imaging technique with image registration technique can be directly used for validation of more increasing use of direct numerical simulation techniques.

5.7 References

Al-Raoush, R. (2002). "Extraction of physically-realistic pore network properties from three-dimensional synchrotron microtomography images of unconsolidated porous media," Louisiana State University and Agricultural and Mechanical College, Baton Rouge, LA.

Al-Raoush, R., and Alshibli, K. A. (2006). "Distribution of Local Void Ratio in Porous Media Systems from 3D X-ray Microtomography Images." *PHYSICA A*, 361(2), 441-456.

Andò, E., Hall, S., Viggiani, G., Desrues, J., and Bésuelle, P. (2012). "Grain-scale experimental investigation of localised deformation in sand: a discrete particle tracking approach." *Acta Geotechnica*, 7(1), 1-13.

Bear, J. (1972). *Dynamics of fluids in porous media*, American Elsevier Publishing Company, Inc., New York, NY.

Becker, J., Wiegmann, A., and Schulz, V. (2007). "Design of fibrous filter media based on the simulation of pore size measures." Filtech Europa, Wiesbaden, Germany.

Brown, L. G. (1992). "A survey of image registration techniques." *ACM Comput. Surv.*, 24(4), 325-376.

Buades, A., Coll, B., and Morel, J. M. (2005). "A non-local algorithm for image denoising." *Computer Vision and Pattern Recognition, 2005. CVPR 2005. IEEE Computer Society Conference on*, 60-65 vol. 2.

Christe, P., Bernasconi, M., Vontobel, P., Turberg, P., and Parriaux, A. (2007). "Three-dimensional petrographical investigations on borehole rock samples: a comparison between X-ray computed- and neutron tomography." *Acta Geotechnica*, 2(4), 269-279.

Clausnitzer, V., and Hopmans, J. W. (1999). "Determination of phase-volume fractions from tomographic measurements in two-phase systems." *Advances in Water Resources*, 22(6), 577-584.

Collignon, A., Maes, F., Delaere, D., Vandermeulen, D., Suetens, P., and Marchal, G. (1995). "Automated multi-modality image registration based on information theory." *Information Processing in Medical Imaging*, 263-274.

Esteban, M. D., and Morales, D. (1995). "A summary on entropy statistics." *Kybernetika*, 31(4), 337-346.

Ferréol, B., and Rothman, D. H. (1995). "Lattice-Boltzmann simulations of flow through Fontainebleau sandstone." *Transport in Porous Media*, 20(1), 3-20.

Gonzalez, R. C., and Woods, R. E. (2008). *Digital Image Processing*, Pearson Prentice Hall, Upper Saddle River, NJ.

Hazlett, R. D. (1995). "Simulation of capillary-dominated displacements in microtomographic images of reservoir rocks." *Transport in Porous Media*, 20(1), 21-35.

Hopmans, J. W., Nielsen, D. R., and Bristow, K. L. (2002). "How useful are small-scale soil hydraulic property measurements for large-scale vadose zone modeling?" *Geophysical Monograph*, 129, 247-258.

Kaddhour, G., Ando, E., Salager, S., Bésuelle, P., Viggiani, C., Hall, S., and Desrues, J. (2013). "Application of X-ray Tomography to the Characterisation of Grain-Scale Mechanisms in Sand

Multiphysical Testing of Soils and Shales." L. Laloui and A. Ferrari, eds., Springer Berlin Heidelberg, 195-200.

Kim, F. H., Penumadu, D., Gregor, J., Kardjilov, N., and Manke, I. (2013a). "High resolution neutron and X-ray imaging of granular materials." *Journal of Geotechnical and Geoenvironmental Engineering*, 139(5), 715-723.

Kim, F. H., Penumadu, D., and Hussey, D. S. (2012). "Water Distribution Variation in Partially Saturated Granular Materials Using Neutron Imaging." *Journal of Geotechnical and Geoenvironmental Engineering, American Society of Civil Engineers (ASCE)*, 138(2), 147-154.

Kim, F. H., Penumadu, D., Schulz, V. P., and Wiegmann, A. (2013b). "Pore Size Distribution and Soil Water Suction Curve from Micro-tomography Measurements and Real 3-D Digital Microstructure of a Compacted Granular Media by Using Direct Numerical Simulation Technique." Multiphysical Testing of Soils and Shales, L. Laloui and A. Ferrari, eds., Springer Berlin Heidelberg, 171-176.

Kudejova, P., Cizek, J., Schulze, J., Jolie, J., Schillinger, B., Lorenz, K., Mühlbauer, M., Masschaele, B., Dierick, M., and Vlassenbroeck, J. (2007). "A marker-free 3D image registration for the ANCIENT CHARM project. Case study with neutron and X-ray tomography datasets." *Notziario Neutrioni e Luce di Sincrotrone*, 12(2), 6-13.

Kumar, M., Lebedeva, E., Melean, Y., Madadi, M., Sheppard, P., Varslot, T. K., Kingston, A. M., Latham, S. J., Sok, R. M., Sakellariou, A., Arns, C. H., Senden, T. J., and Knackstedt, M. A. (2010). "Micro-petrophysical experiments via tomography and simulation." *Advances in Computed Tomography for Geomaterials : GeoX 2010*, New Orleans, LA, USA, 238-253.

Latham, S. J., Varslot, T. K., and Sheppard, A. P. (2008). "Automated registration for augmenting micro-CT 3D images." *Proceedings of the 14th Biennial Computational Techniques and Applications Conference, CTAC-2008*, C534-C548.

Maes, F., Vandermeulen, D., and Suetens, P. (1999). "Comparative evaluation of multiresolution optimization strategies for multimodality image registration

by maximization of mutual information." *Medical Image Analysis*, 3(4), 373-386.
Maintz, J. B. A., and Viergever, M. A. (1998). "A survey of medical image registration." *Medical Image Analysis*, 2(1), 1-36.
Manke, I., Markötter, H., Tötzke, C., Kardjilov, N., Grothausmann, R., Dawson, M., Hartnig, C., Haas, S., Thomas, D., Hoell, A., Genzel, C., and Banhart, J. (2011). "Investigation of Energy-Relevant Materials with Synchrotron X-Rays and Neutrons." *Advanced Engineering Materials*, 13(8), 712-729.
Matsushima, U., Graf, W., Zabler, S., Kardjilov, N., and Herppich, W. B. (2009). "Application of cold neutron and synchrotron X-ray imaging to investigate rose bent neck syndrome." *Acta Hort. (ISHS)*, 847, 279-286.
Mitchell, J. K., and Soga, K. (2005). "Fundamentals of Soil Behavior (3rd Edition)." John Wiley & Sons.
Muhunthan, B., and Chameau, J. L. (1997). "Void Fabric Tensor and Ultimate State Surface of Soils." *Journal of Geotechnical and Geoenvironmental Engineering*, 123(2), 173-181.
Oda, M. (1972a). "Initial Fabrics and Their Relations to Mechanical Properties of Granular Material." *Soils and Foundations*, 12(1), 17-36.
Oda, M. (1972b). "The Mechanism of Fabric Changes During Compressional Deformation of Sand." *Soils and Foundations*, 12(2), 1-18.
Oda, M. (1972c). "Deformation Mechanism of Sand in Triaxial Compression Tests." *Soils and Foundations*, 12(4), 45-63.
Pluim, J. P. W., Antoine Maintz, J. B., and Viergever, M. A. (2000). "Interpolation Artefacts in Mutual Information-Based Image Registration." *Computer Vision and Image Understanding*, 77(2), 211-232.
Pluim, J. P. W., Maintz, J. B. A., and Viergever, M. A. (2003). "Mutual-information-based registration of medical images: a survey." *Medical Imaging, IEEE Transactions on*, 22(8), 986-1004.
Shannon, C. E. (1948). "A mathematical theory of communication." *The Bell System Technical Journal*, 27, 379-4223/623-656.
Soille, P. (1999). "Morphological Image Analysis: Principles and Applications." Springer-Verlag Berlin Heidelberg, 89-125.
Spanne, P., Thovert, J. F., Jacquin, C. J., Lindquist, W. B., Jones, K. W., and Adler, P. M. (1994). "Synchrotron Computed Microtomography of Porous Media: Topology and Transports." *Physical Review Letters*, 73(14), 2001-2004.
Studholme, C., Hill, D. L. G., and Hawkes, D. J. (1999). "An overlap invariant entropy measure of 3D medical image alignment." *Pattern Recognition*, 32(1), 71-86.
Trtik, P., Münch, B., Weiss, W. J., Kaestner, A., Jerjen, I., Josic, L., Lehmann, E., and Lura, P. (2011). "Release of internal curing water from lightweight aggregates in cement paste investigated by neutron and X-ray

tomography." *Nuclear Instruments and Methods in Physics Research Section A: Accelerators, Spectrometers, Detectors and Associated Equipment*, 651(1), 244-249.

Tsao, J. (2003). "Interpolation artifacts in multimodality image registration based on maximization of mutual information." *Medical Imaging, IEEE Transactions on*, 22(7), 854-864.

Viola, P., and Wells, W. M., III. (1995). "Alignment by maximization of mutual information." *Computer Vision, 1995. Proceedings., Fifth International Conference on*, 16-23.

Winkler, B. (2006). "Applications of Neutron Radiography and Neutron Tomography." *Reviews in Mineralogy and Geochemistry*, 63(1), 459-471.

Winkler, B., Knorr, K., Kahle, A., Vontobel, P., Lehmann, E., Hennion, B., and Bayon, G. (2002). "Neutron imaging and neutron tomography as non-destructive tools to study bulk-rock samples." *European Journal of Mineralogy*, 14(2), 349-354.

Yang, X. (2005). "Three-Dimensional Characterization of Inherent and Induced Sand Microstructure," Gerogia Institute of Technology.

Zitová, B., and Flusser, J. (2003). "Image registration methods: a survey." *Image and Vision Computing*, 21(11), 977-1000.

CHAPTER 6. DIRECT NUMERICAL SIMULATION BASED ON IMAGE DATA

This chapter is revised partially based on a conference paper published by Felix Kim, Dayakar Penumadu et al. :

Kim, F. H., Penumadu, D., Schulz, V. P., and Wiegmann, A. (2013). "Pore Size Distribution and Soil Water Suction Curve from Micro-tomography Measurements and Real 3-D Digital Microstructure of a Compacted Granular Media by Using Direct Numerical Simulation Technique." Multiphysical Testing of Soils and Shales, L. Laloui and A. Ferrari, eds., Springer Berlin Heidelberg, 171-176.

My primary contributions to the paper included: (i) Understanding full morphology simulation method and permeability simulation method, (ii) gathering and reviewing literature, (iii) performing X-ray imaging at Helmholtz-Zentrum-Berlin, (iv) processing, analyzing, and interpretation of the numerical simulation data, (v) most of the writing.

6.1 Abstract

Direct numerical simulation was performed to estimate engineering properties based on image data obtained from X-ray tomography. X-ray tomography provides actual pore geometry accurate to resolution level. Full morphology method is performed on Ottawa sand pore geometry to predict capillary pressure – saturation curve for drainage condition. The effect of image threshold level on capillary pressure – saturation curve is investigated. The effect of solid-liquid contact angle on capillary pressure – saturation curve is investigated. Hydraulic conductivity is also estimated based on image data by numerically solving Stokes equation and based on Darcy's law.

6.2 Introduction

The deformation and fluid flow behavior of partially saturated granular medium (soil) is a complex and important problem. The complexity arises from the particulate nature of soil which is composed of three phases (solid, gas, and liquid). The true nature of deformation and fluid flow can be revealed more accurately when the particulate material is studied at the grain/pore scale. The small size (< 1 mm) of individual particle and the large number of particles involved has prohibited researchers from studying soil at grain/pore level with traditional experimental and numerical techniques. Recently, imaging technique such as X-ray tomography technique has been used popularly to study the soil

and porous rock geometry (Alshibli et al. 2000; Desrues et al. 1996). The fluid phase of porous media has also been visualized with X-ray by using contrast agents (Al-Raoush and Willson 2005; Schnaar and Brusseau 2005). Neutron imaging technique has also been used to study mainly the fluid phase without using a contrast agent (de Beer and Middleton 2006; Hassanein et al. 2006; Kim et al. 2012). The author have recently performed an experimental approach to utilize the dual modality contrast of neutron and X-ray tomography images to study three phases of partially saturated sand (Kim et al. 2013).

Traditionally, numerical simulations have been performed at the macroscopic level with continuum assumption. Discrete element method (DEM) has been developed and applied to study the particulate nature of granular materials focusing on the solid phase (e.g. Cundall and Strack 1979; Iwashita and Oda 1998; Yimsiri and Soga 2010). The complex nature of pore geometry makes it difficult to simulate the fluid flow. Several research projects have been performed to simulate the fluid flow behavior at a pore level from realistic microstructure of various porous media generated either from X-ray tomography or by stochastic methods (Hazlett 1995; Schulz et al. 2007; Spanne et al. 1994). Macroscopic properties such as permeability, thermal conductivity, diffusion and capillary pressure – saturation curves of porous media have been obtained from microstructure of various porous media (Becker et al. 2008; Ferréol and Rothman 1995; Vogel et al. 2005).

In this research, predictive measurements of hydraulic and transport properties are computed from a realistic microstructure of sand column obtained from X-ray micro-tomography. Phase distribution for different saturation according to change in capillary pressure is computed and visualized, and capillary pressure – saturation curves (soil water suction curves) were generated. The basic principles of full morphology method are explained. The sensitivity to the choice of threshold on pore size distribution and capillary pressure – saturation curves were investigated. The effect of solid – fluid contact angle on capillary pressure – saturation curve is also investigated. Additionally, the hydraulic conductivity was simulated from the microstructure. Different sizes of REVs were used to compute hydraulic conductivities, and the convergence is investigated. Simulated hydraulic conductivity was compared for Ottawa sand and Q-ROK sand.

6.3 Full Morphology Method

6.3.1 Principles

Full morphology model is based on the work by Hilpert and Miller (2001), the stationary distribution of wetting phase (WP) and non-wetting phase (NWP) for an arbitrary capillary pressure (p_c) can be determined. Schulz et al. employed a so-called full-morphology model for the quasi-static drainage simulation of liquid water in a porous media (Schulz et al. 2007). The simulations presented

here run the full morphology method as implemented in the GeoDict code (www.geodict.com). The pore size is the main factor determining the drainage at a given capillary pressure. Morphological opening is used to determine the pore size distribution as shown in equation 6.1 where *X* represents the pore space and *B* is the structuring element. O_B is the pore space that the structuring element fits in determined from morphological opening process.

$$O_B(X) = \bigcup \{B \mid B \subseteq X\} \tag{6.1}$$

A spherical structuring element with radius *r* is used, and the method assumes a spherical interface between WP and NWP. The radius *r* is the constant curvature radius of the WP and NWP interface, and it is also related to capillary pressure determined with Young – Laplace equation shown in equation 6.2. Capillary pressure (p_c) is related to surface tension (γ) between WP and NWP and contact angle (θ) between WP and solid phase.

$$p_c = \frac{2\gamma \cos\theta}{r} \tag{6.2}$$

A simulation of drainage condition can be performed by applying morphological opening operations with a test for connectivity to NWP reservoir. It is assumed that the volume is connected to NWP reservoir in one end and WP reservoir on the other end. An illustrative example of the morphological opening process for a drainage step is shown in Figure 6.1. The dry porous medium is shown in Figure 6.1a. The porous medium is assumed to be fully saturated with the WP initially as shown in Figure 6.1b, and NWP replaces the WP to simulate

drainage process. The pore space is eroded by spheres with increasing radius *r* starting with the smallest radius corresponding to the largest capillary pressure as shown in Figure 6.1c. The pores can be filled with NWP if the erosion of the pore space has a continuous connection to the NWP reservoir. The eroded pore phase that has connected to WP reservoir (Figure 6.1d) is dilated with the same structuring element to complete the opening process as shown in Figure 6.1e. The saturation of the WP is basically the volume fraction of WP compared to the total volume of pores. The whole process is repeated for the next structuring element with a larger radius. Based on the results of capillary pressure and WP saturation, a capillary pressure – saturation curve is generated.

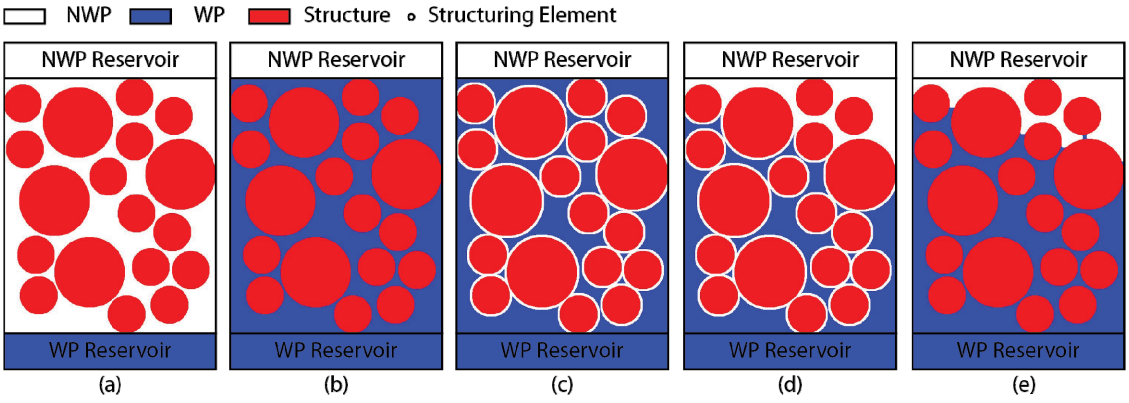


Figure 6.1: Illustration of morphological opening step for drainage simulation shown with initial unsaturated state (a), fully saturated with WP (b), erosion step (c), connectivity to WP (d) and dilation step (e)

6.3.2 Materials and Methods

The dataset used here is Ottawa sand dry data obtained from HZB. The sand is placed in an aluminum sample holder. The sand is compacted in three layers to be at dense configuration. The three dimensional (3D) realistic microstructure of dry Ottawa sand (20/40 Oil Frac) column is obtained from micro-focus X-ray tomography at Helmholtz-Zentrum-Berlin (HZB). The dry Ottawa sand is placed in a custom developed thin walled aluminum compaction mold as shown in Figure 6.2a. The inner dimension is about 10 mm dia. × 23 mm height. The average Ottawa sand grain diameter is around 700 μm. The system consists of microfocus X-ray source and a flat panel detector. The detector has 50 μm pixel sizes, and the specimen was magnified about 4.46 times resulting in the effective image voxel size of 11.2 μm. The image data was smoothened with 3D median filter and thresholded to binary data. Parts of the volume comprising about 1000^3 voxels (11.2^3 mm^3/voxel) as shown in Figure 6.2b are used for the analysis. An example tomography slice is shown in Figure 6.2c, and good contrast between sand phase and air phase is presented. The 3D view of the thresholded sand phase is shown in Figure 6.2d.

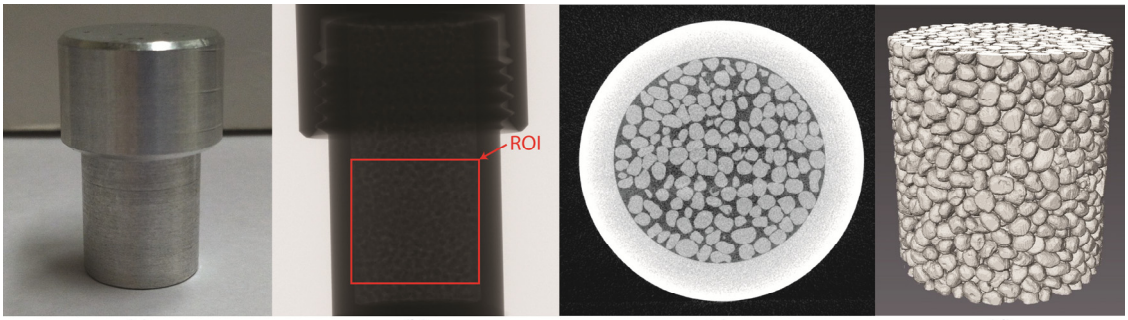


Figure 6.2: Picture of the aluminum compaction mold (a), X-ray radiography of dry Ottawa sand specimen (b), reconstructed slice (c), and 3D volume rendering of the dry Ottawa sand specimen segmented from X-ray tomography (d)

6.3.3 Thresholding

From the original dataset, smoothing operations were performed for easier thresholding. Median 3D filter (3×3×3) and median 3D filter (5×5×5) were applied to smooth data and remove noise. Histogram variation for different smoothing operations is shown in Figure 6.3. In the original data set histogram, there is no clear peak for air, sand and aluminum phases. After median 3D filter is applied, clear peaks of air, sand and aluminum phases are obtained. The dataset after median 3D filter (5×5×5) was applied showed nicer peaks.

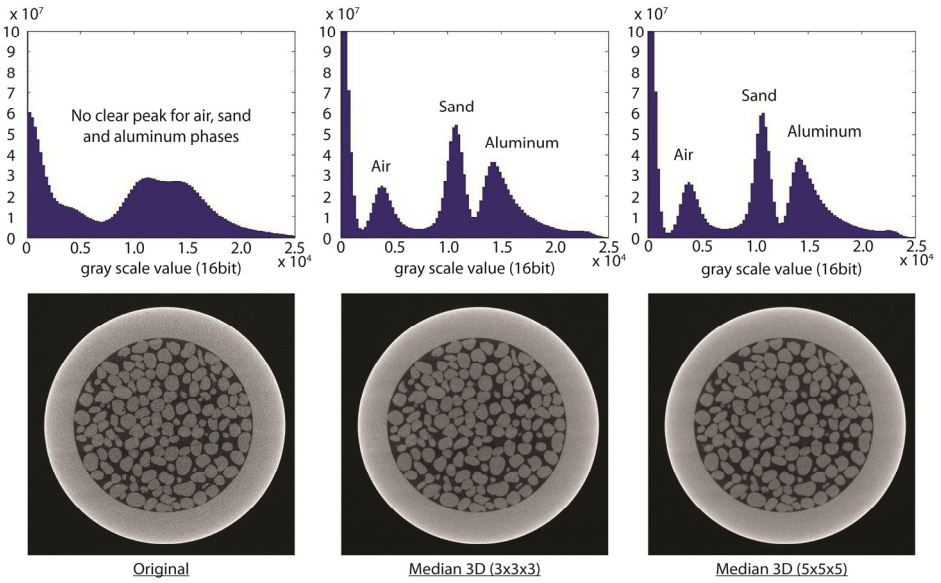


Figure 6.3: Histogram comparison for original data, and median 3D (3x3x3) filter applied and median 3D (5x5x5) filter applied

For the dataset after median 3D (5×5×5) applied, different threshold values were chosen. The ideal threshold value was found automatically by applying an automatic thresholding algorithm based on factorization method (Otsu 1979). From the threshold, ±500 gray scale values were chosen for comparison. The threshold values in the histogram are shown in Figure 6.4. The porosity values computed based on the different threshold values are shown in Table 6.1.

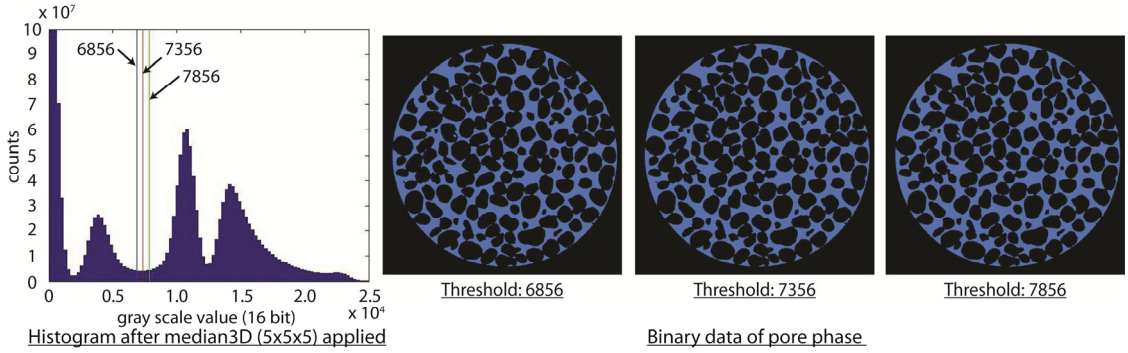


Figure 6.4: Different threshold values and binary results comparison

Table 6.1: Porosity values at different threshold levels

Threshold	Porosity
6856	0.371
7356	0.383
7856	0.395

6.3.4 Pore Size Distribution and Full Morphology Simulations

Once the binary structure is obtained for different thresholds, pore size distribution is compared for the different thresholds. The pore size distribution and cumulative pore size distribution curves are shown in Figure 6.5 and Figure 6.6 respectively.

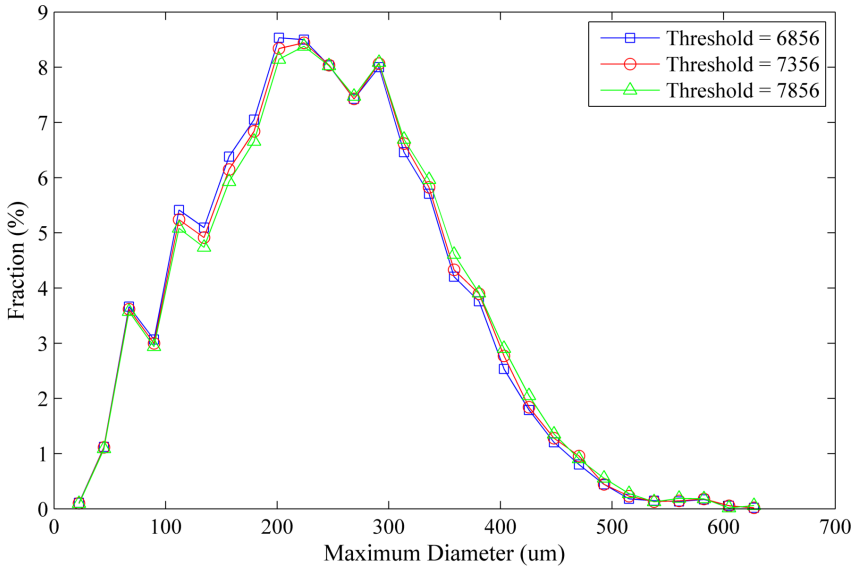


Figure 6.5: Pore size distribution for different threshold values

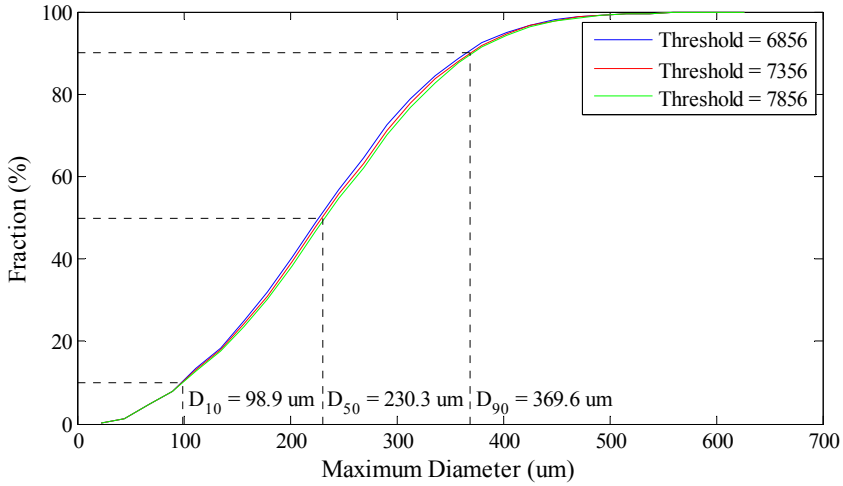


Figure 6.6: Cumulative pore size distribution for different threshold values

The drainage simulations were performed by using the full-morphology method for the three different thresholds. The full capillary pressure – saturation curve is shown in Figure 6.7 for the entire curve and in Figure 6.8 for capillary pressure range between 1 and 2 kPa. In this case, the pore radius (r) was varied from 11.2 μm to 313.6 μm in 28 equal steps. The capillary pressure was varied from 12.991 kPa to 0.467 kPa according to equation 6.2 for contact angle of 0°. The surface tension (γ) was assumed to be 72.75 mN/m. It is observed that negligible difference in the curve was obtained due to the change of threshold values.

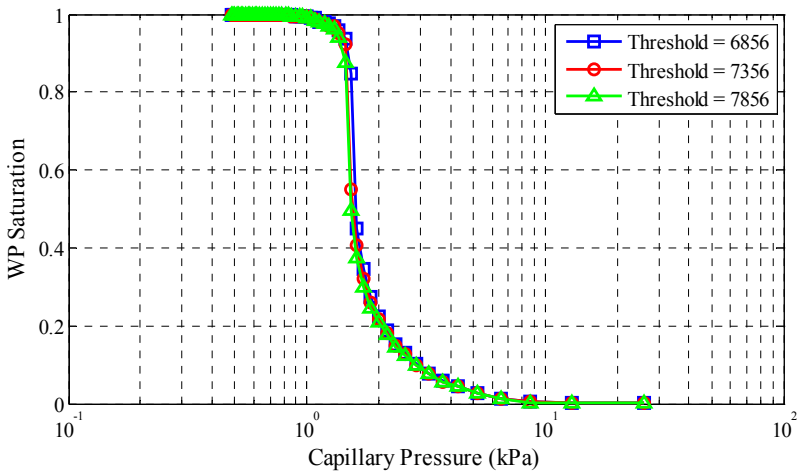


Figure 6.7: Capillary pressure – saturation curves for different threshold values

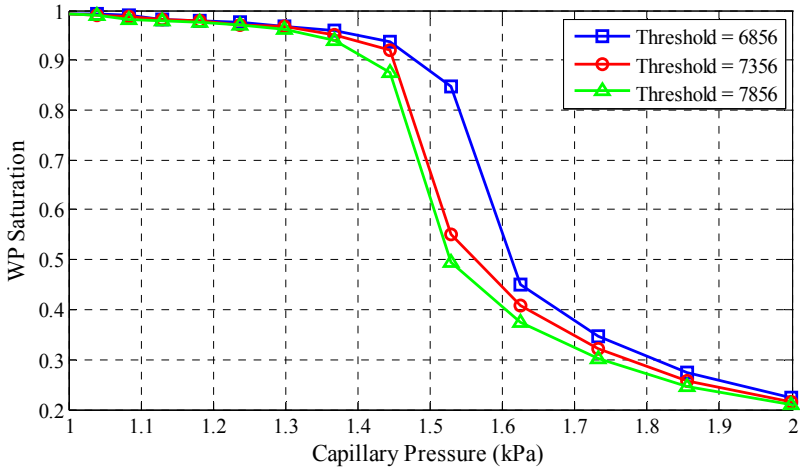


Figure 6.8: Capillary pressure – saturation curves for different threshold values magnified between capillary pressure of 1 kPa and 2 kPa

6.3.5 Effect of Contact Angle

It is known that the solid-fluid contact angle is an important factor affecting capillary pressure. The Young-Laplace equation in equation 6.2 has also the term for the contact angle. Based on literatures, three different contact angles of water (0°, 27°and 60°) were chosen. Capillary pressure – saturation curves for primary drainage and arbitrarily mobile fluids are shown in Figure 6.9. The advancing and receding contact angle of water on silica is found to be near 60° and 27° respectively (Ishakoglu and Baytas 2005). It shows that the difference with contact angle affected the capillary pressure – saturation relationship

significantly. An example stationary WP and NWP distributions for different capillary pressures are presented in Figure 6.10 for the case of 0° contact angle.

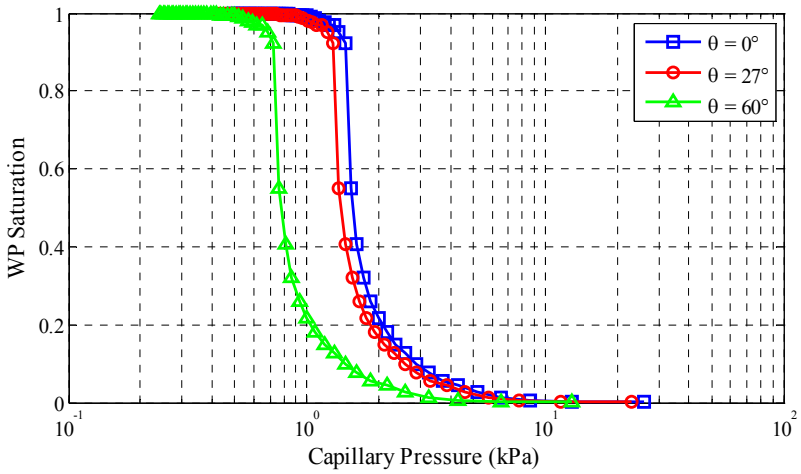


Figure 6.9: Effect of different contact angles on capillary pressure – saturation curves

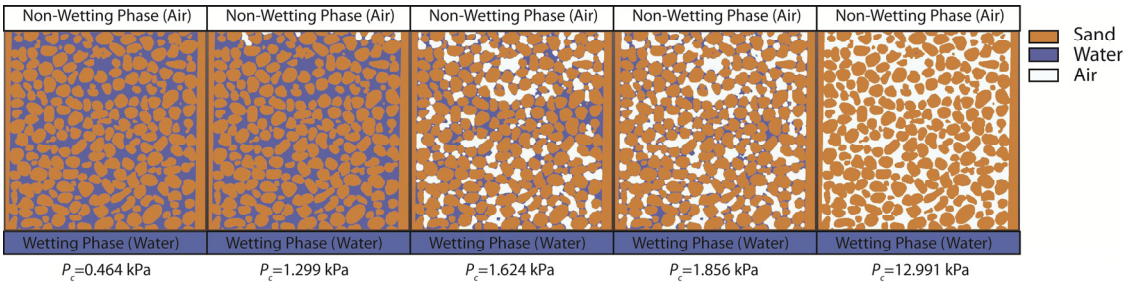


Figure 6.10: Simulated two phase distribution for contact angle 0°

6.4 Hydraulic Conductivity Simulation

6.4.1 Permeability and Hydraulic Conductivity

Permeability is a measure of the ability of a porous material to allow fluids to pass through it. Permeability is a parameter describing how easily a fluid can move through pore spaces. Permeability depends on many factors including soil fabric, porosity, effective pore size, shape of voids and flow path through the soil pores (tortuosity) (Holtz and Kovacs 1981). The degree of saturation also influences the actual permeability in the field. The property of fluid (viscosity and density) also has some effect on permeability. The absolute permeability is defined as the mean permeability of the material when the entire pore space is filled with a fluid of one type only. When the fluid is water, we are measuring hydraulic conductivity or water coefficient of permeability. Since water is the most common fluid associated with soil, hydraulic conductivity is an important engineering parameter for characterization of soil. In soil mechanics, the terms permeability and hydraulic conductivity are often used interchangeably. In this chapter, however, a distinction will be made where permeability is in the unit of length squared, and hydraulic conductivity is in the unit of length over time where the fluid viscosity and unit weight is taken into consideration. For experimental determination of hydraulic conductivity, significant amount of time is required to fully saturate soil perform the experiment. Once the soil specimen is fully saturated, the amount of water flow is measured for a given time where pressure

is either constant or falling. The Darcy's law is used to estimate permeability or hydraulic conductivity.

Experimental approach requires considerable amount of time for preparation and experiment. A new type of approach is to estimate hydraulic conductivity in a predictive sense based on numerical simulation. Direct numerical simulation (DNS) can be performed on a realistic microstructure obtained from X-ray tomography. Estimation of hydraulic conductivity with DNS approach is described in this section.

For simulation of permeability, Darcy's law is still used. An example form of Darcy's law is shown in equation 6.3 based on Figure 6.11 where Q is discharge in m^3/s, k is material permeability in m^2, A is the cross-sectional area in m^2, (P_a-P_b) is the pressure drop in Pa, μ_d is the dynamic viscosity in Pa·s, and L is the length over pressure drop is taking place in m. Darcy's law only applies to very slow (Stokes) flows with a Reynolds number of 0. In this flow regime, flow velocity changes linearly for a change of pressure.

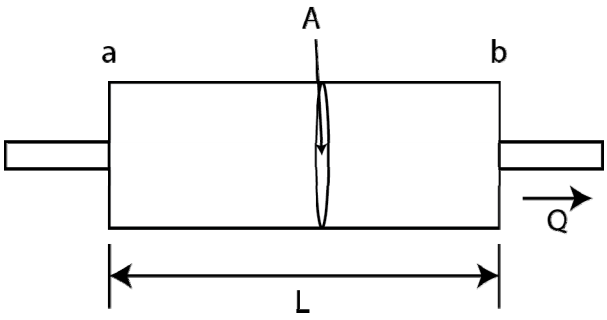


Figure 6.11: Darcy's law

$$Q = \frac{-kA}{\mu_d}\frac{P_b - P_a}{L} \tag{6.3}$$

In actual experiment of constant head permeability test, a modified form of Darcy's law is used to compute the hydraulic conductivity as shown in equation 6.4 where k_w is hydraulic conductivity commonly used in soil mechanics community in the unit of m/s, h_b - h_a is the total head difference in m.

$$k_w = -\frac{QL}{(h_b - h_a)A} \tag{6.4}$$

A following relationship can be obtained between k and k_w as shown in equation 6.5 where γ_w is the unit weight of water and μ_w is viscosity of water. Thus, permeability is a material property, and hydraulic conductivity considers the fluid property.

$$k_w = k\frac{\gamma_w}{\mu_w} \tag{6.5}$$

Navier-Stokes equation for incompressible fluid is shown in equation 6.6 (The conservation of momentum) and 6.7 (The conservation of mass) is generally used to describe the fundamental behavior of fluid flow where **u** is velocity vector, *p* and pressure, μ_d is dynamic viscosity of the fluid, ρ is the density of fluid. For very slow steady flow regime required for Darcy's law, simplified Stokes equation is acceptable. The conservation of momentum equation of Navier-Stokes equation is modified to equation 6.8 for Stokes equation.

$$\rho(\partial_t \mathbf{u} + (\mathbf{u} \cdot \nabla)\mathbf{u}) = -\nabla p + \mu_d \nabla^2 \mathbf{u} \quad 6.6$$

$$\nabla \cdot \mathbf{u} = 0 \quad 6.7$$

$$-\mu_d \nabla^2 \mathbf{u} + \nabla p = 0 \quad 6.8$$

For simulation, Darcy's law is modified to relate the pressure gradient and the average flow velocity ($\bar{u}$) with the permeability tensor (K) as shown in equation 6.9 where the viscosity is denoted by μ_d as shown in equation 6.9.

$$\bar{u} = -\frac{1}{\mu_d} K \nabla p \quad 6.9$$

The component K_{ij} of the permeability tensor represents the permeability of the material in the direction parallel to the j^{th} coordinate axis if the main flow direction is parallel to the i^{th} coordinate axis. For convenience, the edges of the sample are parallel to the Cartesian coordinate axes. As a result, the equation can be simplified as the equation 6.10 where $\overline{u_i}$ is the average flow speed, δp is

the pressure drop in the i[th] direction and L is the length of the edge of the sample which is parallel to the i[th] coordinate axis.

$$\overline{u_i} = -\frac{K_{ii}}{\mu_d L}\delta p \qquad 6.10$$

$$K_{ii} = -\frac{\mu_d L \overline{u_i}}{\delta p} \qquad 6.11$$

The diagonal component K_{ii} can be obtained for a choice of δp and μ_d if the $\overline{u_i}$ for i=1, 2, 3 can be computed. The average velocity ($\overline{u_i}$) can be found by solving the Stokes equation as an example. The permeability values can always be converted to estimate the hydraulic conductivity by using equation 6.5. Different governing equations such as Navier-Stokes equation or Stokes – Brinkmann equation can be used for different flow regimes and scales of the problem. The governing equation can be solved numerically by using Lattice-Boltzmann scheme or explicit jump scheme. In this work, computationally efficient explicit jump scheme is used (Wiegmann 2007; Wiegmann and Bube 2000).

6.4.2 Materials and Methods

The dry Ottawa sand specimen data used the section 6.3 is used here. A compacted Q-ROK sand specimen was also obtained at HZB in a similar imaging condition as that of the Ottawa sand specimen. Both sand specimens are prepared in an aluminum specimen holder with 3 compaction layers.

6.4.3 Representative Elementary Volume (REV) and Hydraulic Conductivity

Hydraulic conductivity simulation was performed on different size of REV of Ottawa sand. The side dimension of REV cube varied from 0.5 mm to 5.5 mm in 0.5 mm increments. The porosity variation is shown in Figure 6.12. It shows that porosity value starts to converge at the side dimension of 2.5 mm. Simulated hydraulic conductivity results for each direction of each REV are presented in Figure 6.13. The hydraulic conductivity value starts to converge at the REV dimension of about 4 mm.

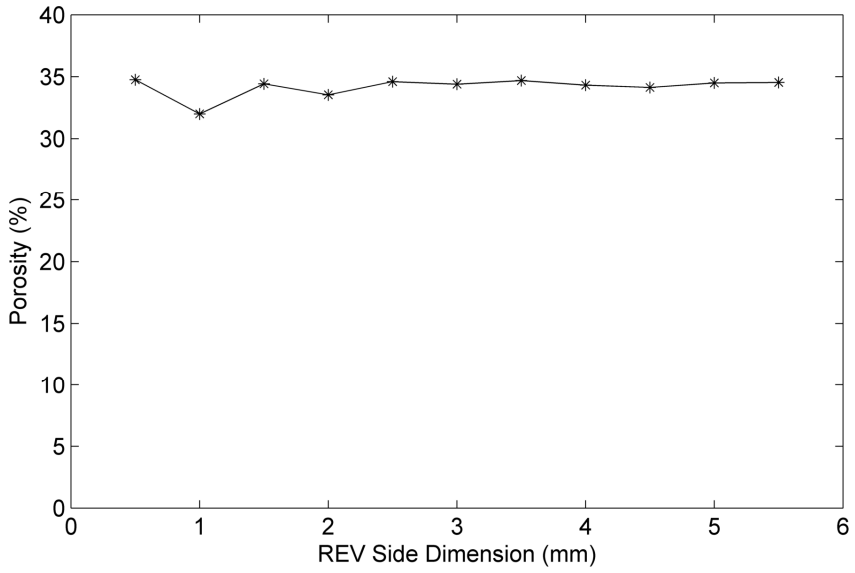


Figure 6.12: Porosity variation for different REV side dimensions

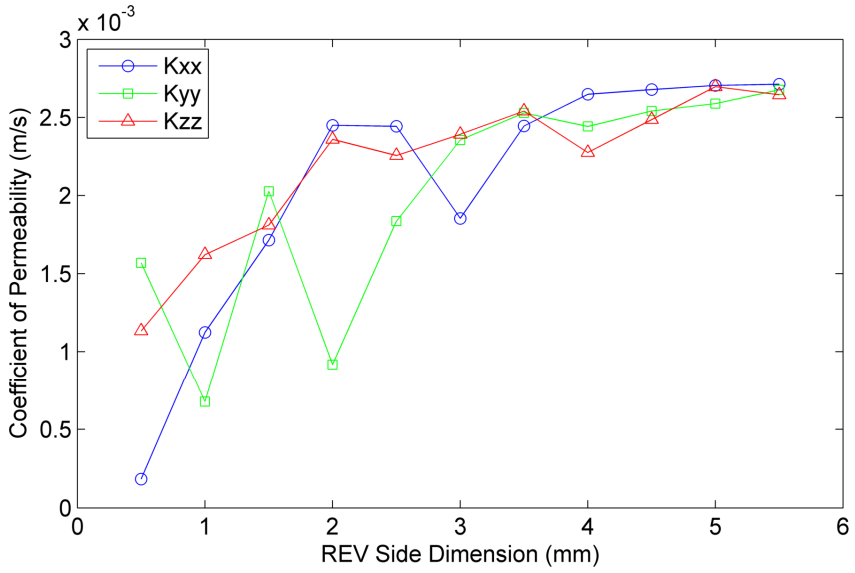


Figure 6.13: Hydraulic conductivity for different size of REV

6.4.4 Grain Shape Effect

Hydraulic conductivities of Ottawa sand and Q-ROK sand specimens are compared. The porosity and coefficient of hydraulic conductivity in each direction are shown in Table 6.2. Approximately the same dimension of volume (5 mm × 5 mm × 5 mm) was used to perform permeability simulation at different directions. Pressure difference is set to 0.02 Pa. The value of pressure difference does not matter since Stokes equation is used. Even though Q-ROK sand specimen has a higher porosity than that of the Ottawa sand specimen, the simulated hydraulic conductivity is lower. Higher tortuosity due to angular grain shape possibly has influenced the result. The number of iterations to reach convergence on the

hydraulic conductivity is shown in Figure 6.14. Example result of simulated velocity distributions are shown in Figure 6.15 for Ottawa sand.

Table 6.2: Simulated hydraulic conductivity values of Ottawa and Q-ROK sand

	Ottawa Sand	Q-ROK Sand
Porosity	0.345	0.402
K_{xx} (m/s)	0.00271	0.00223
K_{yy} (m/s)	0.00259	0.00228
K_{zz} (m/s)	0.00270	0.00220

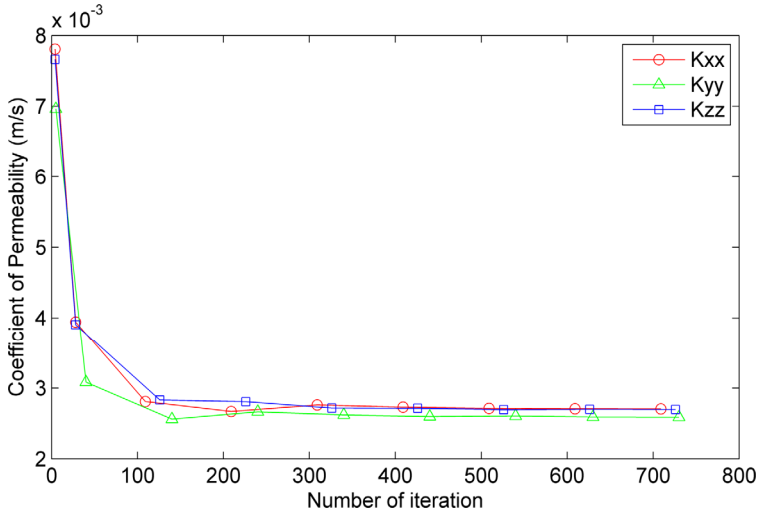


Figure 6.14: The number of iteration to reach convergence of Ottawa sand data

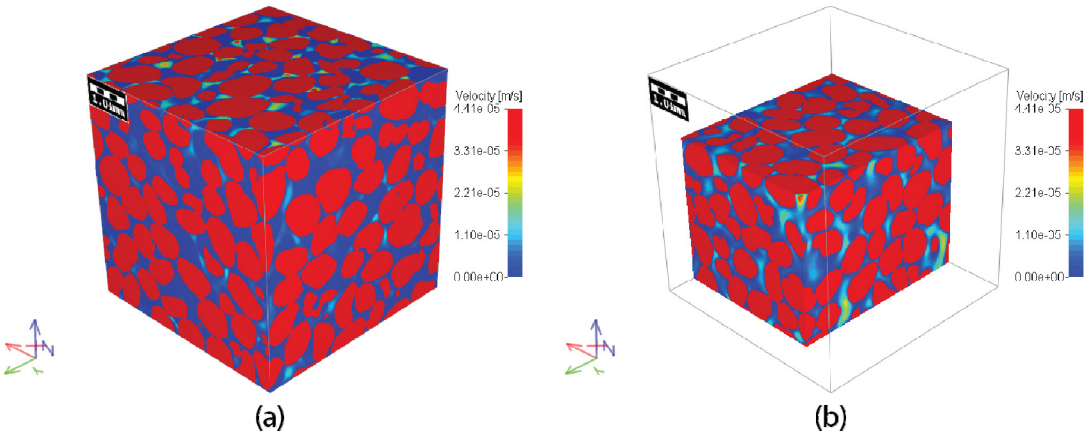


Figure 6.15: Simulated velocity profile Ottawa sand specimen at the edge (a) and around the area where high velocity is found (b)

6.5 Conclusion

A direct numerical simulation approach was applied to predict capillary pressure– saturation curve based on a realistic microstructure of dry Ottawa sand obtained with X-ray micro-tomography. General description of the full morphology method was explained. Capillary pressure – saturation curves for appropriate contact angles were simulated, and the effect of contact angle with predictive measurement was demonstrated. The predictions of suction versus saturation for Ottawa sand generally agree with published literature. The direct numerical simulation technique not only provides simulation results based on actual geometry of porous media, but it also provides opportunity to compare simulation results directly with image data of physical experiment results. Permeability of Ottawa sand and Q-ROK sand was also computed by solving Stokes equation numerically based on X-ray tomography image data.

6.6 References

Al-Raoush, R. I., and Willson, C. S. (2005). "A pore-scale investigation of a multiphase porous media system." *Journal of Contaminant Hydrology*, 77(1-2), 67-89.

Alshibli, K. A., Sture, S., Costes, N. C., Frank, M. L., Lankton, M. R., Batiste, S. N., and Swanson, R. A. (2000). "Assessment of Localized Deformations in Sand Using X-Ray Computed Tomography." *Geotecnical Testing Journal*, 23(3), 274-299.

Becker, J., Schulz, V., and Wiegmann, A. (2008). "Numerical Determination of Two-Phase Material Parameters of a Gas Diffusion Layer Using Tomography Images." *Journal of Fuel Cell Science and Technology*, 5(2), 021006-9.

Cundall, P. A., and Strack, O. D. L. (1979). "A discrete numerical model for granular assemblies." *Géotechnique*, 29(1), 47-65.

de Beer, F. C., and Middleton, M. F. (2006). "Neutron Radiography Imaging, Porosity and Permeability in Porous Rocks." *South African Journal of Geology*, 109(4), 541-550.

Desrues, J., Chambon, R., Mokni, M., and Mazerolle, F. (1996). "Void ratio evolution inside shear bands in triaxial sand specimens studied by computed tomography." *Géotechnique*, 46(3), 529-546.

Ferréol, B., and Rothman, D. H. (1995). "Lattice-Boltzmann simulations of flow through Fontainebleau sandstone." *Transport in Porous Media*, 20(1), 3-20.

Hassanein, R., Meyer, H. O., Carminati, A., Estermann, M., Lehmann, E., and Vontobel, P. (2006). "Investigation of Water Imbibition in Porous Stone by Thermal Neutron Radiography." *Journal of Physics D: Applied Physics*, 39(19), 4284-4291.

Hazlett, R. D. (1995). "Simulation of capillary-dominated displacements in microtomographic images of reservoir rocks." *Transport in Porous Media*, 20(1), 21-35.

Hilpert, M., and Miller, C. T. (2001). "Pore-morphology-based simulation of drainage in totally wetting porous media." *Advances in Water Resources*, 24(3-4), 243-255.

Holtz, R. D., and Kovacs, W. D. (1981). *An Introduction to Geotechnical Engineering*, Prentice Hall, Englewood Cliffs, NJ

Ishakoglu, A., and Baytas, A. F. (2005). "The influence of contact angle on capillary pressure-saturation relations in a porous medium including various liquids." *International Journal of Engineering Science*, 43(8-9), 744-755.

Iwashita, K., and Oda, M. (1998). "Rolling Resistance at Contacts in Simulation of Shear Band Development by DEM." *Journal of Engineering Mechanics*, 124(3), 285-292.

Kim, F. H., Penumadu, D., Gregor, J., Kardjilov, N., and Manke, I. (2013). "High resolution neutron and X-ray imaging of granular materials." *Journal of Geotechnical and Geoenvironmental Engineering*, 139(5), 715-723.

Kim, F. H., Penumadu, D., and Hussey, D. S. (2012). "Water Distribution Variation in Partially Saturated Granular Materials Using Neutron Imaging." *Journal of Geotechnical and Geoenvironmental Engineering, American Society of Civil Engineers (ASCE)*, 138(2), 147-154.

Otsu, N. (1979). "A threshold selection method from gray-level histograms." *IEEE Transactions on Systems, Man, and Cybernetics* SMC-9(1), 62-66.

Schnaar, G., and Brusseau, M. L. (2005). "Pore-Scale Characterization of Organic Immiscible-Liquid Morphology in Natural Porous Media Using Synchrotron X-ray Microtomography." *Environmental Science & Technology*, 39(21), 8403-8410.

Schulz, V. P., Becker, J., Wiegmann, A., Mukherjee, P. P., and Wang, C.-Y. (2007). "Modeling of Two-Phase Behavior in the Gas Diffusion Medium of PEFCs via Full Morphology Approach." *Journal of The Electrochemical Society*, 154(4), B419-B426.

Spanne, P., Thovert, J. F., Jacquin, C. J., Lindquist, W. B., Jones, K. W., and Adler, P. M. (1994). "Synchrotron Computed Microtomography of Porous Media: Topology and Transports." *Physical Review Letters*, 73(14), 2001-2004.

Vogel, H.-J., Tölke, J., Schulz, V. P., Krafczyk, M., and Roth, K. (2005). "Comparison of a Lattice-Boltzmann Model, a Full-Morphology Model, and a Pore Network Model for Determining Capillary Pressure–Saturation Relationships." *Vadose Zone J.*, 4(2), 380-388.

Wiegmann, A. (2007). "Computation of the permeability of porous materials from their microstructure by FFF-Stokes." Fraunhofer ITWM.

Wiegmann, A., and Bube, K. P. (2000). "Wiegmann, A., & Bube, K. P. (2000). The explicit-jump immersed interface method: finite difference methods for PDEs with piecewise smooth solutions. SIAM Journal on Numerical Analysis, 37(3), 827-862." *SIAM Journal on Numerical Analysis*, 37(3), 827-862.

Yimsiri, S., and Soga, K. (2010). "DEM analysis of soil fabric effects on behaviour of sand." *Géotechnique*, 60(6), 483-495.

CHAPTER 7. HIGH RESOLUTION NEUTRON IMAGING OF FLOW THROUGH COMPACTED POROUS MEDIA

This chapter is revised partially based on a paper being prepared by Felix Kim, Dayakar Penumadu et al. :

Kim, F. H., Penumadu, D., Gregor, J., Kardjilov, N. and Manke, I. Schulz, V. (2013). High Resolution Neutron Imaging of Multi-phase Fluid Flow through Compacted Porous Media, Paper in preparation.

My primary contributions to the paper included: (i) Understanding the problem and preparing experimental setup, (ii) gathering and reviewing literature, (iii) performing imaging experiments at NIST, PSI and HZB, (iv) processing, analyzing, and interpretation of the experimental data, (v) most of the writing.

7.1 Abstract

In-situ imaging of water flow through silica sand of different initial state is performed with neutron radiography and tomography at neutron imaging facilities at National Institute of Standards and Technology (NIST), Paul Scherrer Institute (PSI) and Helmholtz-Zentrum Berlin (HZB). Neutron radiography and tomography experiments of flow through compacted sand were performed at NIST with relatively coarse spatial resolution (250 μm). At PSI NEUTRA beam line, simultaneous X-ray and neutron imaging was implemented to study flow through dense and loose states of sand with intermediate spatial resolution (150 μm). Cold neutron imaging beam line, CONRAD, at HZB was used to perform in-situ flow through compacted sand with high resolution (20 μm) neutron time-lapsed radiography and tomography. Initial microstructure of the compacted sand in dry state is obtained by using a micro-focus X-ray tomography system due to good contrast of silica and void phases. The flow of water is precisely controlled by using a syringe pump. Water is allowed to flow from bottom to top at a target flow rate. Time-lapsed neutron radiographs are obtained during the water injection stage, followed by neutron tomography after allowing sand specimen to reach equilibration for approximately 2 hours at the end of injection step. The distribution of water, air, and silica phase in three dimensions after injecting known amount of water under controlled conditions is obtained. This study has

broad implications to wide array of problems involving understanding of multi-phase transport through porous media.

7.2 Introduction

Understanding multi-phase fluid flow through porous media is a challenging problem and is affected by various material state variables such as the pore size distribution, pore shape and connectivity, wetting behavior of fluid-solid surface and boundary fluid flow conditions. The fluid flow rate and initial saturation are also known to be important parameters (DiCarlo 2010; DiCarlo et al. 2010).

As the radiation based imaging techniques using X-rays and neutrons mature, it is now possible to quantitatively describe the microstructure of a porous medium at pore/particle scale non-destructively. Experiments of flow through porous materials have been performed by using Synchrotron X-ray imaging (Coles et al. 1998; Silin et al. 2011). X-ray CT machine was used to visualize multi-phase fluid flow (David et al. 2008; Heijs et al. 1996; Kasteel et al. 2000; Perret et al. 1999). X-ray based imaging of fluid often requires addition of contrast agent to improve attenuation of fluid phase. Neutron radiography/tomography techniques have also been used to monitor fluid flow (Carminati et al. 2007; Cnudde et al. 2008; Hall et al. 2010; Hassanein et al. 2006). Based on the realistic geometries obtained from X-ray tomography, simulation attempts have been made to model two phase flow by using Lattice-

Boltzmann technique (Ferréol and Rothman 1995). Despite these preliminary studies, additional experimental results are needed to validate and refine the simulation models. Recent advances in neutron imaging with high contrast for water phase provide new insight to study water flow through porous medium.

Dual modality (i.e., using contrast from neutron and X-ray) imaging technique has been recently used to study distribution of solid, fluid and void phase in partially saturated sand specimens at grain scale by the authors (Kim et al. 2013). Image registration technique can be used to align the dual-modal data with different spatial resolution and orientations. Neutron imaging approach shows good contrast for water without adding any contrast agent (for example Cesium Chloride is often used for photons to get adequate contrast), and X-ray imaging shows good contrast of silica sand phase. A multi-modal (simultaneous or sequential use of both photons and neutrons) approach has been implemented to visualize the water flow through compacted sand specimens in this study. Flow pattern in dense and loose states of Ottawa sand were visualized with neutron radiography and tomography. Two types of sand with different grain shapes are used to evaluate the complex relationship between particle shape, initial assembly after controlled compaction effort, and multi-phase flow behavior as a function of target injection flow rate.

7.3 In-situ Flow Experiment through Compacted Sand

Experiment of in-situ flow through compacted sand was performed at NIST thermal neutron imaging beam line. Amorphous silicon detector with 250 μm spatial resolution (127 μm/pixel) was used. A simple water injection system as shown in Figure 7.1 was used to inject water through a compacted Ottawa sand specimen. Water was allowed to flow in three discrete steps at a relatively fast flow rate. Neutron tomography experiments were performed after each flow step to visualize the microstructure of dry sand specimen and its variation at the end of each flow step. Radiographs after each flow step are shown in Figure 7.2. A few tomography slices after flow step 2 is shown in Figure 7.3. Partially saturated region was observed near the flow wetting front while the area below has relatively uniform water distribution. The observation is similar to that of DiCarlo et al. (2010) where they observed larger number of pores filled with water for faster flow rate. The spatial resolution of the image was too coarse (~250 μm) to study at the grain/pore scale in detail. The experiment provided ideas for improvement of the experimental system and potential application at higher spatial resolution.

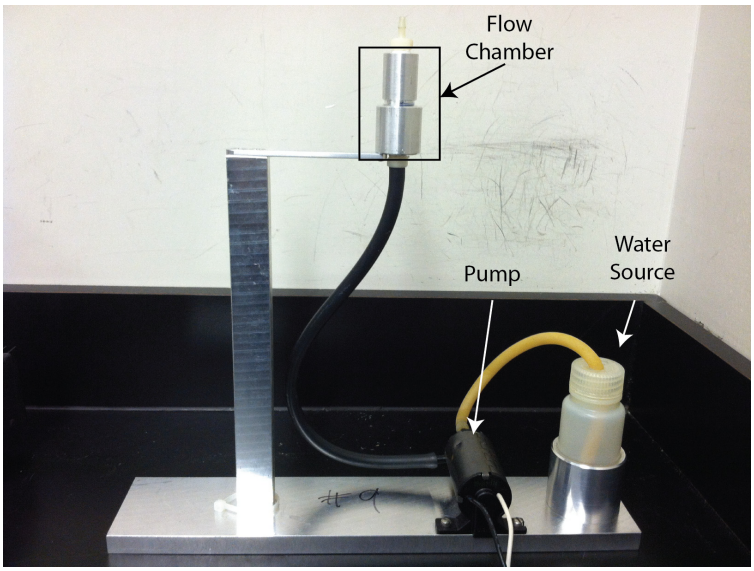


Figure 7.1: Water injection system used for in-situ imaging at NIST

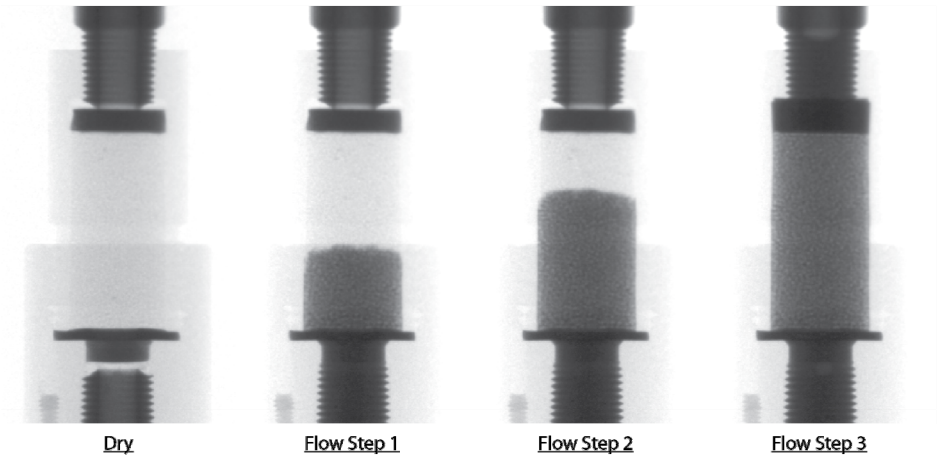


Figure 7.2: Radiographs after incremental water flow steps showing through thickness attenuation as a function of location

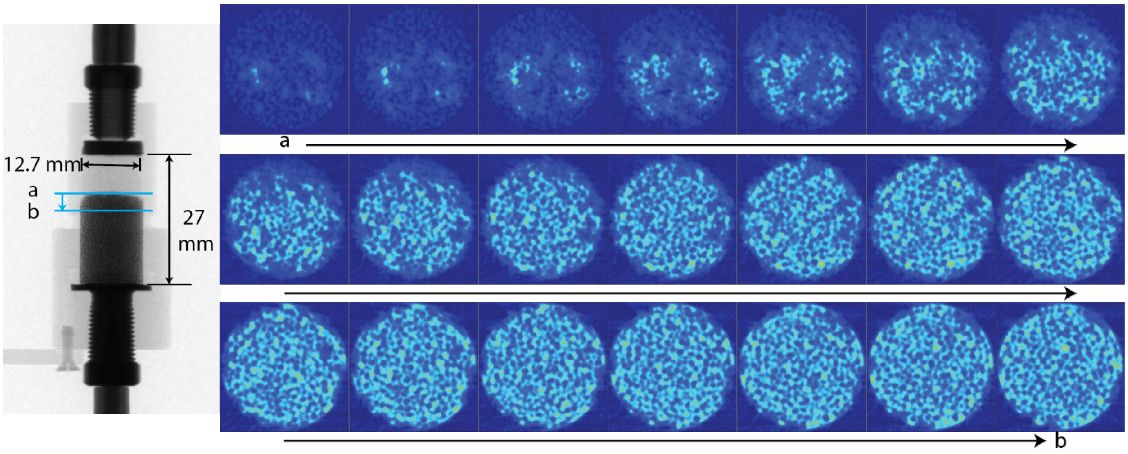


Figure 7.3: Example tomography slices at the flow front from top (a) to bottom (b) for the flow step 2

7.4 In-situ Flow Experiment through Dense and Loose States of Sand

7.4.1 Thermal neutron imaging at PSI

In-situ flow experiment was performed for dense and loose states of sand specimens at NEUTRA beam line of PSI to evaluate the dependency of pore size distribution and pore connectivity of identical granular medium. NEUTRA beam line has thermal neutron spectrum where the peak is at 25 meV. Slightly larger penetration depth through water is possible with thermal neutron compared to cold neutron (generally around 1 meV). Due to polychromatic spectrum, the average attenuation coefficient or total macroscopic cross section is measured at

different facilities. The average total macroscopic cross sections of water and penetration depth are compared for two different neutron imaging facilities with different spectrum in Table 7.1 where NEUTRA beam line has thermal neutron spectrum while CONRAD beam line at HZB has cold neutron spectrum. The actual size limit of the specimen depends on the pore geometry of the porous medium and water distribution.

Table 7.1: Average total macroscopic cross section of water (Σ_w) and penetration depth for 3% penetration at NEUTRA (thermal neutron) and CONRAD (cold neutron) beam line

Parameter	NEUTRA (Thermal)	CONRAD (Cold)
Total Macroscopic Cross Section of Water, Σ_w (cm^{-1})	3.6	5.1
Penetration Depth (cm)	0.974	0.688

7.4.2 Imaging Setup and Parameters

Intermediate spatial resolution (~50 μm/pixel) is available at the beam line with a field of view of 111.8 x 132.5 mm^2. The beam line also has an option of using X-ray imaging system for the same experimental setup by using 320 kV X-

ray source (XTRA) and corresponding scintillator screen suitable for X-ray. Both neutron and X-ray imaging system use the same detector system. The detector uses a configuration of lens coupled Andor neo scientific CMOS camera with a mirror and a scintillator. Nikon Nikkor 50 mm lens is used. Scintillator is switched for the neutron and X-ray imaging system. All imaging parameters of neutron and X-ray imaging are provided in Table 7.2. The experimental setup with flow chamber is shown in Figure 7.4.

Table 7.2: Neutron and X-ray imaging parameters used at PSI NEUTRA beam line

Parameters	Neutron	X-ray
Energy	Thermal (0.25 meV peak)	100 kV (100 keV max)
Pixel Size (μm)	51.76	51.76
Detector Array Size	2160 x 2560	2160 x 2560
Field of View (mm)	111.8 x 132.5	111.8 x 132.5
Exposure Time (s)	30	3
L/D	350	350
Scintillator Type	LiFZnS	CAWO OG4
Scintillator Thickness (μm)	50	~200 (estimate based on MTF)
Sample (center) to Detector Distance (mm)	35	35

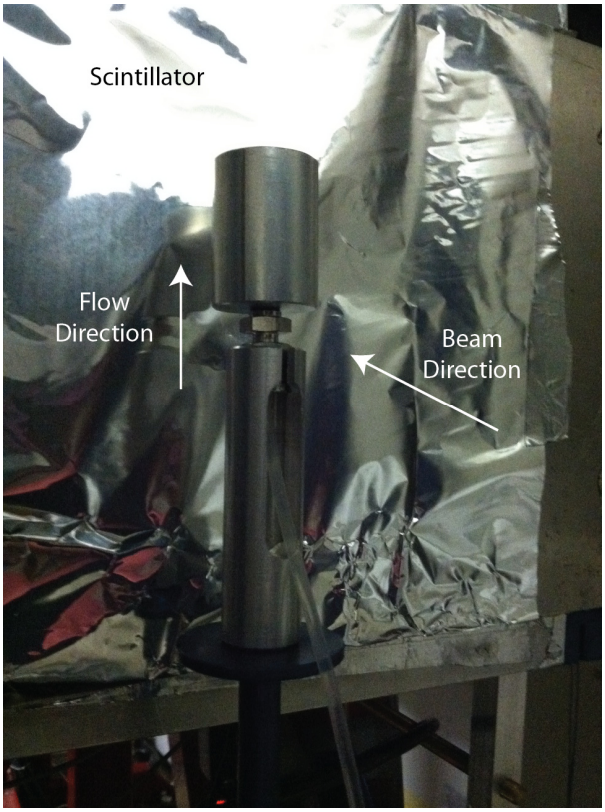


Figure 7.4: Experimental setup used at PSI NEUTRA beam line

During the initial setup, the lens coupled detector system is focused with optical light. Once the lens is focused, the scintillator is placed. PSI resolution target (Grunzweig et al. 2007) is then imaged with neutrons for the determination of spatial resolution corresponding to the setup used. The mask has lines of known width and spacing that are made with highly neutron absorbing gadolinium. An image used for optical focusing of the detector system and a neutron image of neutron resolution target developed at PSI is shown in Figure

7.5a and b respectively. Spatial resolution is determined from the resolution target directly. For the setup used here, the spatial resolution of neutron imaging was determined to be approximately 150 μm. Spatial resolution of the X-ray imaging system was not directly measured, but it can be estimated from scintillator Modulation Transfer Function (MTF) curve provided by the vendor which is the limiting factor in spatial resolution. The MTF curve for OG4 is shown in Figure 7.6. At MTF of 10%, approximately 200 μm spatial resolution is expected for X-ray imaging. The thickness of the scintillator is thought to be relatively thick designed for conversion of possible high energy X-rays (up to 320 keV).

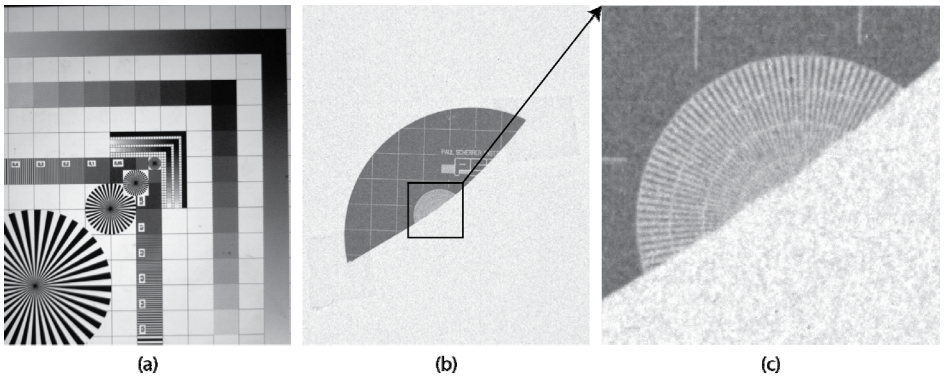


Figure 7.5: Optical image of focusing mask (a), Gd mask used for neutron resolution determination for a given set of imaging parameters (b), Gd resolution mask magnified (c)

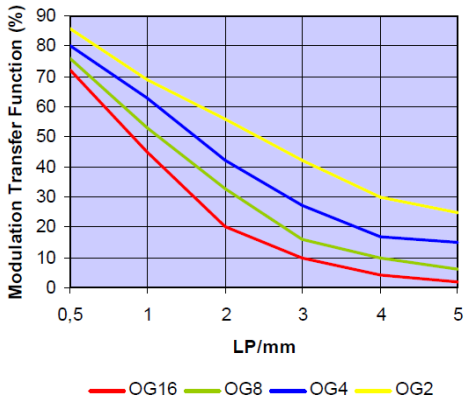


Figure 7.6: MTF of X-ray scintillator (OG4) (CAWO)

7.4.3 Specimen Preparation

Two specimens were prepared with Ottawa sand at dense and loose states. Relatively large field of view (FOV) allowed larger specimen size where the inner diameter is 19.12 mm and height is approximately 19.12 mm. The flow chamber is made out of aluminum. A filter paper is placed at the top and bottom of a stainless steel screen (# 60 mesh) to prevent the loss of sand particles during flow experiments and provide a uniform wetting front boundary. The top of sand specimen covered with a porous plastic which allows fluid (air/water) flow while keeping sand in place.

The sand specimen at dense state is prepared by placing dry sand in 3 layers. Each layer was compacted with a tamping rod in a similar fashion employed in proctor compaction mold. The sand specimen at the loose state was

prepared by using the technique proposed by Lade et al. (1998). The corresponding void ratios for dense and loose states are shown in Table 7.3.

Table 7.3: Measured void ratios of dense and loose sand specimens

Specimen	Void Ratio
Ottawa Dense	0.52
Ottawa Loose	0.74

7.4.4 Flow Experiment Parameters

A controlled flow rate of 0.33 µl/sec was used for water injection into the flow chamber containing compacted sand specimen. Water was injected at 3 discrete steps from bottom to top, and the volume of water injected is shown in Table 7.4. During the water injection step, time-lapsed radiography was taken to monitor in-situ water flow pattern. For time-lapsed radiography, 2 x 2 binning was used to reduce the exposure time to 15 sec. After each water injection step, neutron tomography was taken. After completion of neutron tomography, X-ray tomography was additionally obtained for the dense Ottawa sand specimen for dual-modal contrast comparison. For neutron tomography, 30 sec exposure time was used for each of 1025 projections covering 180 degrees. For X-ray tomography, 2 sec exposure time was used for 1025 projections.

Table 7.4: Parameters used for the flow experiment through sand specimens prepared in dense and loose states

Parameter	Dense	Loose
Bulk Density (g/cm^3)	1.74	1.53
Pore Volume (cm^3)	1.84	2.24
Flow Rate (µl/sec)	0.33	0.33
Injected Water Volume for Flow Step 1 (cm^3)	0.6	0.6
Injected Water Volume for Flow Step 2 (cm^3)	0.6	0.6
Injected Water Volume for Flow Step3 (cm^3)	0.8	0.8

7.4.5 Dual Modality

The dual-modal contrast of neutron and X-ray imaging results are presented in Figure 7.7 using example radiographs and reconstructed tomography slices at identified location for different flow steps. High contrast from water phase is clearly revealed with neutron imaging. It is shown that the spatial resolution of X-ray images was much coarser than that of neutron images. As a result, neither the pore structure or water distribution can be identified with X-ray images.

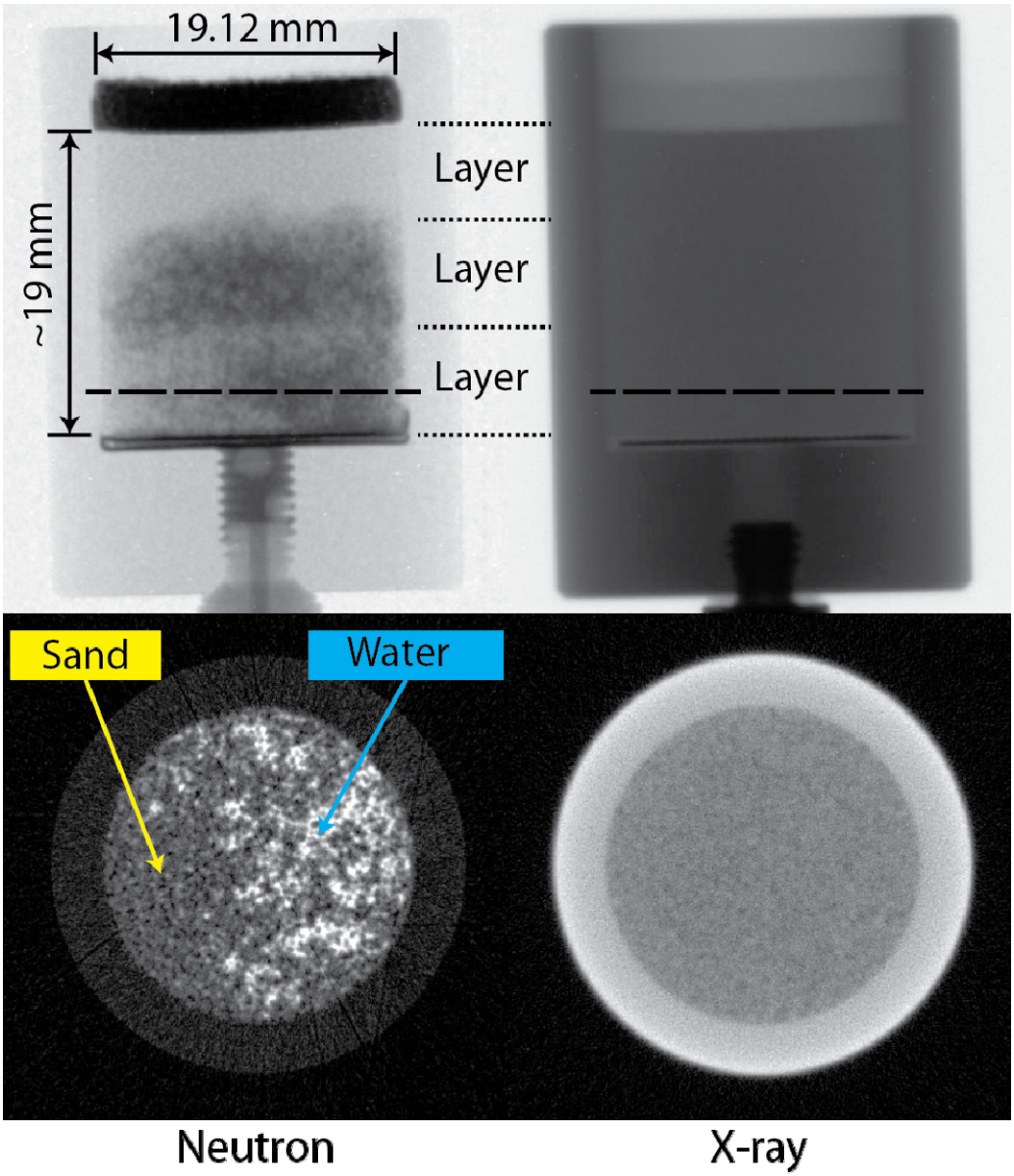


Figure 7.7: Dual-modal (neutron and X-ray) contrast of Ottawa dense specimen at flow step 1 shown from radiographs and reconstructed tomography slices

7.4.6 Flow Results

Time – lapsed radiographs for Ottawa sand corresponding to dense state of compaction for flow steps 1, 2 and 3 are shown in Figure 7.8, Figure 7.9, and Figure 7.10 respectively. Water was injected using the flow pump at controlled an very slow rate of 0.33 μm/sec into the sample through a port connected at the center of the bottom face of the sample. Water entered the sample through filter paper which has very high in-plane transmissivity. Thus the boundary condition corresponds to providing access for porous sand medium to simultaneously be in contact with wetting water front for the entire bottom face of the sample. It is interesting to note that bottom right corner seems to have initiated the water diffusion through porous network. Based on the injection flow rate, expected rise of water front without considering capillary rise is 0.2 mm/min. Yet the observed is much faster (~0.93 mm/min) and is due to capillary rise which is a function of pore entry size.

It also shows that water flows laterally along the interface between compaction layers. It shows that possible anisotropy caused by the compaction process affected the water flow pattern. In flow step 1, water initially moved up to the first and second compaction layer very quickly and spreads laterally. More water entered and diffused through the middle compaction layer than the bottom compaction layer. In the flow step 2, water have saturated already wet porous media from the flow step 1 and more fully fill the pores in the bottom compaction

layer eventually reaching the top compaction layer after the flow step 3. As shown with the arrows, the major flow direction in lateral direction. In the flow step 3, water first filled up most of the pores in the sand specimen before it finally moves up through the porous plastic.

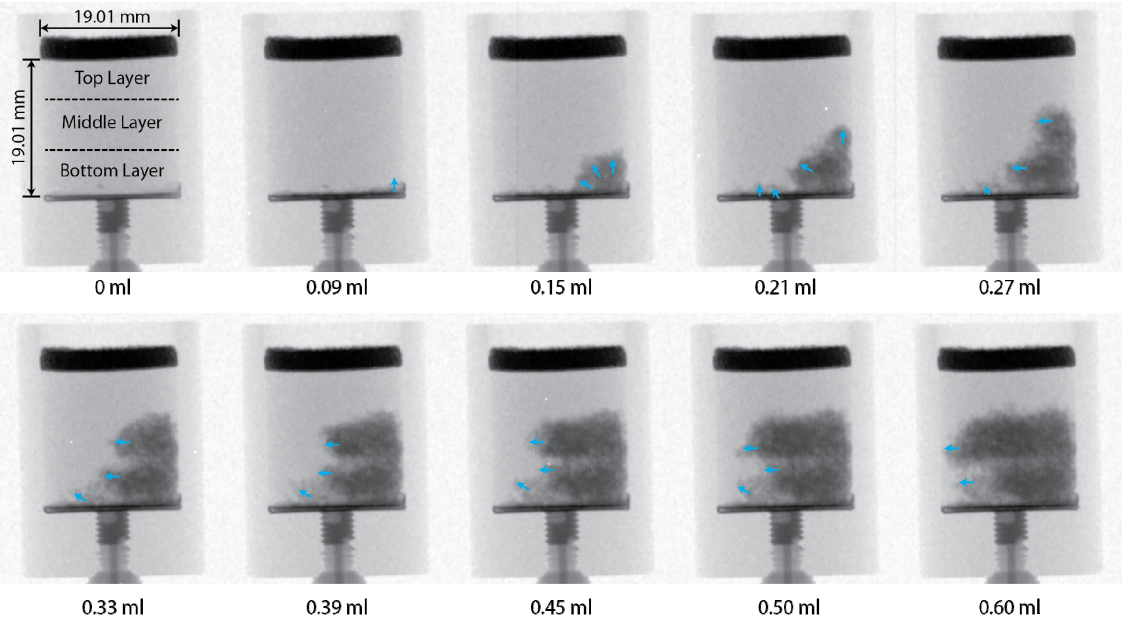


Figure 7.8: Time-lapsed radiographs of flow step 1 of Ottawa sand at dense state

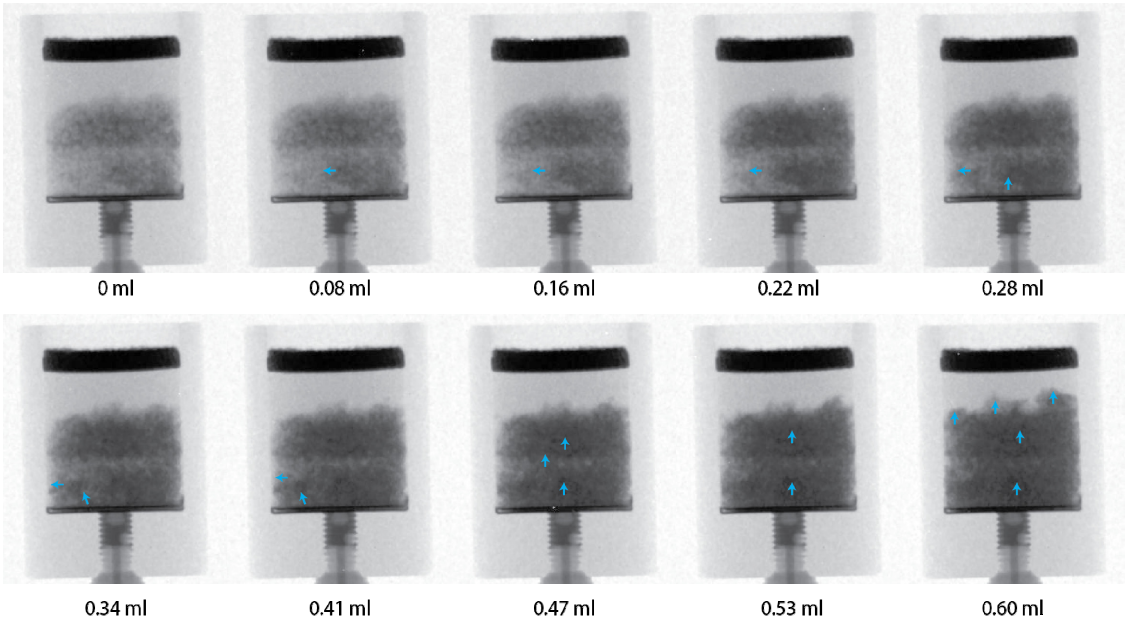


Figure 7.9: Time-lapsed radiographs of flow step 2 of Ottawa sand at dense state

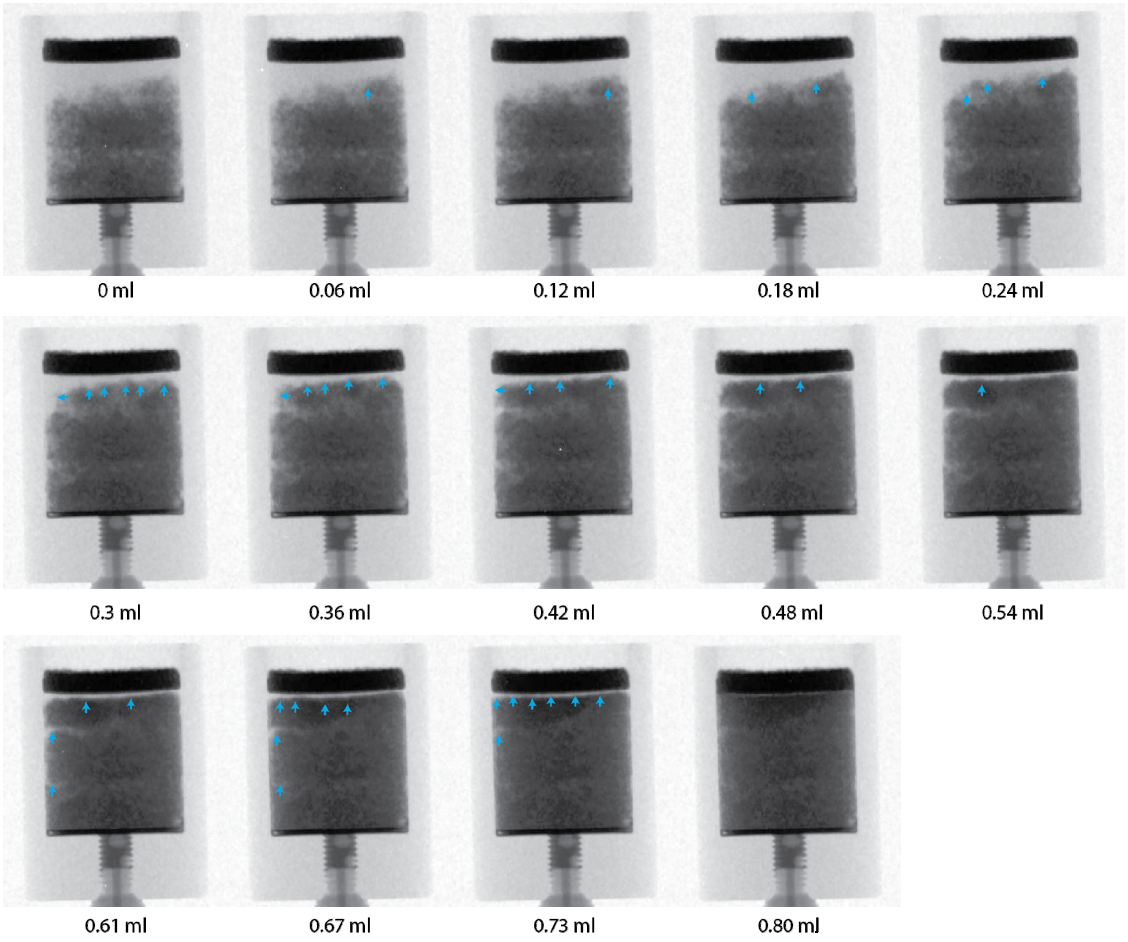


Figure 7.10: Time-lapsed radiographs of flow step 3 of Ottawa sand at dense state

Corresponding time – lapsed radiography results for Ottawa sand which is initially in loose state are shown in Figure 7.11, Figure 7.12, and Figure 7.13 respectively. For the same amount of water used in the dense state, water flow pattern was very different from that of the dense state. Due to lack of anisotropy in the structure, water was able to spread out more isotropically as indicated by

the arrows. Once water hits the container boundary, boundary effects limits the water flow direction.

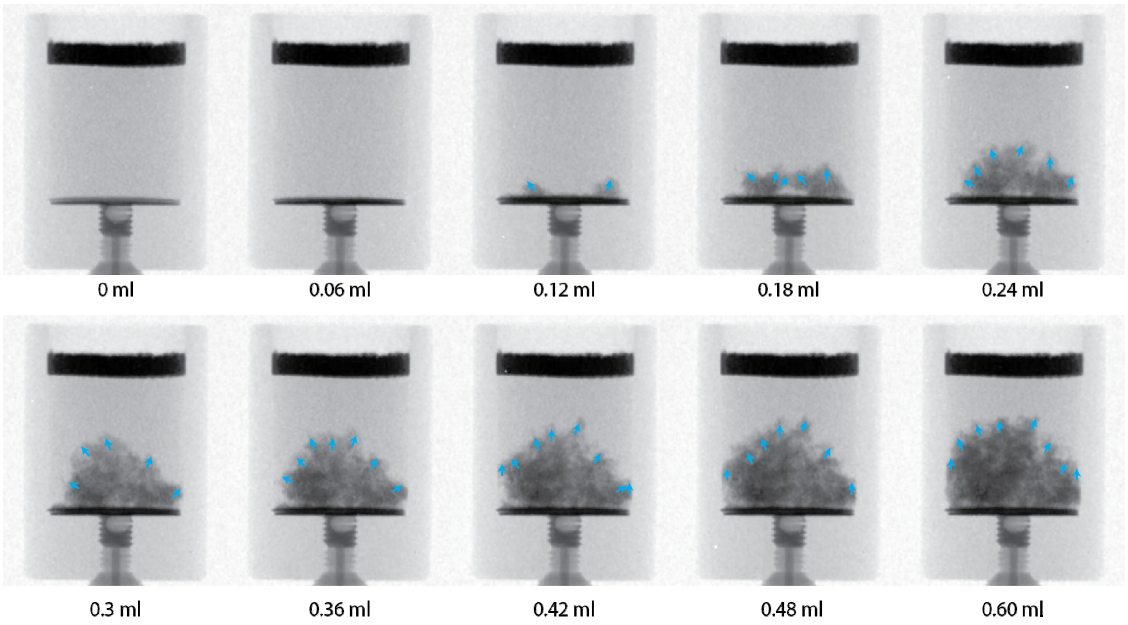


Figure 7.11: Time-lapsed radiographs of flow step 1 of Ottawa sand at loose state

.

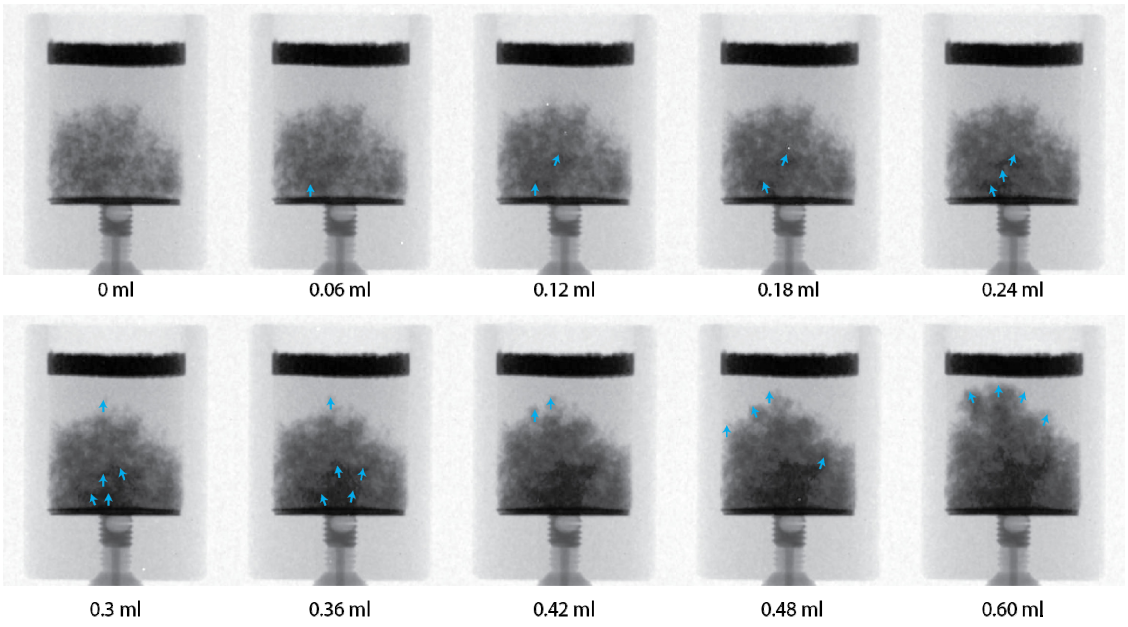


Figure 7.12: Time-lapsed radiographs of flow step 2 of Ottawa sand at loose state

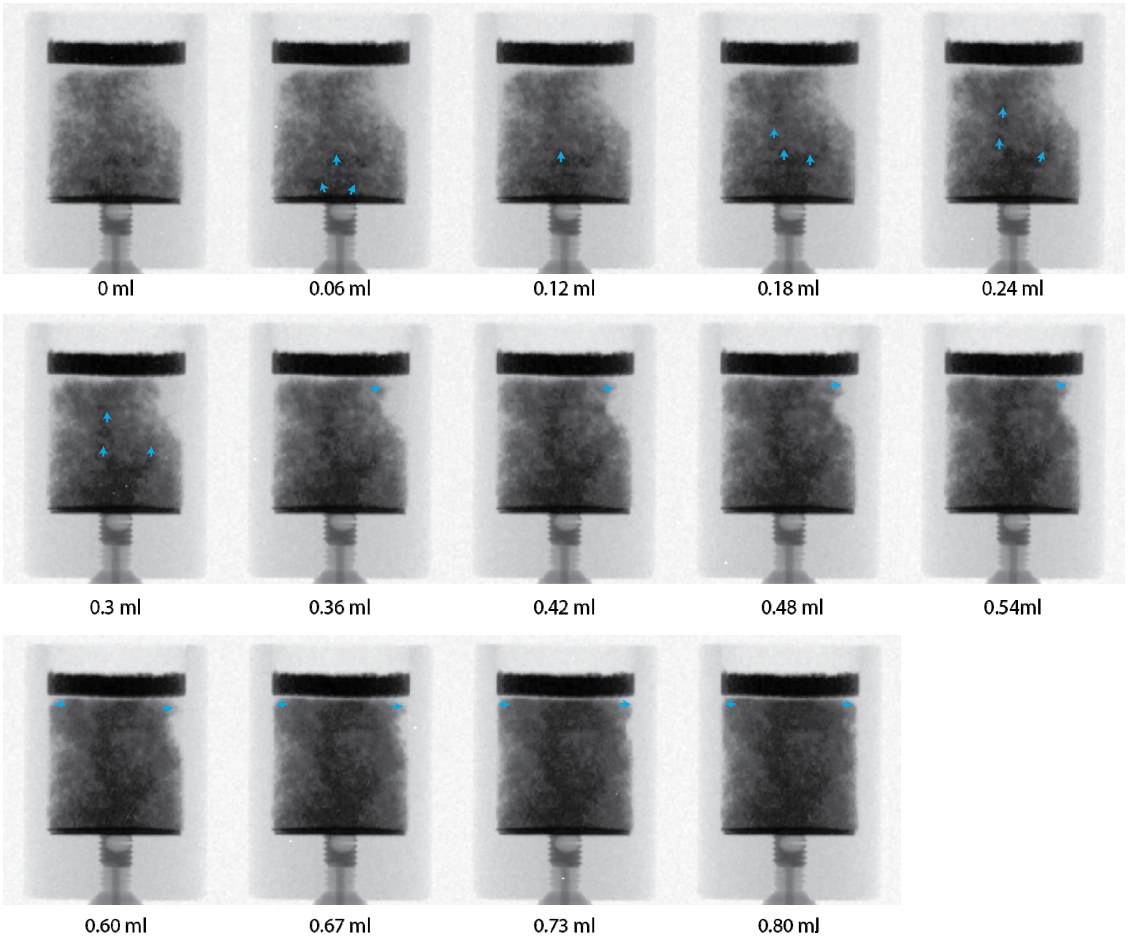


Figure 7.13: Time-lapsed radiographs of flow step 3 of Ottawa sand at loose state

Radiographs showed information about water flow pattern, but it is only showing the information integrated through the thickness. The three dimensional information can be shown from tomography taken after each flow step. Cross sectional water distribution patterns of the dense Ottawa sand specimen are shown from reconstructed tomography slices from top, middle and bottom

compaction layer for flow step 1,2 and 3 are shown in Figure 7.14. It shows that the compacted sand is only partially saturated in bottom and middle layers for the flow step 1. In flow step 2, majority of the pore is filled with water in the bottom and middle layer, and water infiltrated to the top compaction layer. In flow step 3, pores in bottom and middle compaction layers are even more saturated with water than flow step 2.

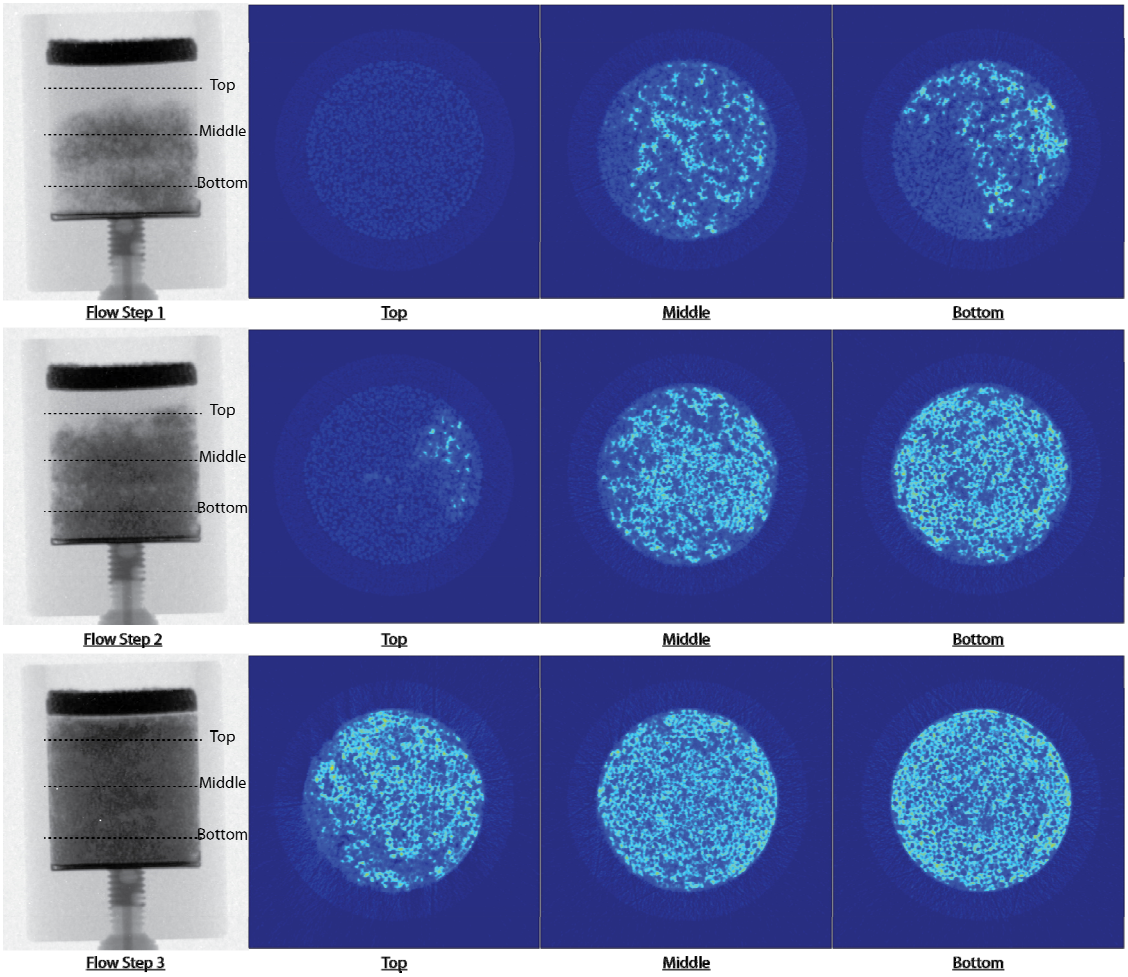


Figure 7.14: Cross-sectional water distribution pattern of dense Ottawa sand specimen shown from reconstructed tomography slices from top, middle and bottom compaction layers for flow steps 1, 2 and 3

Cross sectional water distribution patterns of the loose Ottawa sand specimen are shown from reconstructed tomography slices from top, middle and bottom compaction layer for flow step 1,2 and 3 are shown in Figure 7.15. The reconstructed slices show the cross sectional water flow pattern that is difficult to infer from 2D radiographs. Compared to the dense state, the water distribution is rather sparse. As shown in flow step 3, more unfilled pores are observed in the middle and bottom area compared to similar location in the dense Ottawa sand specimen despite the fact that water still reached the top of the specimen.

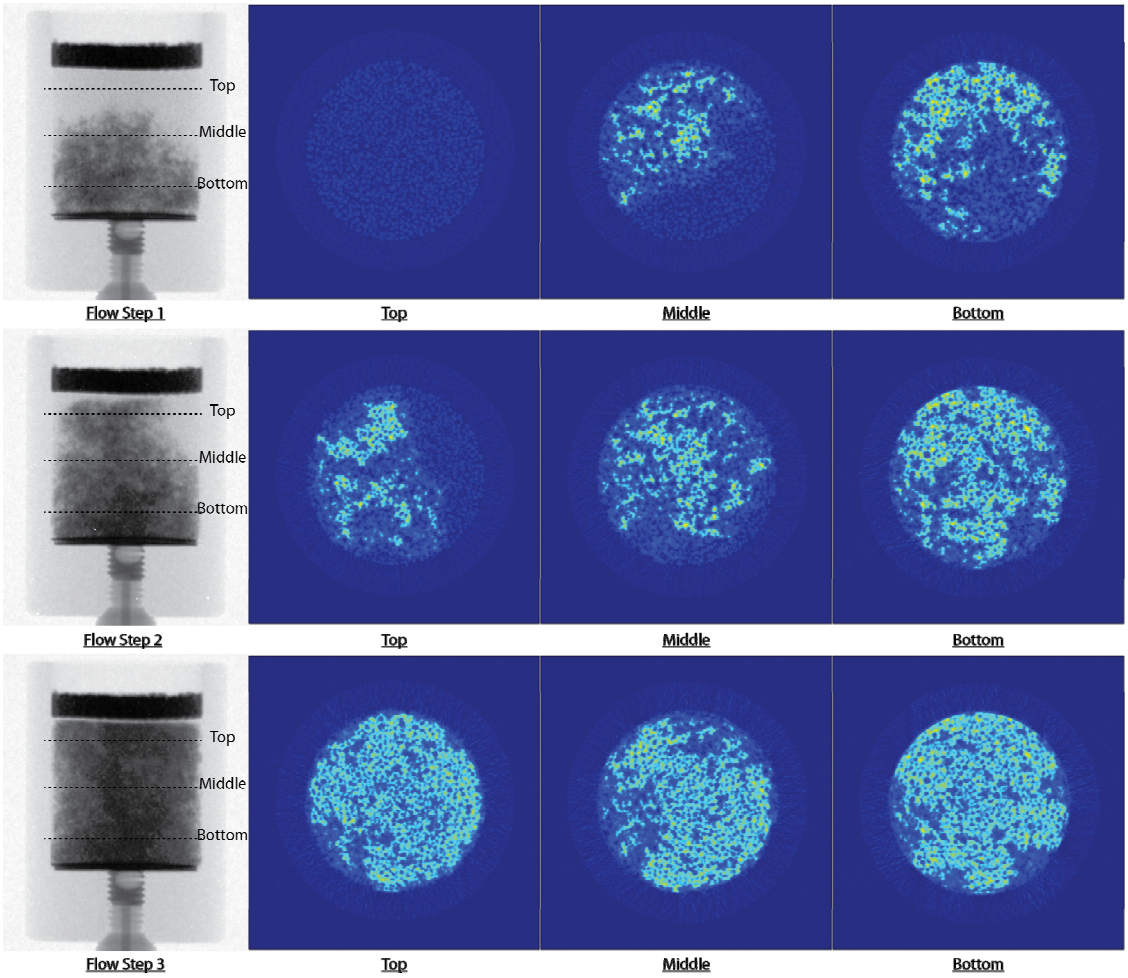


Figure 7.15: Cross-sectional water distribution pattern of loose Ottawa sand specimen shown from reconstructed tomography slices from top, middle and bottom location of the specimen for flow steps 1, 2 and 3

7.5 High Resolution In-situ Flow Experiment though Compacted Sand Specimens using Cold Neutrons

7.5.1 High Resolution Neutron and X-ray Imaging

For pore/grain scale analysis, sequential use of high resolution X-ray and neutron imaging systems were implemented at CONRAD beam line of Helmholtz-Zentrum-Berlin (HZB), Germany based on the idea of dual-modal contrast of three phases of soil (Kim et al. 2013). Information of initial pore structure is revealed with high resolution X-ray tomography, and water flow pattern is identified with high resolution neutron tomography. HZB has a dedicated neutron imaging beam line, and also there is also a micro-focus X-ray tomography system available. A very high resolution (~6.5 μm/pixel) neutron imaging system was used for this research (Williams et al. 2012). Related imaging parameters are shown in Table 7.5.

Table 7.5: X-ray and neutron imaging parameters used at HZB

Modality	X-ray	Neutron
Energy (keV)	70 (max)	7.30×10^{-6} (peak)
Voxel Size (μm)	6.9	6.5
FOV (mm x mm)	16.1 x 16.1	13.3 x 13.3
Number of Projections	1000	600
Frames/Projection for Tomography	3	2
Tomography Exposure Time (sec)	1.7	20
Radiography Exposure Time (sec)	N/A	10

7.5.2 Specimen Preparation

In this experiment, compacted sand specimens at target density prepared in aluminium cylindrical flow chamber custom developed for use at high resolution in-situ imaging as shown in Figure 7.16a. Due to limited size of FOV (13.3 mm x 13.3 mm), the chamber was designed to have inner dimension of 10.27 mm (dia.) x 10.27 mm (height). A stainless steel screen (#60 mesh) was placed at the bottom of the chamber for structural support, and filter papers were placed on top and bottom of the stainless steel screen placed to prevent the loss of sand particles during flow experiments and provide a uniform wetting front boundary. Two compacted sand specimens are prepared in dense state by using two different types of sand with different grains shapes: Ottawa sand (round) and

Q-ROK sand (angular). Sand was placed about an equal amount (0.5 g each layer for Ottawa sand and 0.44 g each layer for Q-ROK sand) in 3 layers. Each layer was compacted by dropping a tamping rod 25 times. Porous plastic was placed on top of sand specimen to allow fluid (air/water) flow while keeping the sand particles in place. Water flow is maintained by a syringe pump which is remotely controlled from outside of the neutron imaging beam line as shown in Figure 7.16b.



Figure 7.16: Aluminum flow chamber (a) and syringe pump (b)

7.5.3 Experimental Procedure

Once the specimens are prepared, X-ray tomography was performed to obtain the initial dry microstructure of the compacted sand specimen. The

specimen was then carefully moved to the neutron imaging beam line which was located in the neighboring building. The experimental setup at neutron imaging beam line is shown in Figure 7.17. At first, a neutron tomography of the dry specimen was taken which will be used to compare and register with the initial structure obtained by using X-ray tomography. Then, water was allowed to flow at a controlled flow rate (0.033 µl/sec). This flow rate is 10 times slower than the flow rate used at PSI described in previous section. The experimental parameters are shown in Table 7.6.

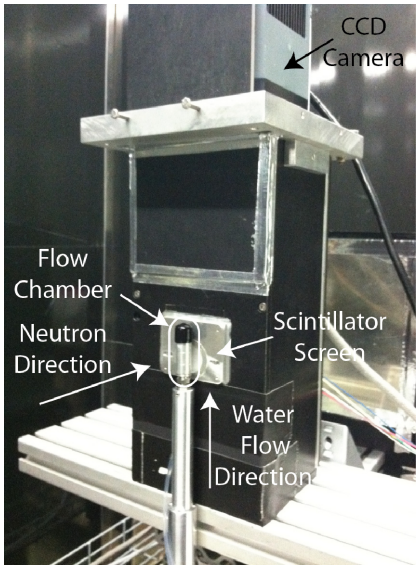


Figure 7.17: Experimental setup used at CONRAD neutron imaging beam line

Table 7.6: Water injection parameters for Ottawa sand and Q-ROK sand specimens

Parameter	Ottawa Sand	Q-ROK Sand
Bulk Density	1.81 g/cm^3	1.64 g/cm^3
Pore Volume	0.260 cm^3	0.305 cm^3
Void Ratio	0.460	0.612
Flow Rate	0.033 µl/sec	0.033 µl/sec
Injected Water Volume (Flow Step1)	0.064 cm^3	0.065 cm^3
Injected Water Volume (Flow Step2)	0.058 cm^3	N/A

Time-lapsed dynamic radiographies for one fixed view angle were taken during water injection stage with 10 sec exposure time. After completion of the first injection phase, water was allowed to equilibrate for approximately 2 hours and then the neutron tomography of the flow step 1 was completed. This was followed by a second flow step for the Ottawa sand specimen. For neutron tomography, 2 frames were taken per view angle to remove gammas detected on the thin gadox scintillator used for obtaining very high resolution imaging corresponding to 6.5 µm pixel size. The minimum value at each pixel of the two digital images was used as a criterion to remove higher intensity gammas which are usually detected randomly due to background gamma radiation in an enclosed hutch required for shielding. Spatial median filter (3×3) was additionally

applied to remove any bright spots from remaining gamma radiation since it is possible to have detected gammas at the same pixel location for the 2 images taken.

7.5.4 Dual Modality and Image Registration

X-ray tomography of initial dry state and neutron tomography of initial dry state were registered by using cross-correlation. For dry sand, both X-ray and neutron images show similar contrast, and cross-correlation of attenuation intensities is suitable instead of using more computationally intensive mutual information based registration presented in Chapter 5. The procedure is implemented using Avizo 7 visualization software. Since the neutron tomography data of flow steps are in the same location as that of dry neutron tomography data, X-ray tomography of dry state can be directly compared with neutron flow step 1 and 2 data after registration is performed. The registered result is shown in Figure 7.18 for the full Ottawa sand specimen, and a smaller region of interest (ROI) volume is considered in Figure 7.19. A close registration of X-ray and neutron tomography data was achieved. The initial microstructure can be obtained from the X-ray tomography data with, and water phase distribution can be shown from the neutron tomography data.

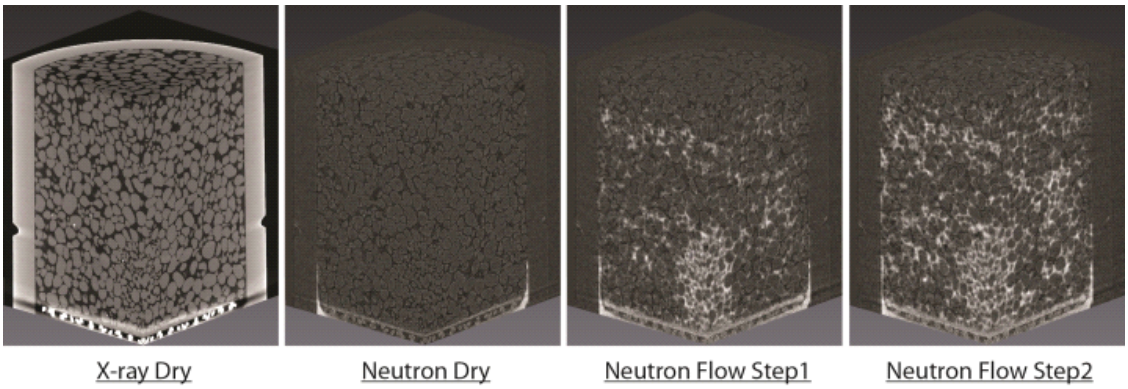


Figure 7.18: Three dimensional view of X-ray tomography data of the dry state, neutron data of the dry state, flow step 1, and flow step 2 of Ottawa sand at dense state

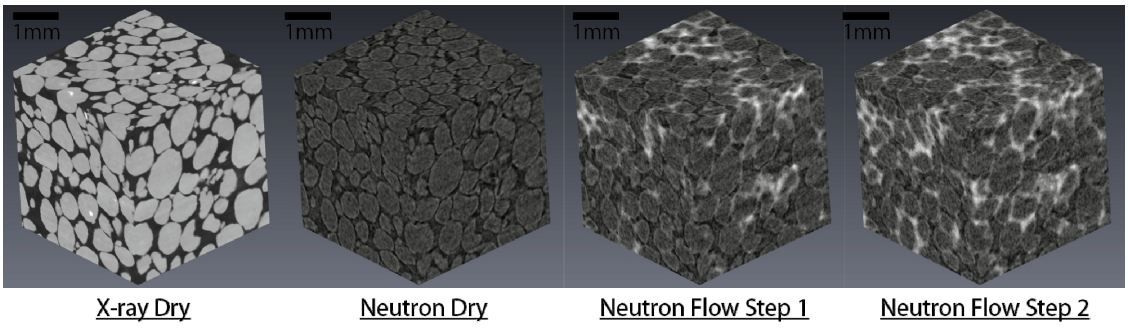


Figure 7.19: Dual modality contrast comparison of X-ray and neutron images and quality of image registration shown from small ROI volumes

7.5.5 Time-lapsed Radiography

Time-lapsed radiographs of the flow step 1 of the dense Ottawa sand specimen are shown in Figure 7.20. The controlled flow rate (0.033 µl/sec) advanced the water at capillary flow regime, and the water flow patterns are shown in the radiographs. The amount of water allowed to flow for this injection sequence amounted to less than 25% of the entire pore volume, and the radiographs show that water has advanced to the top of the sand specimen largely based on capillary fingering.

When water first entered the dense Ottawa sand specimen, a very fast capillary rise of water (~4.5 mm/min) was observed through the middle of the specimen. The rise was high enough to reach the middle compaction layer. Then, water moved in the lateral direction along the middle compaction layer. Once water reached the top compaction layer, water flowed laterally again between the compaction layer interfaces.

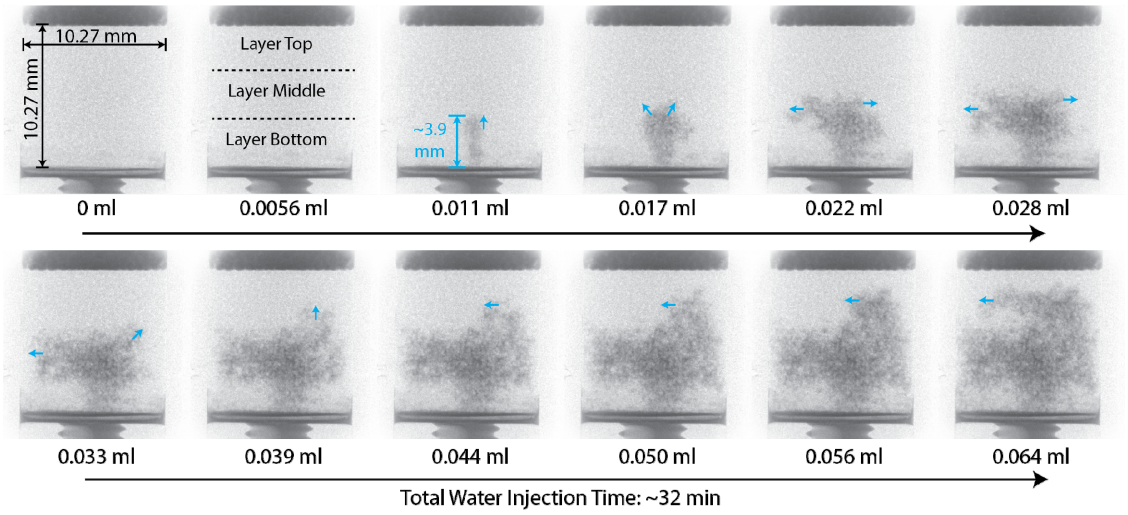


Figure 7.20: High resolution time-lapsed neutron radiographs of flow step 1 of Ottawa sand specimen in dense state

Time-lapsed radiographs of the flow step 2 of the dense Ottawa sand specimen are shown in Figure 7.21. In the second flow step, water first seems to follow the initially wetted area from the first flow step while spreading to the neighboring unfilled pores. Top and middle compaction layers are visible from the radiographs, but the area where water initially entered is visible from the bottom compaction layer. The result indicates that there is slightly different structure causing the flow pattern.

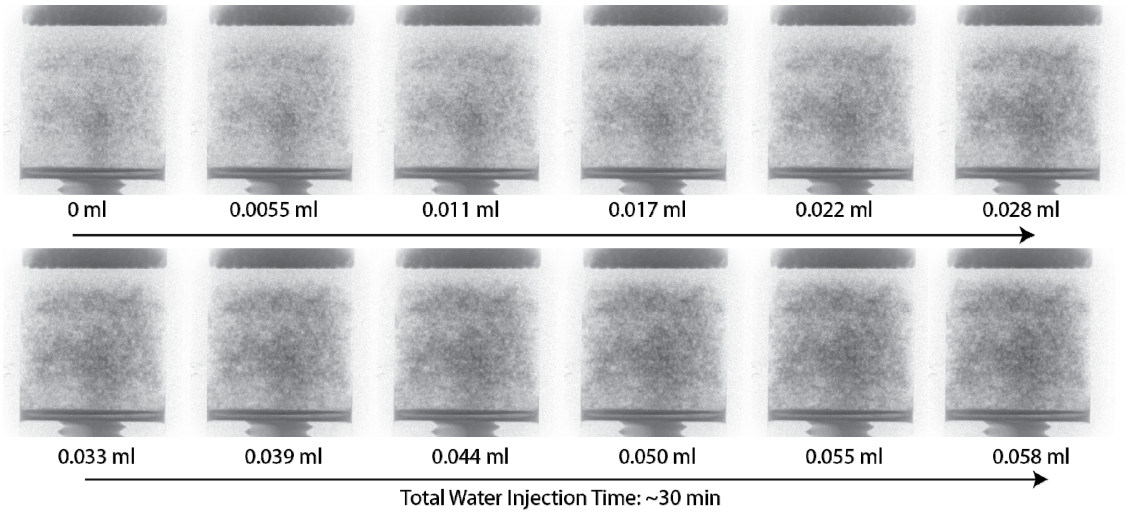


Figure 7.21: High resolution time-lapsed neutron radiographs of flow step 2 of Ottawa sand specimen in dense state

The time-lapsed radiographs of flow step 1 of the dense Q-ROK sand specimen is shown in Figure 7.22. It shows that water saturated the bottom layer before saturating the middle and top compaction layers. Lateral movement of water was also observed at the bottom, middle and top compaction layers. The location of each layer is visible from the flow radiography results. Flow step 2 was not performed for the Q-ROK sand specimen due to time constraints associated with access to neutrons for this beam cycle.

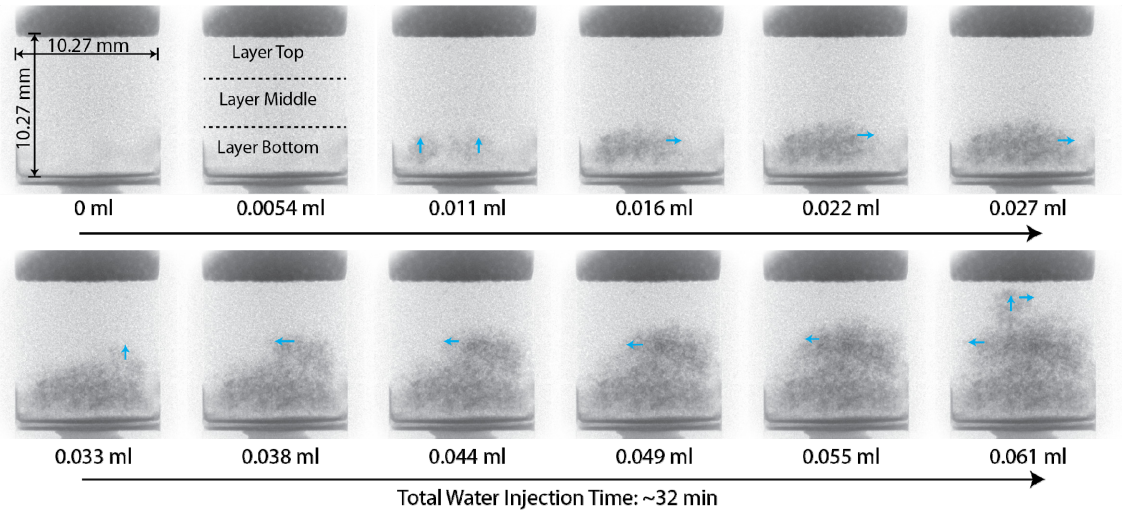


Figure 7.22: High resolution time-lapsed neutron radiographs of flow step 1 of Q-ROK sand specimen in dense state

7.5.6 Pore Size Distribution and Capillary Rise

Pore size and pore size distribution play important roles with capillary forces of fluid flow. The local pore size distribution is investigated in this section. Pore size distribution of the entire volume of the dense Ottawa sand specimen is measured by using image morphological opening algorithm, and corresponding cumulative pore size distribution is shown in Figure 7.23. The typical pore size parameters (D_{10}, D_{50} and D_{90}) used in geomechanics community are shown from these curves. The Ottawa sand specimen in dense configuration presented interesting flow pattern shown from 2D dynamic radiographs and 3D tomography data visualization. It was observed that water had migrated through the area in

the center of the specimen in the bottom compaction layer. It was also visually observed that the area where water flow initiated had smaller grain/pore sizes where capillary pressure influence is higher. This observation was confirmed by quantitatively measuring pore size distribution of the area and compare with the area directly above as well as the entire volume as shown in Figure 7.24. The location of initial water capillary flow path was identified from neutron tomography data of the flow step 1. The exact same location was found from the X-ray tomography data due to image registration of X-ray and neutron data. Based on the segmented X-ray data, pore size distribution is measured. In Figure 7.24, it shows that the ROI (a) where water initially entered the sand specimen at the bottom had smaller pore size compared to other ROI (b) and the entire volume (c). The ROI (b) and (c) had a very similar pore size distribution. It shows that the ROI with smaller pores (a) had affected water to initially flow through the area instead of other areas.

Table 7.7: Dimensions of ROIs used for analysis of pore size distribution and their porosity values

ROI	Size (voxel)	Size (mm^3)	Porosity
a	351 x 351 x 521	2.44 x 2.44 x 3.62	0.320
b	351 x 351 x 521	2.44 x 2.44 x 3.62	0.321
c	1600 x 1600 x 1421	11.1 x 11.1 x 9.87	0.315

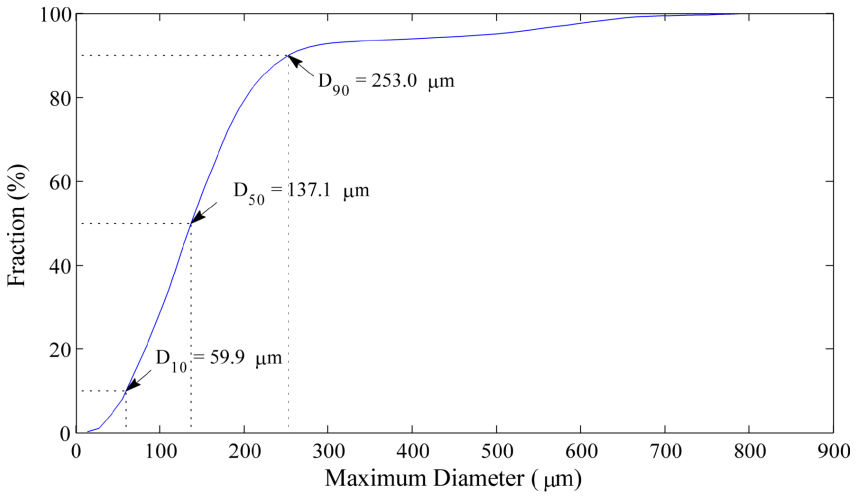


Figure 7.23: Cumulative pore size distribution of the dense Ottawa sand specimen

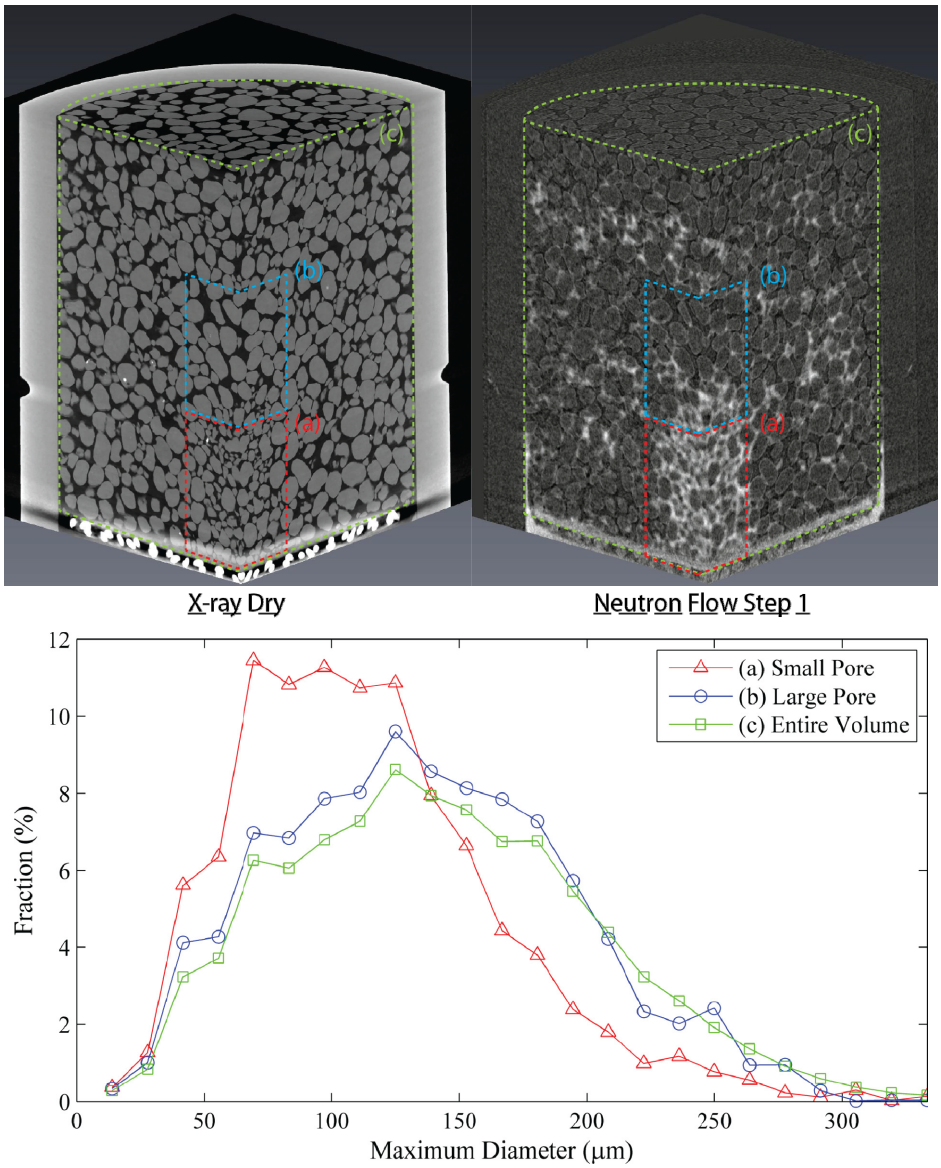


Figure 7.24: Comparisons of pore size distribution of different ROIs (small pore volume (a), large pore volume (b), and entire volume (c))

7.5.7 Degree of Saturation along Height of the Specimen

The neutron and X-ray tomography data was analyzed quantitatively by binarizing voxels using suitable thresholding techniques to obtain volumes of water and pore space respectively. Based on the segmented results, the degree of water saturation along height of round Ottawa sand and angular Q-ROK sand specimens in dense states are provided in Figure 7.25 and Figure 7.26 respectively. It shows that water saturation values are varying along the height of the specimen. Abrupt changes of the degree of saturation are noticed at the interface of the three compaction layers. This is quite clear with the Q-ROK sand specimens and this indicates that the compaction layers had important influence on the water flow patterns. The degree of saturation pattern is similar for flow step 1 and 2 of Ottawa sand specimen, it can be inferred that water saturates more completely around the area where water has initially wetted during the flow step 1.

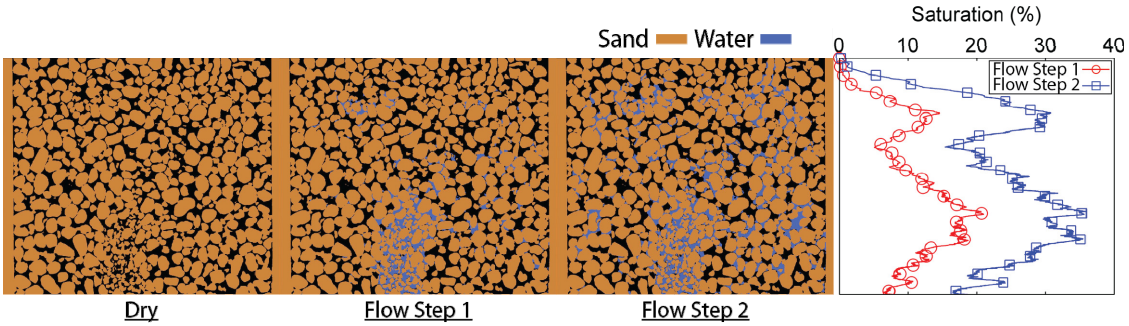


Figure 7.25: The degree of saturation along the height of the specimen for flow steps 1 and 2 of Ottawa sand (round) specimen in dense state

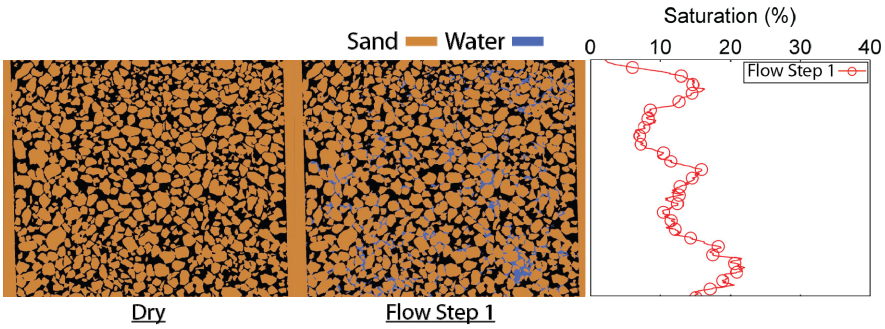


Figure 7.26: The variation of local saturation along the height of the specimen for flow steps 1 of Q-ROK sand (angular) specimen in dense state

7.5.8 Full Morphology Imbibition Simulation

The flow rate of the water was chosen such that the capillary forces are dominant. Since the capillary force depends on the radius of the pore, geometric

data of pore size distribution is used to approximate water distribution for different saturation values. This is a so-called full morphology approach which was introduced by Hilpert and Miller (2001) in order to simulate the drainage or imbibition process. The full morphology method for simulation of drainage condition is explained in Chapter 6. The full morphology simulation for imbibition is very similar to that for drainage. The technique estimates stationary distribution of two fluid phases (wetting and non-wetting) and corresponding capillary pressure. It applies a combination of morphological opening algorithm for phase distribution simulation and Young-Laplace equation for capillary pressure estimation shown earlier in equation 6.2. At each morphological opening step, connectivity check to wetting phase reservoir is performed. The wetting phase reservoir is located at the bottom of the specimen, and the non-wetting phase reservoir is located at the top of the specimen. In this case, a contact angle of 60° was assumed for water with silica sand. The simulation was performed by using GeoDict software (www.geodict.com). The advantage of the full morphology model is its relatively easy implementation and low computational resource requirement. Therefore, one can use it to simulate the phase distribution for large 3D images. An example capillary pressure saturation curve and water distribution is shown in Figure 7.27 for Ottawa sand specimen in dense state. Based on experimental parameters, the saturation of the specimen after injection of water was found to be about 0.246. The simulated two phase

distributions at similar saturation levels (0.223 and 0.265) are compared to actual experimental imaging result in Figure 7.28. A fusion image of X-ray and neutron data is shown for easier identification of water, air and solid phases. Full morphology method is largely based on the pore size and connectivity, and a good agreement between simulation result and experimental result was obtained.

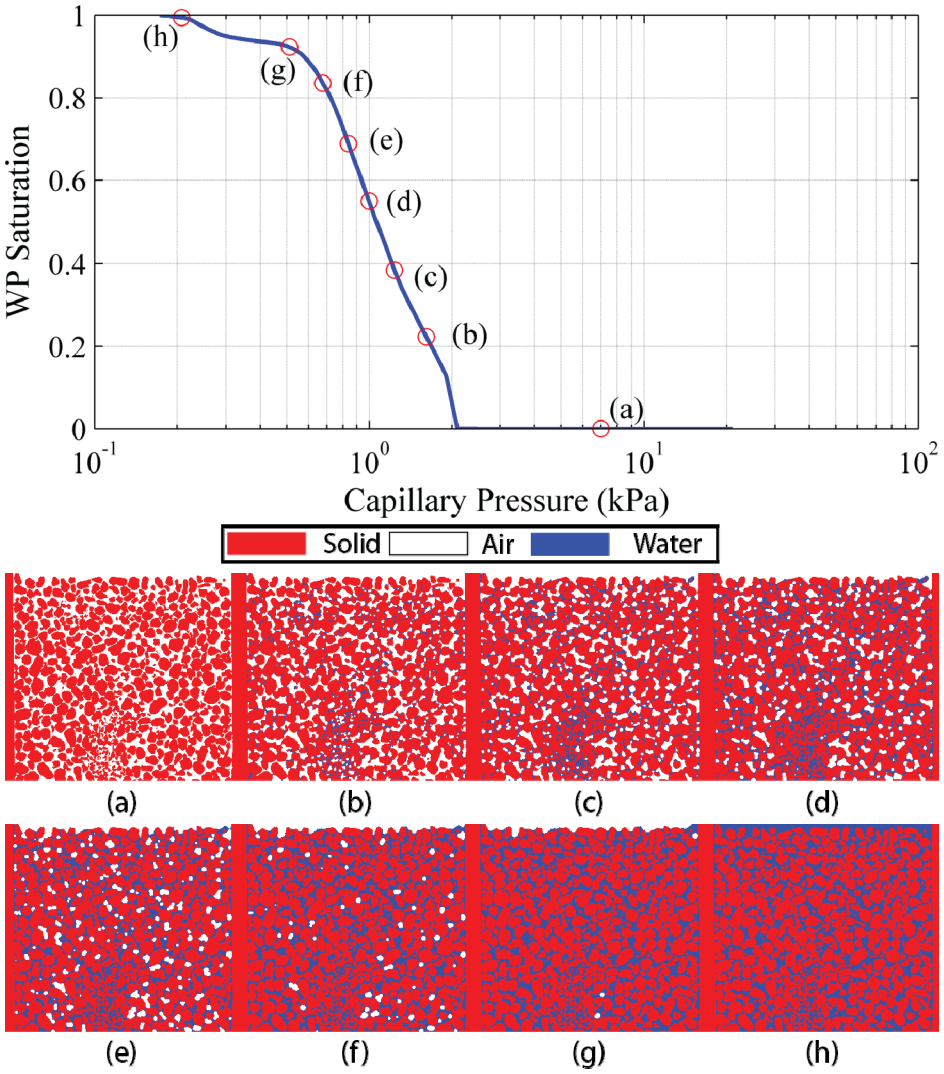


Figure 7.27: Simulated capillary pressure – saturation curve and solid (red), water (blue) and air (white) distribution by using full morphology method for Ottawa sand specimen in dense state

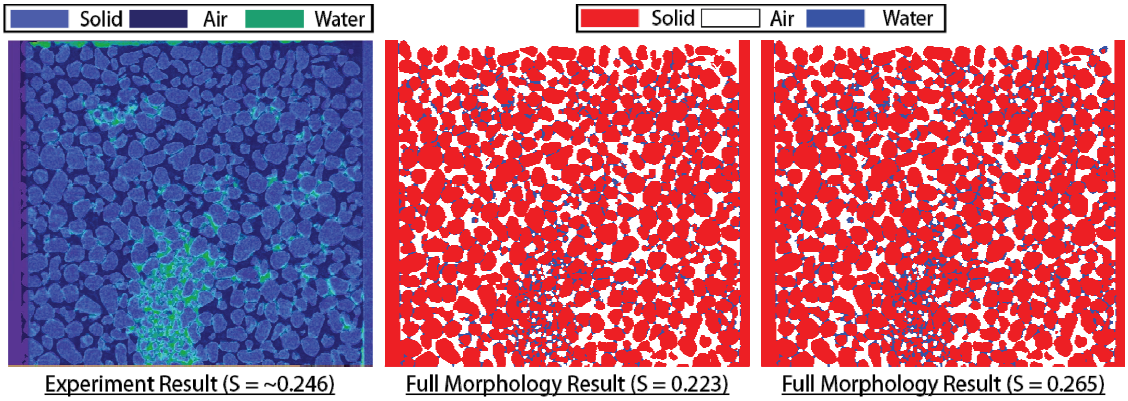


Figure 7.28: Neutron and X-ray super-positioned image compared with simulated two fluid phase distribution at similar saturation level

7.6 Conclusions

In-situ imaging experiments of flow through sand specimens with different initial microstructure were performed by using neutron radiography and tomography were presented at different neutron imaging facilities. The flow advancement was visualized by using neutron time-lapse radiography, and the flow pattern after the injection was visualized from the neutron tomography result. At NIST, coarse spatial resolution thermal neutron imaging was performed for a dense compacted sand specimen. Capillary fringe region was visualized at the top of the flow front. At PSI, specimens with different initial states (dense and loose) of Ottawa sand flowed at a controlled flow rate. Different flow patterns were observed due to different initial structure where compaction layer of dense

state affected lateral flow along the compaction layers and more isotropic flow pattern observed in the loose state. At HZB, sequential use of high resolution X-ray and neutron imaging was performed to obtain both the initial microstructure and flow pattern with a good contrast. The experimental results indicated the importance of pore size on flow pattern. The effect of compaction layer on degree of saturation was also presented. The imbibition process was simulated by using full morphology approach based on the pore geometry obtained from X-ray tomography. The simulation result was directly compared with the imaging experimental results, and a good agreement was obtained. The combined use of neutron and X-ray tomography data was implemented for comprehensive analysis of material microstructure and shows a lot of promise of generalizing this technique for other materials.

7.7 References

Carminati, A., Kaestner, A., Ippisch, O., Koliji, A., Lehmann, P., Hassanein, R., Vontobel, P., Lehmann, E., Laloui, L., Vulliet, L., and Flühler, H. (2007). "Water flow between soil aggregates." *Transport in Porous Media*, 68(2), 219-236.

CAWO. "CAWO Intesifying Screens." C. Solutions, ed.

Cnudde, V., Dierick, M., Vlassenbroeck, J., Masschaele, B., Lehmann, E., Jacobs, P., and Van Hoorebeke, L. (2008). "High-speed neutron radiography for monitoring the water absorption by capillarity in porous materials." *Nuclear Instruments and Methods in Physics Research Section B: Beam Interactions with Materials and Atoms*, 266(1), 155-163.

Coles, M. E., Hazlett, R. D., Spanne, P., Soll, W. E., Muegge, E. L., and Jones, K. W. (1998). "Pore level imaging of fluid transport using synchrotron X-ray microtomography." *Journal of Petroleum Science and Engineering*, 19(1-2), 55-63.

David, C., Menéndez, B., and Mengus, J.-M. (2008). "Influence of mechanical damage on fluid flow patterns investigated using CT scanning imaging and acoustic emissions techniques." *Geophysical Research Letters*, 35(16), n/a-n/a.

DiCarlo, D. A. (2010). "Can Continuum Extensions to Multiphase Flow Models Describe Preferential Flow?" *Vadose Zone Journal*, 9(2), 268-277.

DiCarlo, D. A., Seale, L. D., Ham, K., and Willson, C. S. (2010). "Tomographic measurements of pore filling at infiltration fronts." *Advances in Water Resources*, 33(4), 485-492.

Ferréol, B., and Rothman, D. H. (1995). "Lattice-Boltzmann simulations of flow through Fontainebleau sandstone." *Transport in Porous Media*, 20(1), 3-20.

Grunzweig, C., Frei, G., Lehmann, E., Kuhne, G., and David, C. (2007). "Highly absorbing gadolinium test device to characterize the performance of neutron imaging detector systems." *Review of Scientific Instruments*, 78(5), 053708-053708-4.

Hall, S. A., Hughes, D., and Rowe, S. (2010). "Local characterisation of fluid flow in sandstone with localised deformation features through fast neutron imaging." *EPJ Web of Conferences*, 6, 22008.

Hassanein, R., Meyer, H. O., Carminati, A., Estermann, M., Lehmann, E., and Vontobel, P. (2006). "Investigation of Water Imbibition in Porous Stone by Thermal Neutron Radiography." *Journal of Physics D: Applied Physics*, 39(19), 4284-4291.

Heijs, A. W. J., Ritsema, C. J., and Dekker, L. W. (1996). "Three-dimensional visualization of preferential flow patterns in two soils." *Geoderma*, 70(2–4), 101-116.

Hilpert, M., and Miller, C. T. (2001). "Pore-morphology-based simulation of drainage in totally wetting porous media." *Advances in Water Resources*, 24(3-4), 243-255.

Kasteel, R., Vogel, H. J., and Roth, K. (2000). "From local hydraulic properties to effective transport in soil." *European Journal of Soil Science*, 51(1), 81-91.

Kim, F. H., Penumadu, D., Gregor, J., Kardjilov, N., and Manke, I. (2013). "High resolution neutron and X-ray imaging of granular materials." *Journal of Geotechnical and Geoenvironmental Engineering*, 139(5), 715-723.

Lade, P. V., Liggio, C. D., and Yamamuro, J. A. (1998). "Effects of non-plastic fines on maximum and minimum void ratios of fine sand." *ASTM Geotechnical Testing Journal*, 21(4), 336-347.

Perret, J., Prasher, S. O., Kantzas, A., and Langford, C. (1999). "Three-Dimensional Quantification of Macropore Networks in Undisturbed Soil Cores." *Soil Sci. Soc. Am. J.*, 63(6), 1530-1543.

Silin, D., Tomutsa, L., Benson, S., and Patzek, T. (2011). "Microtomography and Pore-Scale Modeling of Two-Phase Fluid Distribution." *Transport in Porous Media*, 86(2), 495-515.

Williams, S. H., Hilger, A., Kardjilov, N., Manke, I., Strobl, M., Douissard, P. A., Martin, T., Riesemeier, H., and Banhart, J. (2012). "Detection system for microimaging with neutrons." *Journal of Instrumentation*, 7(02), P02014.

CHAPTER 8. CONCLUSION AND FUTURE WORK

8.1 Conclusions

Radiation based imaging techniques were used to study partially saturated sand and flow through porous media. X-ray imaging technique can achieve spatial resolution of a few microns routinely with laboratory micro-focus imaging system and even sub-micron spatial resolution at Synchrotron imaging facilities. X-ray imaging technique has been used to study soil for its high contrast to solid particles, but the technique has some limitations with obtaining good contrast with fluid phase. Neutron imaging is a relatively new imaging technique for studying soil, and significant progress has been made in recently in terms of spatial and temporal resolution. Neutron provides good contrast of fluid phase without addition of any contrast agent.

Basics of neutron imaging was studied carefully and applied to study partially saturated compacted sand specimens with different water contents and sand grain shapes. Local water content distribution was visualized quantitatively from radiography and tomography data at coarse spatial resolution.

Much higher spatial resolution neutron tomography imaging was performed on partially saturated compacted sand specimens. The same partially saturated sand specimens were also imaged with micro-focus X-ray tomography system at similar resolution. Dual-modal (neutron and X-ray) contrast of the three phases of partially saturated sand specimen was demonstrated at grain/pore

scale. Feature such as bulking structure was observed at the bottom of compaction layers due to improved spatial resolution and contrast.

The different resolution and sampling of neutron and X-ray imaging data were registered in the same coordinates for complete analysis by using maximization of normalized mutual information. The water phase was segmented from neutron tomography data and the sand phase was segmented from X-ray tomography data. Due to image registration more accurate segmentation was performed at the sand grain and water boundaries.

Direct numerical simulation was also performed based on X-ray tomography image data. Realistic pore geometry was obtained from X-ray tomography data. Based on full morphology approach, drainage condition was simulated and capillary pressure – saturation curve was obtained. Sensitivity of image threshold to the capillary pressure – saturation curve was studied. Hydraulic conductivity additionally was simulated based on simplified Stokes equation and Darcy's law. Different sizes of REV were used to perform the simulation and converging dimension of REV was investigated.

Finally, several in-situ neutron imaging experiments of flow through sand specimens were performed at various neutron imaging facilities with different energy and spatial resolution. Water flow patterns of dense and loose states of Ottawa sand specimens were visualized with time-lapsed radiography and tomography. Compaction process used to prepare the dense state resulted in

compaction layers, and it was observed that water flow was affected by anisotropy due to compaction layers for dense state of sand. Water flowed more freely in the loose state of sand specimen. Ottawa sand and Q-ROK sand water flow was visualized with neutron imaging at one of the highest spatial resolution currently achievable. The initial dry states of the specimens were imaged with micro-focus X-ray system at a similar spatial resolution. The result revealed and confirmed the idea of importance of pore size on capillary flow. Full morphology method which is based on pore size distribution and pore connectivity was used to simulate water flow pattern and the result showed good agreement with the experimental imaging results.

8.2 Future Work

The whole research experience and results obtained during my PhD study provided me valuable knowledge on the radiation based imaging techniques to study various materials including but not limited to soil. The author is planning to continue similar type of research during post-doctoral study.

The author has presented some iterative reconstruction results, but a lot more work is needed to improve the efficiency for larger data sets for high resolution imaging. Possible improvement with the contrast of different phases has potential to improve the accuracy of thresholding and segmentation.

Development of a more advanced image processing/thresholding algorithm is also needed. Development of image processing algorithm is often problem and material specific, and it requires extensive effort.

One of the topics that I would like to continue to study is direct numerical simulation of two fluid phase flow. Lattice – Boltzmann technique is often used to simulate two phase flow. The author is collaborating with Dr. Volker Schulz of Baden-Wuerttemberg Cooperative State University on this topic to directly simulate and compare with experimental results. For the Lattice – Boltzmann simulation, the high performance computing system will be also explored due to the amount of computation required.

VITA

Felix Kim was born in Knoxville, TN in 1982 while his father was working on getting his Ph.D. at the University of Tennessee. After his father obtained the degree, his family moved to Busan, South Korea when Felix was 7. Felix adapted to Korean culture and went through Korean education system from elementary school all the way to high school. Upon graduation from high school, Felix was accepted to Korea University and studied for a semester before he came to University of Tennessee to study civil engineering. He received a Bachelor of Science degree in Civil Engineering in 2006 at University of Tennessee, and obtained Master of Science degree in Civil Engineering (structural engineering emphasis) from Georgia Institute of Technology in 2007. Felix started to pursue a Ph.D degree in Civil Engineering at University of Tennessee under the supervision of Dr. Penumadu. He obtained his doctoral degree in May 2013. Upon completion of Ph.D he intends to continue with post-doctoral research at University of Tennessee directed by Dr. Penumadu.